Defect Structures in Ordered Intermetallics; Grain Boundaries and Surfaces in FeAl, NiAl, CoAl and TiAl

by

Batsirai M. Mutasa

Dissertation submitted to the faculty of the

Virginia Polytechnic Institute and State University

in partial fulfillment of the requirements for the degree of

DOCTOR OF PHILOSOPHY

in

Materials Engineering Science

©Batsirai M. Mutasa and VPI & SU 1997

APPROVED:

Dr. Diana Farkas, Chairperson

Dr. Alex O. Aning

Dr. Stephen L. Kampe

Dr. Ronald D. Kriz

Dr. Yuri M. Mishin

Dr. William T. Reynolds

May, 1997

Blacksburg, Virginia

KEYWORDS: Grain boundaries, Surfaces, Point defects, Intermetallics, Ductility, Atomistic Simulations, FeAl, NiAl, CoAl, TiAl

Defect Structures in Ordered Intermetallics; Grain Boundaries and Surfaces in FeAl, NiAl, CoAl and TiAl

by

Batsirai M. Mutasa

Committee Chairperson: Dr. Diana Farkas

Materials Engineering Science

(ABSTRACT)

Ordered intermetallics based on transition metal aluminides have been proposed as structural materials for advanced aerospace applications. The development of these materials, which have the advantages of low density and high operating temperatures, have been focused on the aluminides of titanium, nickel and iron. Though these materials exhibit attractive properties at elevated temperatures, their utilization is limited due to their propensity for low temperature fracture and susceptibility to decreased ductility due to environmental effects. A major embrittlement mechanism at ambient temperatures in these aluminides has been by the loss of cohesive strength at the interfaces (intergranular failure). This study focuses on this mechanism of failure, by undertaking a systematic study of the energies and structures of specific grain boundaries in some of these compounds.

The relaxed atomistic grain boundary structures in B2 aluminides, FeAl, NiAl and CoAl and $L1_0$ γ-TiAl were investigated using molecular statics and embedded atom potentials in order to explore general trends for a series of B2 compounds as well as TiAl. The potentials used correctly predict the proper mechanism of compositional disorder of these compounds. Using these potentials, point defects, free surface energies and various grain boundary structures of similar energies in three B2 compounds, FeAl, NiAl and CoAl were studied. These B2 alloys exhibited increasing anti-phase boundary energies respectively. The misorientations chosen for detailed study correspond to the $\Sigma5(310)$ and $\Sigma5(210)$ boundaries. These boundaries were investigated with consideration given to possible variations in the local chemical composition. The effects of both boundary stoichiometry and bulk stoichiometry on grain boundary energetics were also considered. Defect energies were calculated for boundaries contained in both stoichiometric and off-stoichiometric bulk. The surface

energies for these aluminides were also calculated so that trends concerning the cohesive energy of the boundaries could be studied. The implications of stoichiometry, the multiplicity of the boundary structures and possible transformations between them for grain boundary brittleness are also discussed.

ACKNOWLEDGEMENTS

I would like to thank Dr. Diana Farkas for not only serving as my committee chairperson and advisor, but for 'volunteering' me to serve as the unix system adminstator. It has been a long and often frustrating journey - thank you for the support and guidance . I would also like to thank Drs. Aning, Kampe, Kriz, Mishin and Reynolds for serving on my committee. My sincere thanks also go to Dr Garth Wilkes.

To Yuri - Dr. Yuri Mishin, a special thanks for the patience to endure what must often have seemed inane and simple questions. Thank you for invaluable discussions and support.

To my office mates - Anne Vilette, Chris Jones, Christophe Vailhe, Julia Panova, Kevin Ternes thank you for making the journey fun with often off-the-wall discussions.

To the friends who supported and encouraged me; Mike,Thobeka, Dilip, Pamela, Kermit, Virginie and Vendetta and to the staff that was always willing to lend an ear and get things done 'yesterday'; Amy, Jan, Trish and Sandy. Thank you all. I would also like to thank the Women's Division of the United Methodist church for financial support.

This dissertation is dedicated to my family.

Mbuya na Sekuru Kachala ndimimakatanga rwendo rwino - "Gweture" wenyu apedza. Mha na Baba basa renyu rapera. Zeki na Chikanhwa - Thanks for the inspiration. Tondi raajana rako. Ndinotenda mese neminamato dzenyu. Tapedza! Angie thanks for a home away from home.

This work was sponsored by the Office of Naval Research and the National Science Foundation.

TABLE OF CONTENTS

LIST OF FIGURES

LIST OF TABLES

0.1 INTRODUCTION

0.1.1 Potential Applications

The increased demands on aircraft and aerospace system performance has led to the need for the development of new and improved structural materials. The future aircrafts will primarily require: higher thrust-to-weight ratio, increased fuel efficiency, reduced cost, and longer service lives. For these reasons the materials required will have to be stronger, lighter, stiffer and have the ability to maintain these properties at elevated temperatures and in hostile environments. These materials would be utilized in the structural framework and in the aircrafts' engines. The most important requirement for structural aircraft framework is the weight reduction, since 25% of unfueled weight of a typical naval aircraft is made up of the airframe. These requirements translate into the development of low density, high oxidation resistance, high strength intermetallic compounds with increased reliability at higher stress levels which will enable the design and production of higher performance, lighter (high thrust-to-weight ratio) engines for future military aircraft and supersonic commercial transport such as the National Aerospace Plane (NASP), the High Speed Civil Transport (HSCT) and the Intergrated High-Perfomance Turbine Engine Technology Initiative(IHPTET). An example of the possible gas turbine applications proposed for titanium aluminides are shown in Figure 0.1 [1]

The automotive industry has recently been faced with technological challenges which result in the need for improved fuel efficiency, enhanced performance, reduced emissions, greater safety, as well as better styling options and improved quality. These features can be attained, in part, by reducing the weight of the engine and transmission parts, especially the reciprocating or moving parts.

0.1.2 Intermetallic Aluminides

Several B2 intermetallic compounds are currently being investigated for potential high temperature structural applications. CoAl, NiAl, and FeAl are three binary B2 aluminides of the transition metals from the same row of the periodic table. These aluminides have the same B2 (CsCl) ordered crystal structure, but exhibit decreasing ordering energy and increasing ductility from CoAl

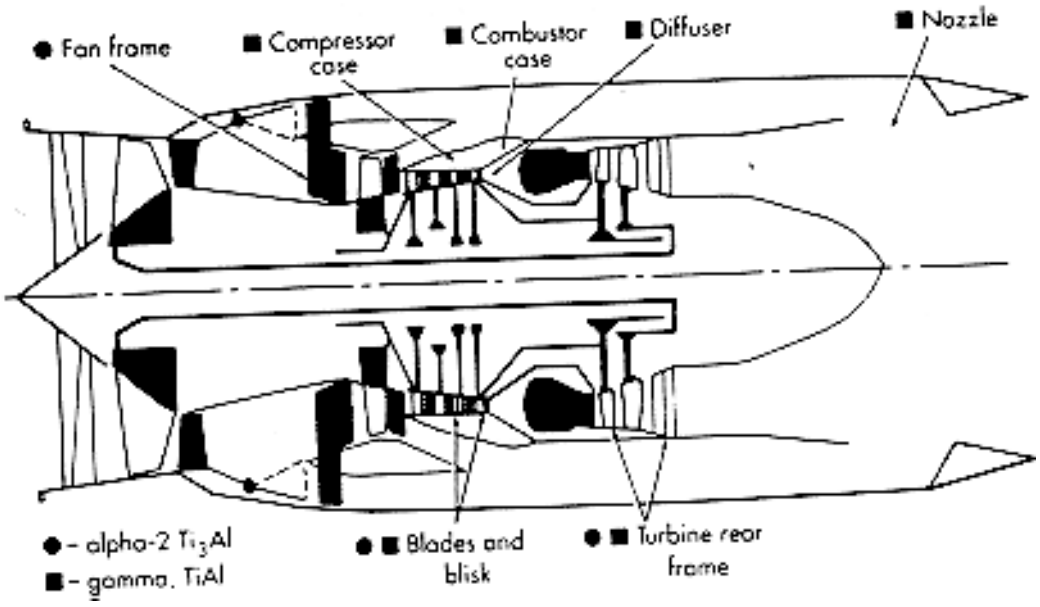

Figure 0.1: Potential applications for titanium aluminides [1]

to FeAl. They have lower densities and higher melting temperatures than Ni-based superalloys and $L1_2$ Ni_3Al [9]. More details are given in Chapter 1.2.

TiAl -based materials are also under investigation for use at elevated temperatures. γ-TiAl with the $L1_0$ crystal structure, is a strong candidate due to the need to develop lightweight materials. It posseses a low density which is less than half that exhibited by superalloys. In addition to this, its high aluminum content makes it highly resistant to oxidation and burning; ideal properties for the high temperature applications it has been targeted for. More details are given in Chapter 1.3.

However, the practical applications of these ordered intermetallic alloys are hindered by their intergranular brittle failure and poor cleavage fracture resistance at ambient temperatures as well as their low strength and creep resistance at elevated temperatures. The brittleness along grain boundaries appears to be intrinsic and thus the phenomenon of grain boundary brittleness, probably related to the cohesive strength of the boundaries, is the main impetus for this study. When dealing with intergranular fracture it is important to gain insight into the structure-property correlations. From a materials design standpoint, it is through the intergranular fracture that one can control the fracture properties. The understanding of the chemistry and structure of these boundaries will

aid in the comprehension of the cause and mechanism of this phenomenon. Ordered intermetallic compounds have been shown to exhibit a multiplicity of boundary structures that differ in both atomic arrangment and local chemical composition. The energy calculation for a stoichiometric boundary embedded in a stoichiometric alloy is unique and does not require knowledge of the chemical potentials of the components. The energy of an off-stoichiometric boundary, however, is dependent on the difference in the chemical potentials. In the present work, we calculated grain boundary structures and energies by means of atomistic computer simulations.

CoAl, NiAl and FeAl, like other B2 compounds, accommodate the departure from stoichiometry via the triple-defect mechanism. This mechanism is characterized by the formation of constitutional vacancies on M, the transition metal, sites in Al-rich compounds and the creation of Co, Ni or Fe constitutional antisites on Al sites in Al-deficient compounds. γ-TiAl, on the other hand, accomodates this departure from stoichiometry by forming constituitional antisites on both sides of stoichiometry.

In the study of extended defects, such as grain boundaries, that show off-stoichiometry locally at the core of the defect, the knowledge of the chemical potentials of the components in the compound is needed. The proper calculation of the chemical potentials according to the correct thermodynamic definition requires the formation energy of the constitutional point defects that accommodate the deviation from stoichiometry. The point defect simulations and the calculated predictions of the point defects which accomodate off-stoichiometry are given in Chapter 3. In this chapter, the chemical potentials are also given, as is the method of calculating energies for defects that are non-stoichiometric.

In the present work, the surfaces and grain boundaries have been studied using EAM type potentials that were fit specifically for the B2 and γ phases in the B2 and TiAl systems respectively and correctly predict the point defects in off-stoichiometric systems. The misorientations chosen for detailed study for the B2 compounds correspond to the $\Sigma = 5(310)[001]$ and $\Sigma = 5(210)[001]$ symmetrical tilt boundaries. These boundaries correspond to planes that have different chemical compositions per layer. For the B2 compounds the (310) planes consist of 50% Al and 50% transition metal atoms. The (210) planes, on the other hand consists of alternating 100% Al and 100%

transition metal atoms of layers. This work is shown in Chapter 5. The work on grain boundaries in γ TiAl is shown in Chapter 6. This chapter looks at the $\Sigma = 5(210)[001]$ symmetrical tilt boundaries, as well as the twins and pseudo-twins.

To determine the grain boundary cohesive energies in the compounds under consideration, a detailed study of the (310) and (210) surface energies with various Ti, Ni, Fe, Co, or Al-rich terminations was carried out. A multiplicity of possible structures was studied for each boundary. Chapter 4 shows this work on surfaces, including the work on high index surfaces for bcc and fcc based materials.

Chapter 2 discusses the Embedded Atom Method (EAM) which is the simulation technique used in this work. A brief overview is also given of the interatomic potentials used. The atomistic simulations are compared to experimental, high resolution electron microscopy images in Chapter 7

Chapter 1

LITERATURE SURVEY

1.1 Intermetallic Compounds

Intermetallic compounds are a class of advanced materials which can be defined as an ordered alloy phase formed between two or more metallic elements. An alloy phase is ordered if two or more sublattices are required to describe the atomic structure. This ordered structure is advantageous in that it possesses long-range order with the attendent difficulty in dislocation motion. These factors result in good elevated temperature properties, such as strength and stiffness, but this long-range order also results in poor ambient temperature properties, such as ductility and fracture toughness, due to the low dislocation mobility.

Prime candidates for elevated temperature usage are transition metal-aluminides, such as iron, nickel, and titanium aluminides, which maintain good mechanical properties at these temperatures. The nickel aluminides have been shown to have higher melting points and oxidation resistance as well as lower strength in comparison to the titanium aluminides, but they exhibit more brittle behaviour at lower temperatures. The iron aluminides have been shown to be heavier than the titanium aluminides, but they are more ductile at lower temperatures.

Ordered intermetallics based on the aluminides have shown promise as a class of metallic materials for high temperature and hostile environment use. The physical and mechanical properties and oxidation behavior of the first row of transition metals B2 aluminides [9] and γ-TiAl [6] [10] have been reviewed and shown to exhibit a wide range of behaviors. Many of their properties are dominated by the presence of constitutional defects, ie constitutional vacancies and antisite defects. The diffusion behavior in these compounds is reasonably clear, but the effects of extrinsic parameters, such as the environment, the anomalies in intrinsic parameters such as the slip sys-

Table 1.1: Comparison of physical properties of Aluminides [2] [6] [7] [8]

Compound	Crystal Structure	Melting Temperature(^{o}C)	Density(g/cc)	Fracture mode	Ductility (%) RT
Fe3Al	DO_3	1540	6.7	C	4-8
FeAl	B2	1330	5.6	IG +/ C	2.5 -8
Ni3Al	$L1_2$	1390	7.5	IG	
NiAl	B2	1640	5.92	IG	0-2
CoAl	B2	1638	6.08		
Ti_3Al	$D0_19$	1180	4.1 - 4.7		2-5
γ-TiAl	$L1_0$	1440	3.7 - 3.9		1-3
Superalloys	fcc/$L1_2$	1450	8.3		3-5

tems, differing grain size effects and differing effects of temperature on yield strength have yet to be understood. More work is thus required to give systematic results, ensure reproducibility and ease of processing before these compounds can be applied on a major scale.

These aluminides show six major advantages for high temperature structural applications over the Ni based superalloys in use today. They have lower densities and higher melting temperatures than their counterparts as shown in the Table 1.1 [2] [6] [7] [8]. The lower densities result in lower operating stresses that make it possible to fabricate smaller and lighter components which, in turn, result in better engine accelerations due to the lower inertial mass of the rotating parts. The melting temperatures define the upper limit of use temperature and are indicators of the temperature range at which diffusion controlled processes start to dominate. For example the melting temperature of NiAl is more than 200^{o}C higher than conventional Ni based super alloys. In addition they have better oxidation resistance and lower ductile to brittle transition temperature (DBTT), as compared to that of the super alloys. Although these compounds have higher thermal conductivities, with NiAl having 4 to 8 times that of the superalloys, depending on temperature and composition, they have similar thermal expansion characteristics. Figure 1.1 shows this comparison of the thermal conductivities for single crystalline NiAl and a superalloy [2]. In comparison to the superalloys, these aluminides, not only have the advantage of density, oxidation resistance, thermal conductivity, DBTT and melting temperature, but the components are relatively inexpensive since they do not generally incorporate rare and strategic elements.

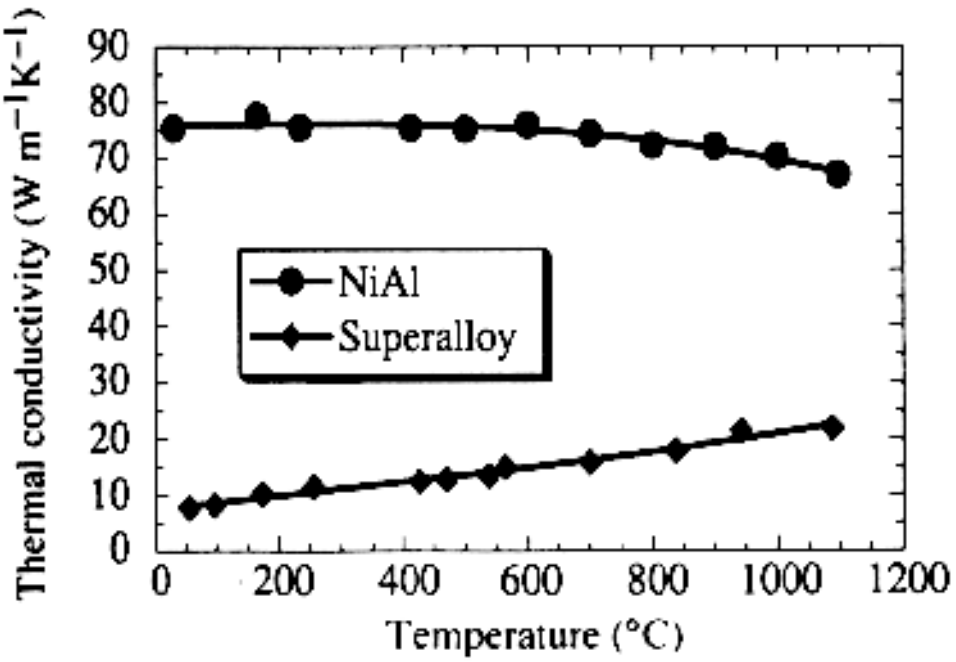

Figure 1.1: Comparison of the thermal conductivity, as a function of temperature, of single crystal NiAl with a Ni-based superalloy [2]

The effecting of the many applications is, however, limited by the low temperature brittleness of these compounds and the attendant difficulty in processing. Significant improvements to mechanical properties and ductility have been attained by microalloying and different processing techniques, in an effort to balance ductility, toughness, strength, impact resistance and fatigue characteristics.

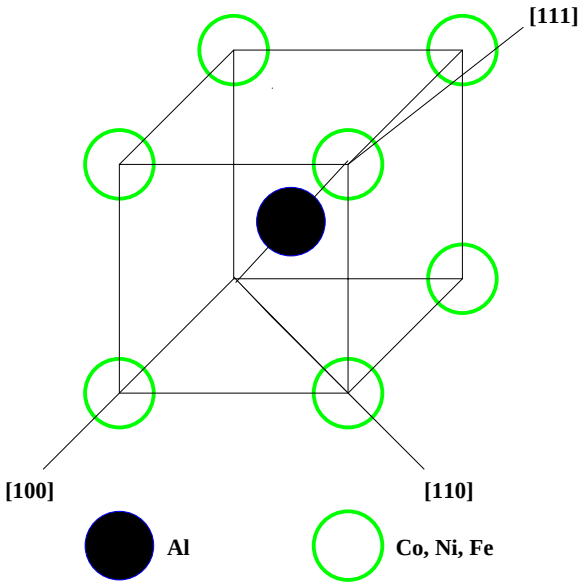

Figure 1.2: The B2 Crystal Structure

1.2 B2 Aluminides

1.2.1 General Characteristics

The aluminides of interest for this paper are NiAl, CoAl and FeAl which are the three binary B2 aluminides that are constructed from the first row of transition metal elements in the periodic table. The B2 (CsCl or $L2_0$) crystal structure of the binary intermetallic compounds under discussion is shown in Figure 1.2. This structure is a body centered ordered structure, where the Al occupies the body center and the transition metal, the corner site. It is the simplest and most common ordered structure with a simple cubic Bravais lattice. The B2 structure has two atoms per unit cell and can thus be described as two interpenetrating simple cubic sublattices. The preferred bonding between Al and the transition metal atoms causes each type of atom to locate at specific sites in the b.c.c. crystal lattice. These alloys have differing ordering energies and they have a higher ductile-to-brittle transition temperature (DBTT) than b.c.c. metals. A brittle fracture occurs in a large number of B2 aluminides at room temperature.

The phase diagrams [11] for the B2 compounds under study are shown in Figures 1.3, 1.4 and

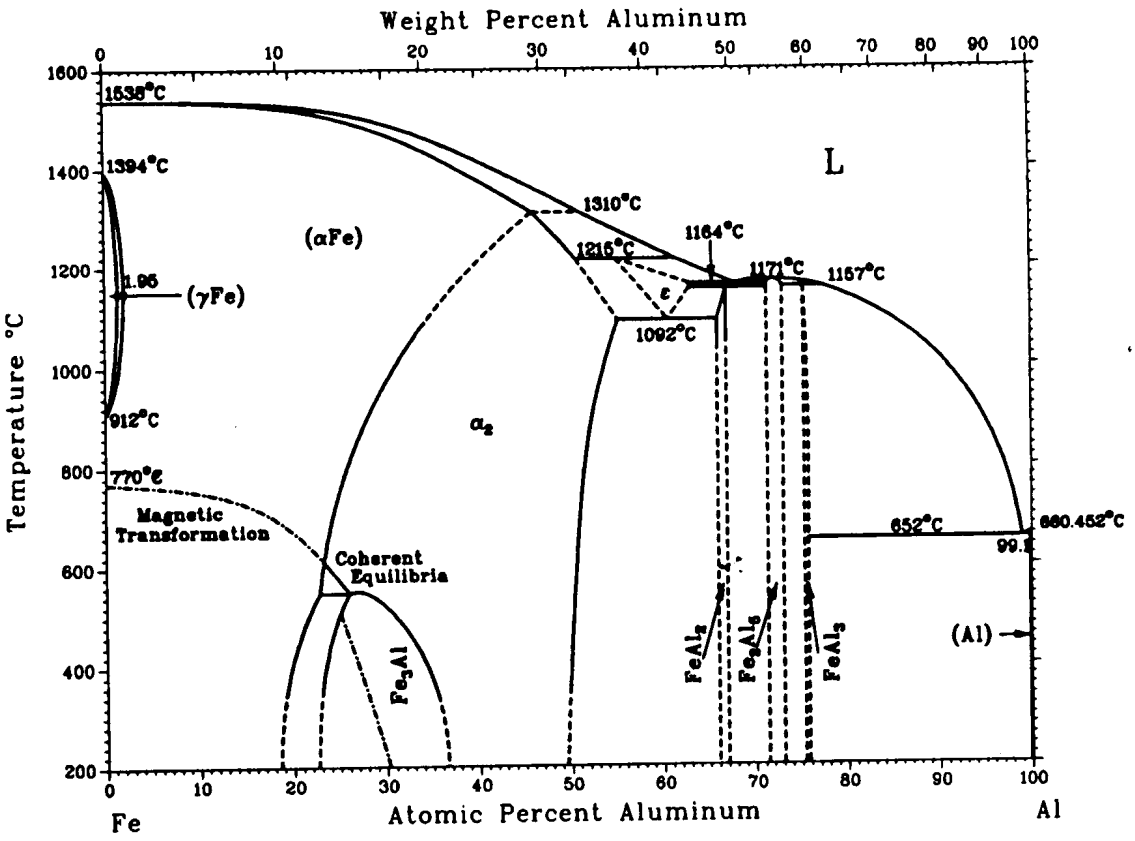

Figure 1.3: FeAl Phase Diagram

1.5. From the wide single phase fields in the phase diagrams it can be seen that these aluminides can form over a wide range of compositions. The range for FeAl extends from about 35 to 52 at.% Al, whereas that of NiAl, ranges from 45 9 to 60 at.% Al. The NiAl melts congruently at 1638^{o}C and CoAl at 1648^{o}C, whereas FeAl has a melting temperature that decreases with Al content to 1250^{o}C at 52 at% Al.

1.2.2 Diffusion

A knowledge of diffusion behavior of B2 compounds is required for production and application of these materials. In ordered alloys, unlike pure metals in which self diffusion occurs by random vacancy motion, self diffusion is not possible since it would disrupt the ordering.

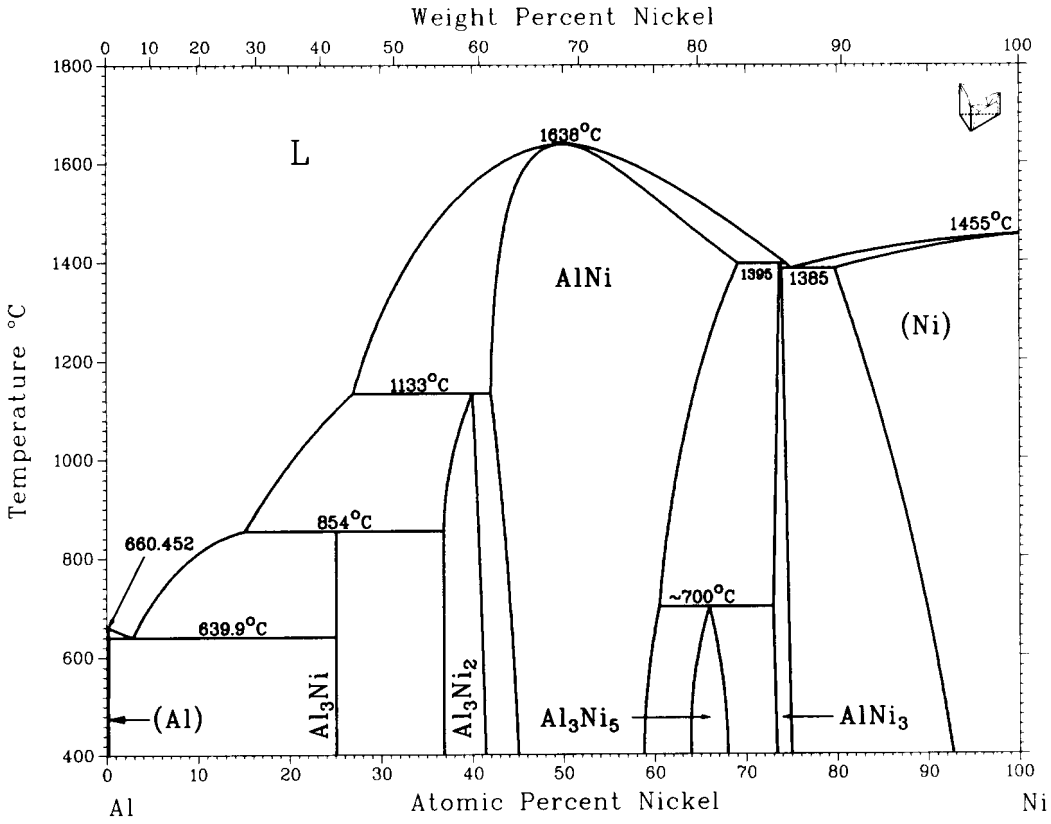

Figure 1.4: NiAl Phase Diagram

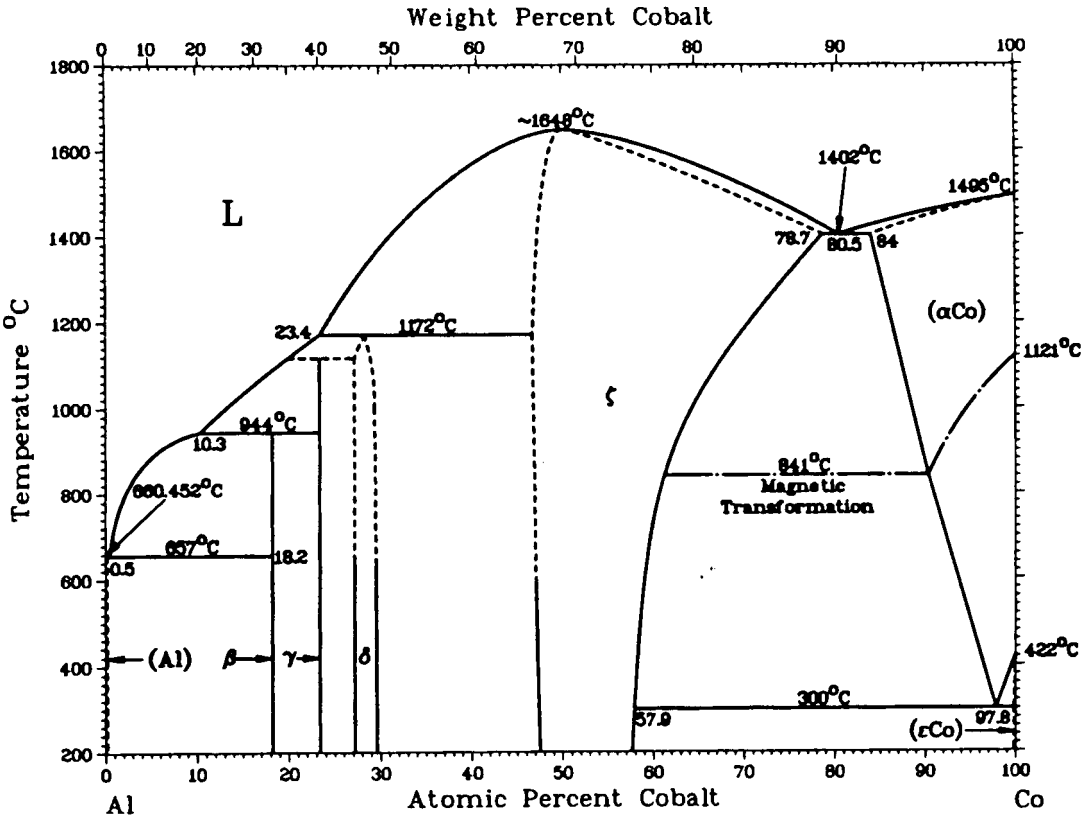

Figure 1.5: CoAl Phase Diagram

It has been shown that deviation from stoichiometry leads to several types of diffusionmechansims, which mirror the variation of constitutional vacancy density with deviation from stoichiometry. The possible mechanisms that have been proposed include single vacancy transport, triple defects mechanism and the six-jump cycle. The six-jump vacancy model allows diffusion to occur exclusively by nearest neighbor vacancy jumps. Which behavior predominates is dependent on temperature, stoichiometry and ordering energy of the compound.

The diffusion coefficient for Ni in NiAl is a minimum at stoichiometry, and it increases more rapidly with deviation from stoichiometry on the Al-rich side, due to the large number of constitutional vacancies on the Ni sites. Q, the activation energy for diffusion of Ni in NiAl peaks at stoichiometry when the least number of antisite atoms or constitutional vacancies are present [12].

1.2.3 Environmental Effects

The proposed applications for these materials require use in hostile environments and so resistance to oxidation, sulfidation, salt and air corrosion at high temperatures is essential for their applicability without compromising their structural integrity. Environmental embrittlement is a major cause for the low ductility in many ordered intermetallics at ambient temeperatures.

It has been found that some B2 compounds exhibit increased strains when tested in hydrogen, vacuum or oxygen, but show decreased elongation (less ductility) in air, where atomic hydrogen leads to embrittlement especially in FeAl [13]. Liu et al. showed that FeAl is intrinsically ductile, and its poor ductility is due to hydrogen induced embrittlement caused by moisture in the air. 36.5at.%Al FeAl was shown to have ductilities of 2.2% in air, 5.4% in vacuum and 17.6% in dry oxygen [3]. A graphical presentation of the effect of different test environments on ductility is shown in Figure 1.6 (From Ref.[3]). There is no environmental sensitivity of FeAl at Al content above 38 at.% because above this composition the alloy is intrinsically brittle. There is an attendant change in fracture mode, from transgranular cleavage in air to mainly grain boundary separation (intergranular fracture) in dry oxygen. The fracture mode changes from interganular at high ductilities to transgranular at low ductilities. The FeAl cleavage planes are more prone to environmental embrittlement than are grain boundaries. Liu et al. explained the environmental embrittlement by

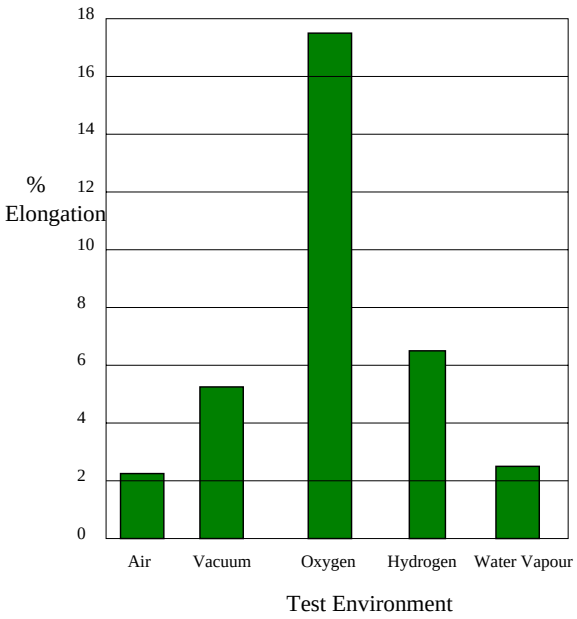

Figure 1.6: Environmental effects on ambient temperature ductility in FeAl [3]

the following chemical reaction:

$$2Al + 3H_2O - -- > Al_2O_3 + 6H^+ + 6e^- \tag{1.1}$$

The reaction of the water vapor in the air with the Al atoms at the crack tips terminates in embrittlement due to the formation of the high fugacity atomic hydrogen which penetrates the crack tips. The molecular hydrogen does not cause severe embrittlement possibly due to its lower activity in comparison to the atomic hydrogen produced from the reaction with the water vapor [3].

Numerous methods to emiliorate ductility have been proposed and implemented that include the formation of protective oxide layers on surfaces by alloying with chromium and/or preoxidizing in air. Grain structure refinement by either thermo-mechanical treatment or second-phase particles (alloying with Zr, B and C to form zirconium borides and carbides), is one method being used.

1.2.4 Strain aging

Recent studies [14] indicate that the fracture resistance of single crystals of NiAl in the $\langle 110 \rangle$ orientation can be improved by controlled heat treatments. These studies propose that NiAl single crystals are intrinsically ductile and that their low ductility and poor toughness at room temperature can be attributed to strain-aging embrittlement, involving pinning of mobile dislocations by interstitial impurities such as carbon and oxygen. Based on this embrittling mechanism, it is expected that the fracture resistance of NiAl crystals can be effectively improved by either reducing the interstitial content or by scavenging interstitials with certain alloying additions.

1.2.5 Fracture

B2 aluminide single crystals have been investigated for cleavage fracture at temperatures below their ductile-brittle transition temperatures [15]. Ordered B2 compounds have two different atoms located at specific sites, and a strong bonding between the unlike atoms makes the crystal more likely to cleave in preferred planes. The B2 aluminides have different room temperature fracture resistance and it was found that FeAl has the highest fracture resistance qualitatively and CoAl the lowest [15]. The fracture resistance was anisotropic due to the existence of a preferred cleavage plane in B2 compounds. A high fracture resistance is measured in the orientation away from the cleavage plane. Griffith's theory in its original form is used when the fracture resistance is intrinsic, ie. a perfectly brittle material fractures with no plastic deformation. The fracture resistance is determined by the crack surface energy or by the free surface energy. An intrinsically brittle single crystal would thus cleave on the plane with the lowest surface energy [16] and CoAl which has high ordering energies generally cleave on $\{110\}$ plane, while FeAl which has a lower ordering energy, cleaves on $\{100\}$ plane like pure b.c.c. metals. The NiAl has a transition fracture region, which has fracture facets on $\{511\}$ transient planes, during the initial cracking stage, followed by final cleavage in the $\{110\}$ plane. An atomistic comparison of the surface energies is shown in Chapter 4.

Hahn and Vedula [17] showed that the predominant fracture mode for polycrystalline NiAl is intergranular at room temperature (RT) and changes to transgranular cleavage around 400-500^{o}C.

Above 600^{o}C it changes to ductile rupture. The fracture toughness of NiAl crystals increases significantly as the temperature is raised to above 200^{o}C. This fracture toughness is independent of the crystal orientation. The crack propagation behavior and crack growth resistance in B2 NiAl and FeAl have been found to differ. Cracks in NiAl show run-arrest behavior, and the fracture toughness of NiAl is insensitive to the average rate of crack propagation, Fe additions and small B additions. By contrast, the crack growth resistance of FeAl decreases as the crack-propagation velocity decreases, and B additions increase the crack growth resistance [18]

1.2.6 Ductility

In the B2 compounds, under study, two slip modes are observed; $\langle 100 \rangle$ slip in NiAl and CoAl and $\langle 111 \rangle$ slip in FeAl. The different slip systems result in differing behavior. B2 compounds, eg., NiAl and CoAl that deform by $\langle 100 \rangle$ slip [19] only have 3 independent slip systems which are insufficient to fulfill Von Mises criterion [20], ie., no plastic flow in the polycrystal is possible. The polycrystals are, therefore, not expected to be ductile. Twinning would be a means by which additional modes of deformation would be possible, but B2 compounds do not twin easily due to the fact that the twinning mode for b.c.c. based compounds; $\langle 111 \rangle \{112\}$ results in disordering in B2 compounds. Compounds, such as FeAl, that display $\langle 111 \rangle$ slip are more likely to be ductile because they meet the Von Mises criterion; the required five independent slip systems are present. FeAl single crystals have been found to be ductile in compression, but as yet not discovered if they are also ductile in tension. As noted earlier the ductility of polycrystalline FeAl is strongly affected by the environment.

Stoichiometric or Ni-rich compositions of single crystalline NiAl are ductile under compression [19] and the strain to failure depends upon the axis of compression. An increase in compressive ductility has also been observed when the single crystal is oxidized prior to testing. [21]

Polycrystalline NiAl has been found to be brittle at room temperature at all compositions and it fractures intergranularly at stoichiometric and transgranularly at other compositions [19]. The RT tensile ductility of polycrystalline NiAl can range from 0-2%, depending on stoichiometry and alloying additions. Other investigators have found limited tensile elongation in stoichiometric

compositions [17], [22]. The reason for this limited elongation is not yet clear; however, it has been found that the yield strength decreases more quickly than fracture stress approaching stoichiometry; thus, the stoichiometric composition is the one most likely to be ductile. Rozner and Wasilewski [22] suggested that stoichiometric NiAl might be inherently ductile, but that its ductility was dependent on surface finish. Polycrystalline NiAl shows tensile ductility at elevated temperatures [19], with no change in slip systems being observed.

An increase in ductility of FeAl has been found with increasing iron content. Channeling patterns taken from intergranular fracture surfaces are sharp, indicating that at compositions near stoichiometry fracture occurs before yielding. Conversely, Fe-rich compositions yield prior to fracture by transgranular cleavage. The lower ductility of Al-rich compositions might be linked to environmental effects. Unlike the B2 aluminides,such as NiAl, which exhibit $\langle 100 \rangle$ slip and are most ductile at stoichiometry, where they exhibit a minimum in yield strength; it has been found that FeAl is brittle at stoichiometry, and does not exhibit a yield strength minimum at this composition.

The ductility of FeAl increases with increasing temperature despite the change from $\langle 111 \rangle$ to $\langle 100 \rangle$ slip modes [23], which results in insufficient slip systems for plastic flow to occur according to Von Mises criterion. This increasing ductility of FeAl might be due to diffusion-controlled processes such as climb contributing additional deformation modes as well as the onset of dislocation climb [23]. FeAl shows a decrease in ductility at temperatures above 0.6Tm (Tm is the melting temperature), and a change from transgranular cleavage to intergranular fracture, possibly due to cavity formation at the grain boundaries by impurity segregation to the interfaces [23].

1.2.7 Alloying Additions

Alloying additions have been found to affect ductility in one of two ways. Alloying additions can decrease ductility by segregating to the grain boundaries, which is due to grain boundary hardening by occupying interstitial sites, especially in powder processed material. Alloying additions also improve ductility by changing fracture modes ie. from intergranular to transgranular fracture as seen by the effect of boron in NiAl [24] [4].

Alloying additions have been made to NiAl in order to promote $\langle 111 \rangle$ slip, by trying to make the bonding more metallic, and thus providing sufficient slip systems for plastic flow [20] as determined by the Von Mises criterion. One of the ternary additions that has received much interest is boron. Figure 1.7 shows a comparison of Auger spectra for grain boundaries of undoped, B-doped and C-doped NiAl [4]. The boron is shown to segregate to the grain boundaries, but carbon does not. If carbon were present it would exhibit a peak at 272 eV. Stoichiometric NiAl at RT exhibits intergranular fracture without boron addition and brittle cleavage with boron addition [4]. Boron addition also produces an increase in yield strength by solid solution hardening. Even though boron segregates to the grain boundary and suppresses intergranular fracture, there is no accompanying improvement in tensile ductility due to lack of slip systems. This lack of improvement is caused by the cleavage fracture mode becoming operative before extensive plastic deformation occurs. The improvement of NiAl ductility, therefore, lies not only in grain boundary strengthening by boron addition, but a method to modify the slip behavior is needed.

Microalloying with Fe, Ga and Mo has been shown to significantly improve the RT tensile ductility of NiAl single crystals tested along a $\langle 110 \rangle$ direction. The failure strain has been shown to increase from the typical 1% exhibited by stoichiometric NiAl to 6% with 0.25% Fe [2]. Figure 1.8 shows the plastic elongation to failure at RT as a function of the ternary alloy concentration for the $\langle 110 \rangle$ oriented specimens. Limited ductility in NiAl with Fe additions has been observed without any change in the slip vector. The mechanism by which this limited ductility occurs is not known [25]. Increasing the amount of Fe added or making the alloy sufficiently Ni-rich may result in a two phase (B2 $+L1_2$) microstructure with improved mechanical properties. An example of a resultant two phase alloy is Ni-30Fe-20Al, which can exhibit 22% tensile elongation at room temperature [26]. Additions of chromium, vanadium, and manganese all resulted in a change in slip vector but without an ensuing improvement in ductility [27], [28]. Adding Nb to NiAl results in a fine dispersion of NiAlNb which strengthens NiAl by impeding dislocation motion [29].

In Fe-rich FeAl, boron addition was found to increase the room temperature ductility, though no concomitant increase in yield strength was observed, as in NiAl. These effects were not observed for the stoichiometric composition. Boron additions to the stoichiometric alloy changed the failure

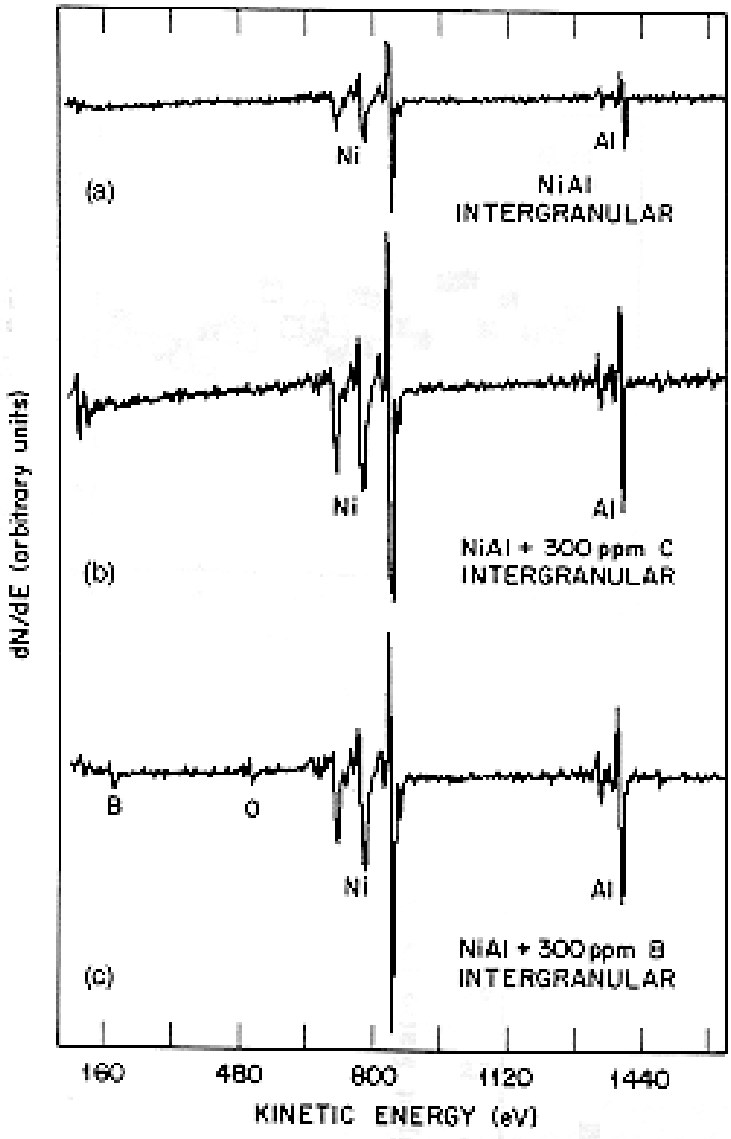

Figure 1.7: Comparison of Auger spectra from grain boundaries in a) undoped b) C-doped and c) B-doped stoichiometric NiAl [4]

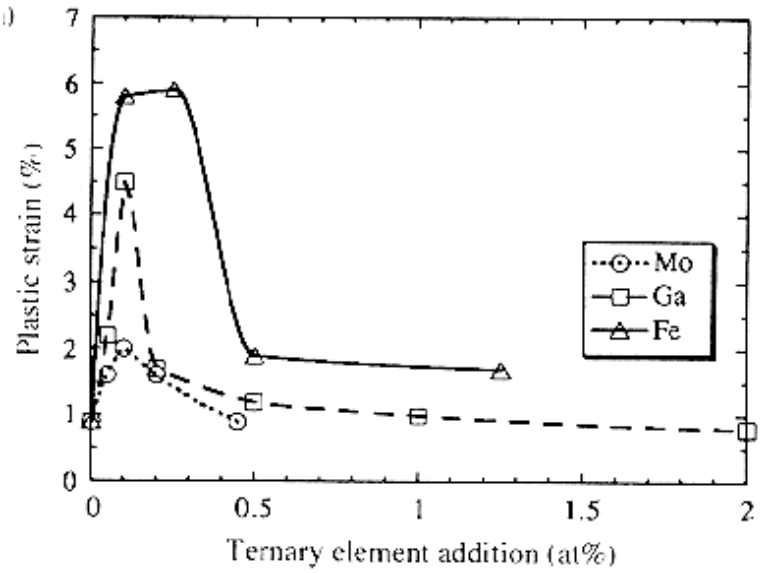

Figure 1.8: Compositional dependence of ductility in NiAl as a function of Fe, Ga and Mo concentration [2]

mode from intergranular fracture to transgranular cleavage.

1.2.8 Oxidation

In the study of the oxidation behavior of B2 compounds, a parabolic growth rate was observed [30]. The stable oxide which forms is α-alumina. This oxide growth occurs by oxygen diffusing inward through the oxide, with oxide formation taking place at the metal/oxide interface. The oxidation rate varies with Al content. In NiAl the maximum oxidation resistance is observed at 4%2Al, whereas in CoAl this occurs at the stoichiometric composition. In Fe-rich FeAl oxidation resistance increases with increasing Al content. Oxidation resistance in NiAl decreases at Al contents lower than 42%, due to the formation of nickel oxides. Oxidation resistance can be improved by the additions of rare earth metals and transition metals.

A decrease in the polycrystalline ductility of NiAl is observed during oxidation due to the presence of small crack-like wedges of oxide at the grain boundaries. This phenomenon is not observed in single crystals where an increase in ductility and decrease in yield strength occurs during

oxidation due to the nucleation of mobile non-screw dislocations at the oxide/metal interface.

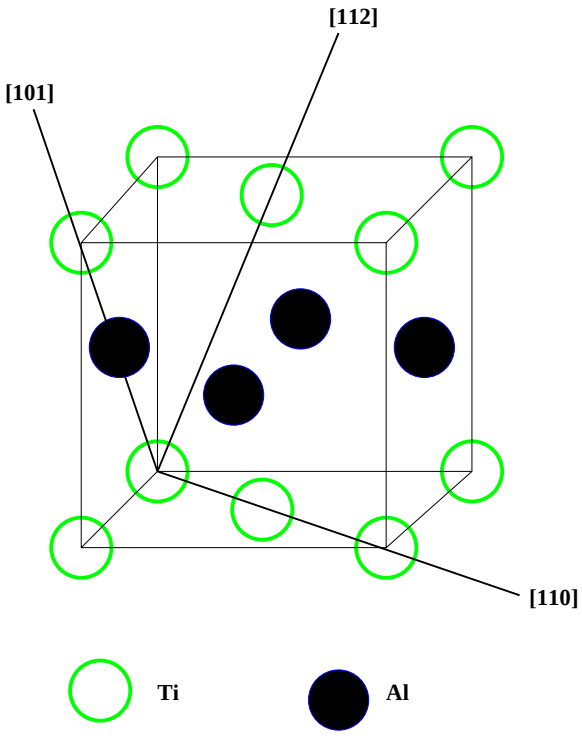

Figure 1.9: The $L1_0$ Crystal Structure

1.3 TiAl

1.3.1 General Characteristics

The γ alloys can be divided into the single phase (γ) and the two phase ($\gamma + \alpha$) alloys. In this discourse, particular attention shall be given to the single phase alloy. γ-TiAl is an ordered, equiatomic compound which has received much attention due to its high specific strength, high modulus and oxidation resistance. The $L1_0$ crystal structure of this binary intermetallic is shown in Figure 1.9. This structure is a face-centered tetragonal (fct) structure with alternating (002) planes of Ti and Al atoms and a small tetragonality ($c/a = 1.02$) at the equiatomic composition. This tetragonality increases to 1.03 at higher Al concentrations. The tetragonality of the structure is decreased to a near fcc structure with decreasing Al content.

The binary Ti-Al phase diagram [1] is shown in Figure 1.10. The single-phase γ is stable on

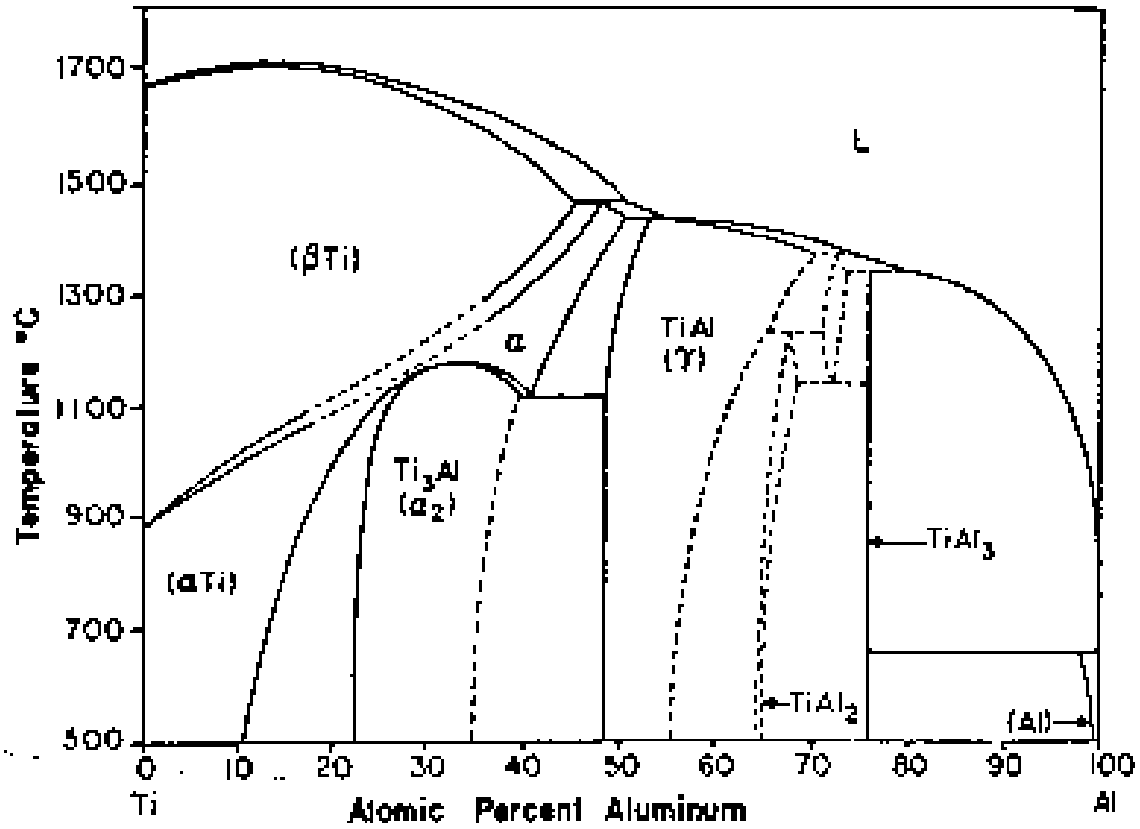

Figure 1.10: The TiAl Phase Diagram

the aluminum rich side from 49 to 66% Al and is considered to be ordered up to the melting point of 1440^{o}C. The two phase microstructure ($\gamma + \alpha$) has nearly stoichiometric or titanium rich compositions. The two phase compounds have been found to be slightly more ductile than the single phase compounds. This ductility is however, still limited to 2-3%.

Titanium aluminides are contemplated for use in structures operating in the range of 600 to 1000^{o}C. γ-TiAl has a higher modulus, lower density good thermo-conductivity and better high temperature capabilities as compared to other titanium alloys as well as the nickel based superalloys. One of its major advantages is stiffness; γ-TiAl has a specific stiffness that is 50% greater than commonly used alloys. It however exhibits poor fracture resistance and low ductility at room

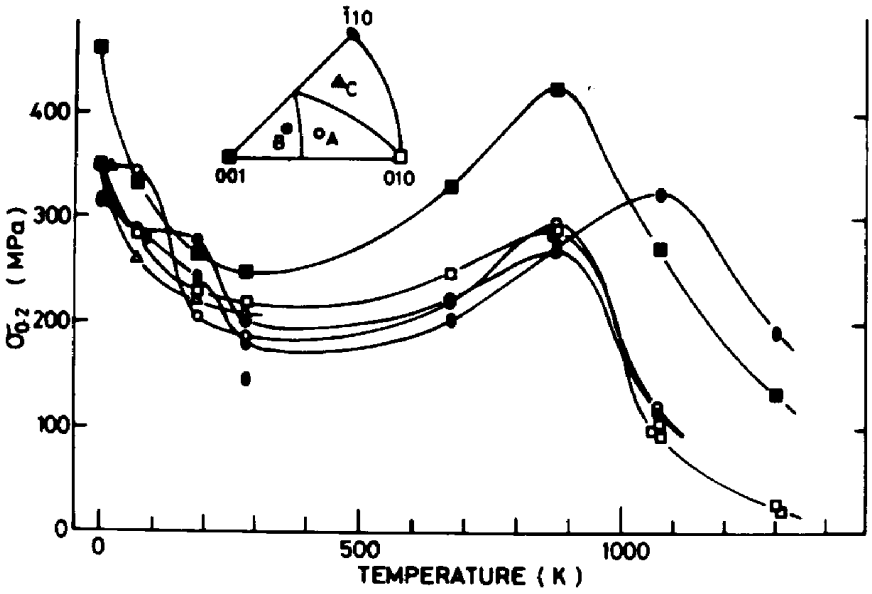

Figure 1.11: The temperature dependence of 0.2% proof stress for various orientations [5]

temperatures. Its low impact resistance would make it prone to machining accidents. The low temperature ductility has been attributed to the long range ordering which gives it its strength.

1.3.2 Anomalous Yield Stress

A yield stress anomaly was reported for single crystals of aluminum rich, γ-TiAl [5]. Aluminum rich single crystals of TiAl were studied in compression, in a temperature range between 4.2K and 1273K, as a function of both temperature and orientation. For all the orientations studied, the yield stress was shown to decrease with temperature up to $\approx$ 273K, where the yield stress then proceeded to increase with temperature to peak at $\approx$ 873K, after which it rapidly decreased with continued temperature rise. This behavior is termed the 'positive temperature dependence of yield stress' and is shown in Figure 1.11 [5]. The exact minima and maxima differed slightly for the orientations studied.

1.3.3 Oxidation Resistance

The oxidation resistance of TiAl compounds deteriorates at temperatures greater than 800^{o}C, especially if the compounds are either under cyclic or thermal loading. The oxidation resistance of γ-based alloys has been found to increase with increasing Al content. This effect, however, is not significant in the most ductile range of 45-50at.% Al.

Alloying additions of various elements have been studied as a means of improving oxidation resistance. The most impressive ternary element additions were exhibited with Nb, Mo and W, where additions as low as 1-2%, allow for the use of γ alloys at 800^{o}C without any coating. This is achieved by forming a layer of Al_2O_3, as opposed to the mixed layer formation of Al_2O_3 and TiO_2 that is present on exposure to air, without the additions [6]. How the alloy additions achieve this is uncertain, but it is known that a continuous layer of Al_2O_3 generally slows the influx of oxygen and the rate of internal oxidation. The formation of Al_2O_3 is favored below 750^{o}C, whilst TiO_2 formation dominates at temperatures above 800^{o}C. Extended exposure to air at temperatures of 600-850^{o}C results in decreased tensile ductility. Other effects of the alloying additions are to suppress the growth of TiO_2, as with tungsten.

Protective surface coatings have also been investigated as a method of improving oxidation resistance in these alloys. One such approach is the heating of TiAl under a low partial pressure of oxygen to produce a thin layer of Al_2O_3. This process however, lacks longevity due to the thinness of the layer formed. Another method is to coat with Al_3Ti. This coating method retains its integrity up to 950^{o}C but has the problem of micro-crack formation.

1.3.4 Alloying Additions

Single-phase γ tends to fracture before reaching 1% strain in tension. This brittle behavior can be improved by alloying additions [31]. Alloying additions of V, Mn and Cr have been found to positively affect ductility in γ alloys. This effect however is a function of both microstructure and Al content and these effects are observed for only the two phase structures in the region of 45-50% Al. The effect of these ternary additions is shown in Figure 1.12. The alloying additions are limited

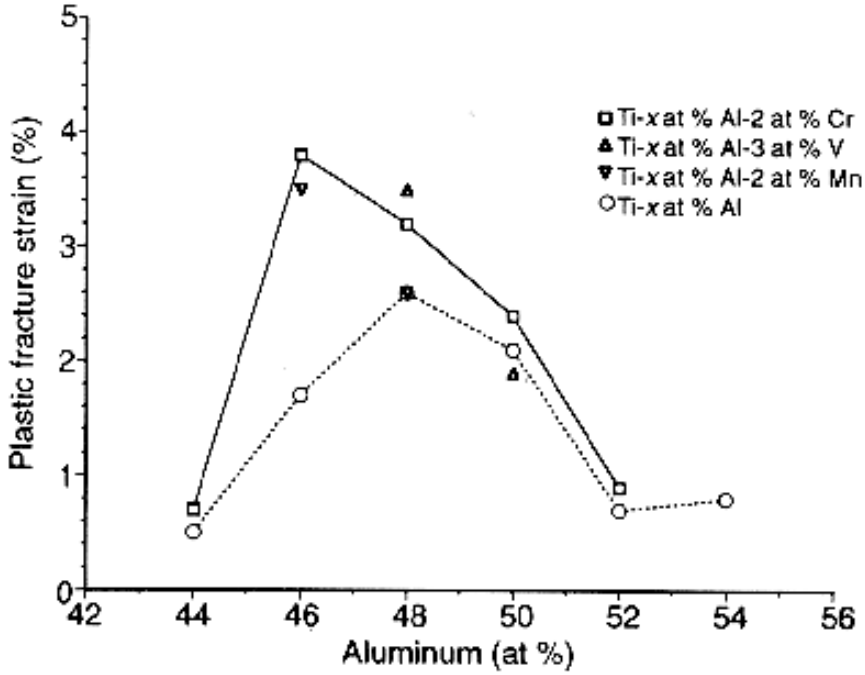

Figure 1.12: The effect of ternary additions on the ductility of γ-based alloys

to 1-3% to avoid formation of a B2 phase. V, Mn and Cr have been found to have no ductilization effects on the single phase γ structure.

The strength of γ alloys can be increased by the addition of interstitial oxygen. The effects of this addition on ductility are dependent on the oxygen concentration and on the presence of the α_2 phase [32]. Nitrogen and carbon impurities have similar effects as oxygen in that they tend to increase strength without an attendant increase in ductility. They do, however, have the advantage of reducing the creep rate.

1.3.5 Deformation

Significant progress has been made in the understanding of the basic mechanisms of deformation in TiAl. An anisotropic deformation behavior is observed in γ alloys, partly due to the tetragonal nature of the crystal structure. This tetragonality and the successive (002) planes being composed

of entirely Ti or Al atoms have important implications on the available Burgers vectors and the different stacking faults produced by partial dislocations. In the following, the mixed notation ⟨hkl] is used to indicate a set of equivalent crystallographic directions which are generated by permutations of ±h and ±k; only a sign change is allowed for l. Three deformation modes have been suggested, namely; i) slip deformation resulting from ordinary 1/2⟨110] type dislocations, ii)slip deformation due to the ⟨101] type super dislocations and iii) twinning deformation as a result of the 1/2⟨112]{111) slip system [33].

The 1/2⟨110]{111} slip system is the most energetically favored slip system, and has been observed experimentally at room temperature and also at higher temperatures. The deformation modes have been shown to be affected by temperature [34], alloying additions and Aluminum content [35]. The ductility of the TiAl alloys has been shown to be improved by twinning with 1/2⟨112]{111} type twins [33], [35]. This increase in ductility by twinning has been suggested to be due to the increase in twinning above the ductile-brittle transition temperature.

Chapter 2

GRAIN BOUNDARY SIMULATION CONCEPTS

2.1 Introduction

Studies in metals have shown that the predominant fracture mode in polycrystalline materials is intergranular fracture. The propensity for intergranular fracture has been shown to be very closely related to the type and structure of the grain boundary [36]. The mode of fracture is strongly affected by material composition, microstructure and the environment. When the fracture mode is predominantly intergranular, a polycrystal shows brittle fracture behavior. This fracture mode has been the main weakness of many advanced, high performance structural materials, such as engineering ceramics and high-temperature intermetallic compounds, as well as structural metals and alloys embrittled by impurities and or in the presence of corrosive environments. It is thus meaningless to discuss the mode of fracture, be it inter or intragranular, without specifying the grain boundary character, misorientation, purity or testing environment. The structure of grain boundaries not only affects fracture modes, but also diffusion, grain boundary sliding and slip transfer. The energy of the boundary plays an important role in segregation, precipitation and corrosion.

The basic characteristic of any interfacial system, such as a grain boundary, is that they are intrinsically inhomogeneous. In systems where an interface exists, the region surrounding the defect can exhibit very different properties from those found in the bulk. It is thus obvious that in order to attain any basic understanding of the interfacial properties, the local behavior of the interfacial region must be accounted for. Since the interface, in this case the grain boundary region, is only a few atomic layers thick, calculations of local properties necessarily require details of atomic forces and displacements. This information can be obtained using atomistic simulations, where the the

grain boundary is modeled as an assembly of particles interacting via interatomic forces.

2.2 Grain Boundary Structure

A grain boundary can be described as a planar interface between two crystals with different orientations in space or translated with respect to each other. The grain boundary can be characterized into five macroscopic and four microscopic geometrical parameters, Figure 2.1. The orientation relationship between the two crystals is given macroscopically by the rotation axis, Ψ, the rotation angle Θ and the boundary plane normal, n. The four microscopic parameters alloy for the rigid body translation of the crystals relative to each other, τ and for the shift of the boundary plane in the direction of its normal. There are two types of boundaries, namely twist and tilt boundaries, whose rotational axes give rise to a misorientation that is either parallel or perpendicular to the grain boundary respectively.

It is generally held that the grain boundary proper is a region where the coordination of atoms differs from that of the perfect lattice and this region has a finite thickness. The structure at the interface between two crystals is specific and differs from the structure of the bulk. The properties at these regions also differ from those of the bulk. As such, the grain boundary can be studied as an individual phase.

2.2.1 Geometric Models of Boundary Structure

Many models of grain boundary structure have been proposed in the literature to describe the atomic mismatch at the boundary [37] [38][39]. Since the 1940's, when Burgers and Bragg proposed a dislocation model of low angle grain boundaries, the idea has been expanded to include other boundaries. This model is based on the mismatch at the boundaries being accommodated by a periodic network or array of lattice dislocations in the plane of the boundary. One of the major drawbacks of this model is the non-inclusion of any rigid body translations between crystals.

A model which has received much success in the interpretation of experimental data is the coincidence site lattice (CSL) model [37] [38]. This is the model upon which the present work is

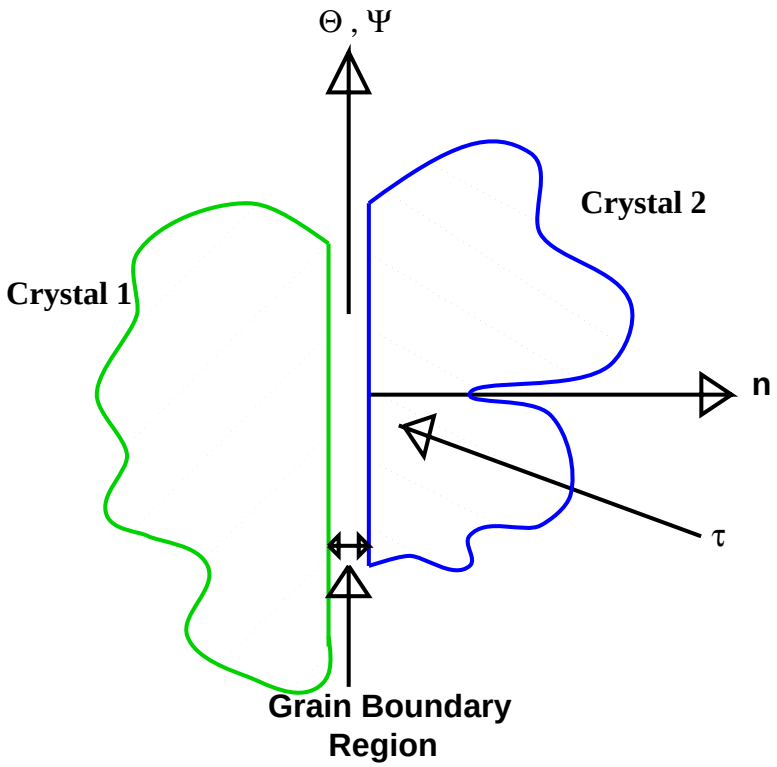

Figure 2.1: The geometrical parameters which define a grain boundary

based. The CSL model can be visualized as hypothetically inter-penetrating two crystal lattices in space to form a superlattice. By bringing a lattice point from each crystal into coincidence and rotating the crystals relative to each other, special orientations can result, called coincidence orientations, where a lattice of coincident sites exists. This lattice of coincidence sites is termed the CSL, Figure 2.2. Insertion of a plane into this lattice and removal of atoms from one crystal from one side of the plane and atoms from the other crystals on the opposing side gives rise to a grain boundary. The fraction of atoms in coincidence is known as the density of coincidence sites. The reciprocal of this density, Σ, is the commonly used parameter to describe a coincidence site boundary. Examples are given for the 210 and 310 $\Sigma = 5$ symmetrical tilt boundaries Figures 2.3 and 2.4. Boundaries with low Σ values and parallel to low index planes of the CSL have been shown to exhibit special properties such as low energies and to also be periodic.

The secondary grain boundary dislocation model states that if the relative orientation between

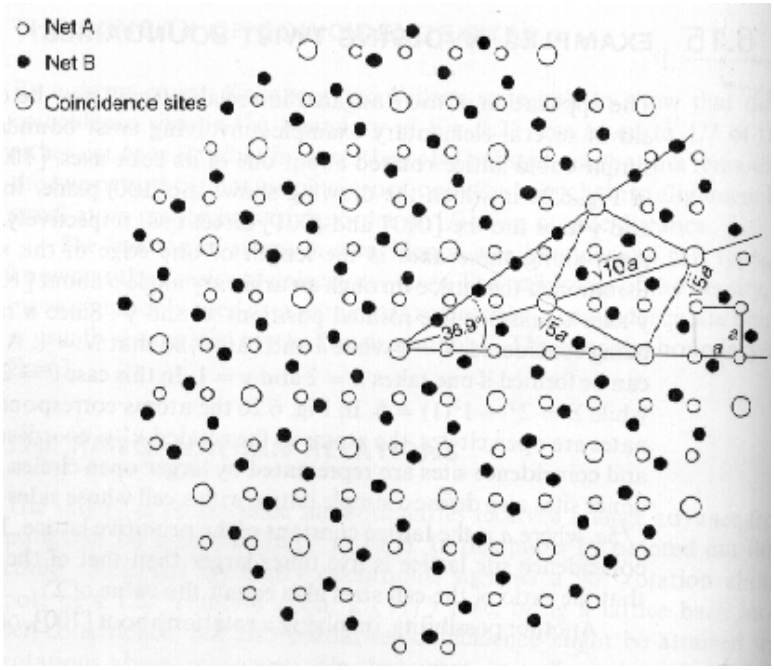

Figure 2.2: A $\Sigma = 5$ coincidence site twist boundary obtained by rotation about a $\langle 001 \rangle$ axis of a simple cubic crystal.

the two crystals is slightly deviated from the coincidence orientation the structure of the boundary relaxes to that of the coincidence boundary with a network of secondary grain boundary dislocations superimposed onto it. The Burgers vectors of these secondary grain boundary dislocations are not lattice vectors, but are vectors of the displacement shift complete lattice (DSCL). This lattice can be viewed as the coarsest lattice which contains both crystal lattices of the interpernetrated lattices as sublattices. It is the coarsest lattice of the CSL as shown in Figure 2.2. If one crystal is displaced by a vector of the DSCL, the CSL pattern will be maintained, but a shift in the origin of the CSL may result. At the boundary, a rigid body translation by an element of the DSCL restores the periodic boundary structure of the CSL, but a translation which is not an element of the DSCL destroys the periodicity of the structure.

The O-lattice theory is a generalized extension of the CSL which considers the coincidence of interior cell points of the two crystals. The coincidences, O-elements, which comprise the O-lattice are described as interior coordinates of a point of any cell of one lattice being identical to the interior

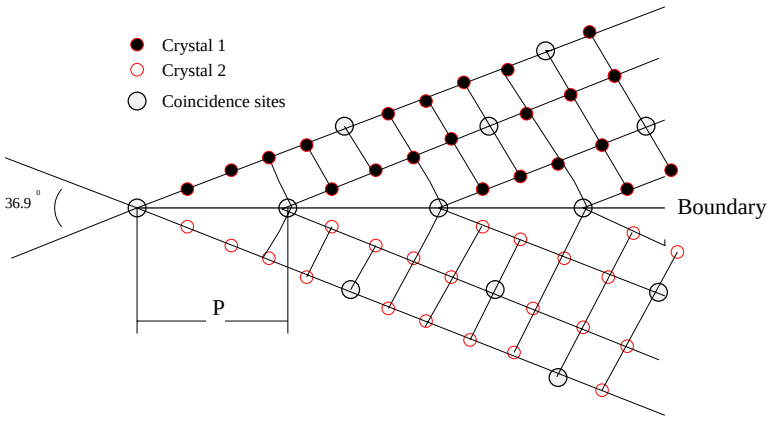

Figure 2.3: A $\Sigma = 5(210)$ coincidence site tilt boundary obtained by a 53.1^o rotation about a $\langle 001 \rangle$ axis of a simple cubic crystal. P, the structural periodicity is equal to the edge of the CSL

coordinates of that same point measured relative to the cell of the other lattice. The O-lattice, unlike both the CSL and DSCL, is dependent on the choice of lattice deformation, and this is the reason why the CSL and DSCL models are believed to be more physically significant.

2.3 Experimental Observations of Grain Boundary Structure

Experimentally, there are many difficulties faced in the investigation of the structure-property correlations of grain boundaries due to the small size of the boundary region. The technique of high resolution electron microscopy (HREM) can provide information about the atomic structure of grain boundaries which is currently unattainable by any other experimental method. HREM provides a resolution of approximately one interatomic distance. It is possible to measure rigid body translations of two adjoining crystals, as well as determine the local atomic positions at the boundary. With this technique, it is also possible to study the morphology of the boundary plane, the orientation relationships and compositional ordering.

The drawbacks to this technique include the sample preparation of very thin crystals of the order of 100Å and the precise alignment of the boundary plane to ensure unambiguous results. The major limitation of HREM is that no atomic structural variations in the direction of the beam are observable since this technique gives only the projection of structure of the boundary.

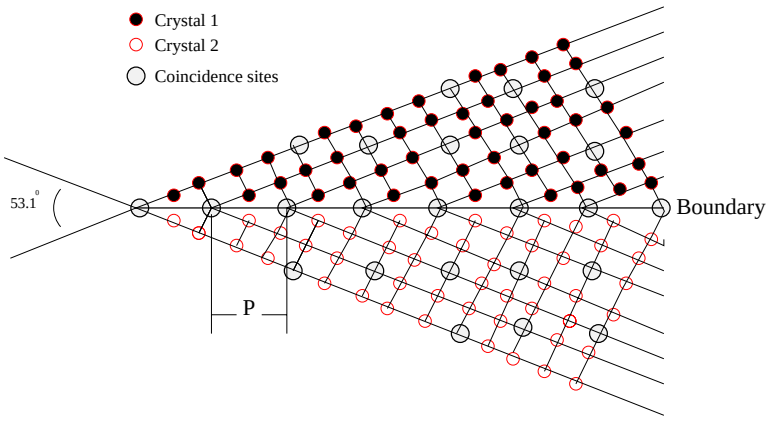

Figure 2.4: A $\Sigma = 5(310)$ coincidence site tilt boundary obtained by a 36.9^o rotation about a $\langle 001 \rangle$ axis of a simple cubic crystal. P, the structural periodicity is equal to the diagonal of the CSL

A number of HREM studies have been carried out in metals and in alloys. This research in ordered alloys has been mainly focused on the fcc based alloys, especially Ni_3Al and other $L1_2$ compounds. Of the B2 compounds, the only work currently available to compare with the simulations carried out in this work is that of Fonda and Luzzi [40] who have studied the $\Sigma = 5(310)[001]$ grain boundary in NiAl using high resolution electron microscopy (HREM). Work also exists for $\Sigma = 3(111)$ in NiAl [41] and the $\Sigma = 6(121)$ in TiAl [42].

2.4 Atomistic Simulations of Grain Boundary Structure

Despite the experimental validation of the existence of special boundaries as predicted by the geometric models, they do not successfully describe the energetics or the detailed atomic structure of the boundary. Computer simulations, on the other hand, allow for the energy minimization of a large number of atoms to give a stable boundary structure. The models, such as the CSL, do serve the purpose of providing the favored periodic boundaries for the computer simulations.

Early investigations of grain boundary structure in intermetallics were based on geometric and crystallographic concepts [43] [44]. Extensive atomistic studies of grain boundary structure of intermetallics have been carried out especially for the $L1_2$ structure using pair potentials [45] and local volume (embedded atom) potential [46] [47] [48]. These potentials were all empirically

fitted to reproduce properties of the respective alloys. Interactions of grain boundaries with lattice dislocations have also been studied atomistically [49].

From a conceptual standpoint, three basic properties are required to predict the properties of the boundary system atomistically, namely; interatomic interaction potentials, boundary conditions for the modeled system and a method of simulation.

2.4.1 Embedded Atom Method and Interatomic Potentials

For a detailed understanding of the atomic behavior of metals and intermetallics, specific atomistic processes must be considered. The Embedded Atom Method (EAM) was developed to handle atomistic calculations for defects, e.g. at surfaces and interfaces. The EAM is a semi-empirical method based on electron density theory. It has been shown to accurately describe a large number of properties in metals and intermetallics.

Atomistic simulations are achieved by the description of the interaction between atoms, mediated by electrons, at the atomic level. This atomic interaction is, in most cases, based on a simple analytical expression which contains one or more parameters adjusted to experimental data. The development of interatomic potentials for a given material involves, first, an expression for the total potential energy of the system which depends on the particle positions and secondly, the dependence of this energy on the particle positions is fitted to some experimentally determined quantities, such as the elastic constants, sublimation and vacancy formation energy of the perfect crystal and the lattice parameter at 0^oK. For binary alloys another fitting parameter, the heat of mixing, is required.

In the case of metallic bonding, pair potentials adequately describe the short-range repulsion between atoms, but not the long-range attraction required for cohesion. This pair term accounts for the classical electrostatic interaction. The attraction between ions in a metal arises from the lowering of the energy of the electron gas when embedding the ion cores in this electron gas. The corresponding embedding energy, $\mathrm{F}(\rho_i)$, can be interpreted as the energy of embedding atom i in an electron gas of density ρ_i and contains the quantum mechanical interaction between the embedded atom and the host atom. The EAM local-volume dependent potentials proposed by Daw and

Baskes [50] adequately describe this long-range attraction required for cohesion. The term local volume indicates that there is a term in the energy expression for each atom that depends on the local atomic density surrounding that atom. These are the potentials used for the atomistic simulations for this work. The model for the potentials consists of two distinct terms: a pairwise term and a local density (volume-dependent) term. The energy of an n-atomic system can be represented as

$$E = \sum_{i}^{n} E_i, \tag{2.1}$$

where the energy of atom i is given by

$$E_i = \frac{1}{2} \sum_{i,j(i \neq j)} \phi(r_{ij}) + \sum_{i} F(\overline{\rho}_i) \tag{2.2}$$

Here r_{ij} is the distance between atom i and j, ϕ is a pairwise interatomic potential, and $\overline{\rho}_i$ is the density at atomic site i due to all its neighbors,

$$\overline{\rho}_i = \sum_{j(\neq i)} \rho(r_{ij}) \tag{2.3}$$

For this study, F, the embedding functions were developed by requiring that the energy of the crystal be fit to Rose's equation of state [51] which scales the cohesive energy of most metals. This results in the agreement of the cohesive energy, lattice parameter and bulk modulus between the potentials and experiment.

When modeling a binary alloy seven functions are required: three each, obtained from fitting to properties of the pure metals; ϕ_{A-A}, ρ_A, F_A, ϕ_{B-B}, ρ_B, F_B, and one, ϕ_{A-B}, to describe the mixed pair interaction. The interatomic potentials for NiAl used in this study incorporated the Ni-Ni and Al-Al pair potentials developed by Mishin and Farkas [52] that were empirically fit to self-diffusion data in pure Ni and Al. The electron density functions and embedding functions for both Ni and Al were those developed by Voter and Chen [53]. The mixed Ni-Al potentials differ from those of Voter and Chen and were fit specifically to the properties of B2 NiAl [54]. The Fe-Fe potential utilized for the grain boundary computations was developed by Simonelli et al. [55]. The EAM

interatomic potentials used for Co interaction were developed by Pasianot and Savino [56], who took into account the restrictive relations imposed on the elastic constants by the EAM, as well as the inner elastic constants' contribution in hexagonal materials. The necessary mixed potentials, Co-Al, Fe-Al and Ni-Al were fit to the properties of the B2 phase in each system. Details of the fitting procedure are discussed elsewhere [52] [57] [58]. The set of potentials used renders all three compounds as triple-defect compounds in agreement with experimental results. They thus correctly predict the point defects that accommodate off-stoichiometry, namely antisites on M-rich side and vacancies on Al-rich side. For the work on TiAl, the Ti potentials were those of Pasianot and Savino [56] who accounted for the contribution of the inner elastic constants. The electron density and embedding functions for Al were again those developed by Voter and Chen [53]. The mixed Ti-Al potential, which reproduces the properties of $L1_0$ TiAl, was that developed by Farkas [54].

Limitation of the EAM Technique

The EAM technique is adequate for the description of the properties of most metallic materials, but it fails in cases where the Cauchy relation for the metal or alloy is negative and for covalent materials. For covalent materials, the strong directional bonding needs to be accounted for. This can be achieved by angular consideration in the electronic density function. Of the number of techniques proposed to overcome this limitation of the EAM technique in treating angular-dependent forces, the embedded defect method (EDM) [59] is the simplest approach.

2.4.2 Simulation Procedure

As mentioned in section 2.1, interfacial systems are composed of two coupled regions, the interface and the surrounding bulk. It is, therefore, important in atomistic simulations to properly formulate the boundary conditions such that the size is optimized for minimum computational time without allowing the artificial perturbation of the defect by the boundary conditions, and thereby compromising the realistic modeling of the interaction of the interface and the bulk.

The atomistic simulations for this study were carried out using "molecular statics". This method allows the zero-temperature relaxed structure determination of a simulation system by minimization

of the potential energy, E_i. The total energy of the block is minimized with respect to local displacements of the atoms from their initial positions.

In our simulation studies of the grain boundaries, the first step was the generation of the perfect lattice based on information of the bravais lattice of the material and repeating this along the cartesian coordinates. The lattice parameters determine the length of the orthogonal vectors. The initial configurations of the grain boundaries are then constructed by overlapping two infinite perfect crystals and performing the appropriate rotation, θ, about an axis, $[hkl]$, to achieve the desired misorientation. After the defect introduction, boundary conditions are imposed. A computational block is generated, as shown in Figure 2.5, consisting of two parts, "Region I" and "Region II". "Region I" is the interfacial area that includes the grain boundary, and it consists of atoms that are free to move according to interactions defined by the potentials. This region is at least $100\mathring{A}$ in length. The atoms in "Region II", are fixed on normal lattice sites and influenced by the long range elastic interactions of the defect. These atoms interact with neighboring atoms in "Region I", but their coordinates do not change. The boundary conditions in the boundary plane, the X and Z directions, are periodic, while those in the direction perpendicular to the boundary plane, Y direction, are fixed.

Relaxation of the atoms within the interfacial area, "Region I", is achieved by the conjugate gradient method. This minimization technique moves the atoms from their initial position towards the direction with the steepest gradient, ie. the direction in which the rate of energy decrease is a minimum. This movement occurs until the energy gradient is zero. On obtaining the lowest energy position, the process of atom movement in a perpendicular direction occurs. This iteration procedure continues, until no further decrease in energy is possible by movement in a perpendicular direction. The total potential energy of the block is determined by considering all the possible pairs within the cut-off radius of the the potentials. Although the two grain are free to translate with respect to each other, the resultant translational state might not correspond to the lowest energy configuration. To find the global minima, it is essential to apply rigid body translations of the two grains.

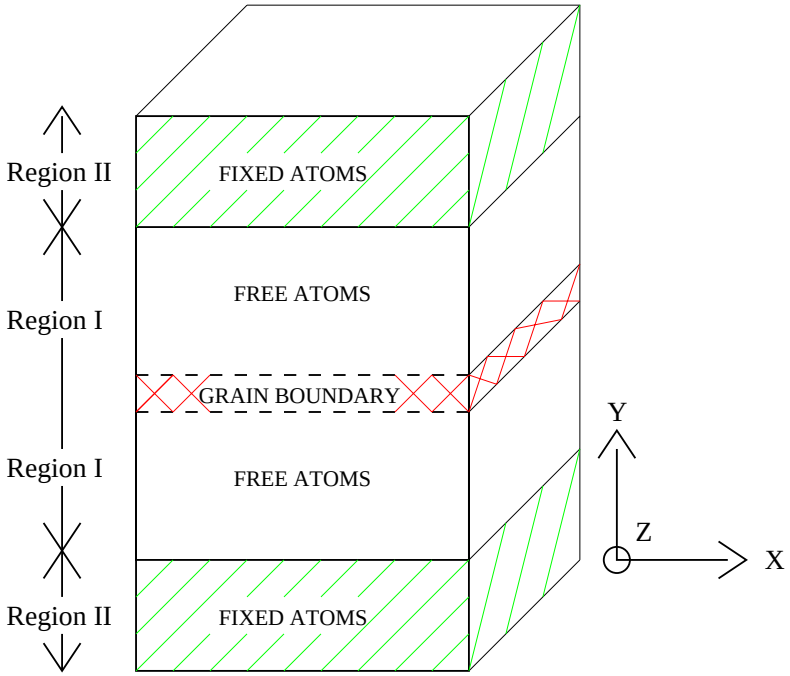

Figure 2.5: A schematic of the simulation block. The simulation cell has periodic boundary conditions in X and Z directions and fixed boundary conditions in Y, normal to the boundary plane.

Chapter 3
POINT DEFECTS

3.1 Introduction

To understand high temperature mechanical deformation, an understanding of point defect behavior of these alloys is important because they not only form the basis for diffusion assisted processes such as creep, but it has also been shown that the mechanical strength of the ordered alloys under study can be greatly influenced by deviations from stoichiometry. This departure from exact stoichiometry is accommodated by structural defects. It has thus been suggested that the increase in strength is attributable to the increase of either the substitutional antisites or the structural vacancies with increasing deviation from stoichiometry. It is also possible that certain point defects or combinations of defects decrease atomic mobility while others increase it. Furthermore, solid solution alloying will affect defect concentrations and thus play an important role in the mechanical behavior at elevated temperatures.

The formation of defect structures allows for the large range of deviations from the stoichiometric composition. The knowledge of point defect energetics is essential for the proper calculation of the formation (excess) energy of extended defects, such as grain boundaries, with local off-stoichiometry in the defect core. The deviation is accomplished by either vacancies on the sublattice sites of the deficient element or antisite of the element in excess. Many compounds have a defect structure that is different on either side of stoichiometry. Deviations from stoichiometry in the B2 aluminides under question are accomplished, in transition metal-rich compositions by antisite atoms and in the Al-rich compositions by the excess Al atoms filling normal transition metal sites and the creation of transition metal vacancies. Conversely, deviations from stoichiometry in TiAl are accomplished by antisite atoms on both sides of stoichiometry. These factors make the atomistic simulation of

point defects very important.

It is important to note that when defects are simulated in a crystal using "molecular statics", the energy obtained, the "raw" energy, is not the true formation energy of the defect but rather an energy calculated by using a perfectly ordered (stoichiometric) crystal as the reference state. This energy is used to derive the true formation energy of the defect according to its proper thermodynamic definition. This conversion of energy from the "raw" to the true energy is facilitated by knowledge of the chemical potentials of the components of the system slightly deviated from exact stoichiometry and at zero temperature. The proper calculation of the chemical potentials, according to their thermodynamic definition requires the formation energies of the constitutional defects that accommodate the deviation of the system from stoichiometry. Mishin and Farkas [52] made a detailed study for triple defect compounds with emphasis on the NiAl system. The following sections (3.2 and 3.3) summarize this work [52].

3.2 Energy Calculations of Defects with Local Off-stoichiometry

The proper calculation of the excess energy of a crystalline defect in a binary compound is not trivial. For a stoichiometric binary compound, AB, with a point defect in the compound, the thermodynamically correct definition of the defect formation energy at zero temperature is:

$$\varepsilon = \left(\frac{\partial E}{\partial N_{pd}} \right)_{N_A, N_B} \tag{3.1}$$

Where E is the total energy of a crystal containing N_A atoms of A and N_B atoms of B, N_{pd} is the number of point defects of a given type in the crystal. This means that the formation energy of a defect equals the change in the total energy due to the introduction of one point defect provided that the number of atoms of each species in the system is fixed.

In theory the formation energy of a defect, using "molecular statics," is derived from the difference in relaxed energy δE of the perfect block and one which contains the constitutional point defect; assuming that they both contain the same number of A and B atoms.

$$\varepsilon = \delta E \tag{3.2}$$

In practice, however, the creation of a defect in a simulation block is achieved by first generating a perfectly stoichiometric block with equal number of A and B atoms. The defect is achieved by displacement, removal and or replacement of atoms followed by the energy minimization of the block using molecular statics. This usually results in the number of A and B atoms in the defected block being different from those in the perfect block. The energy difference, $\delta\varepsilon^*$, thus derived is different from δE defined in eqn. 3.2. This "raw" energy, $\delta\varepsilon^*$, can be recalculated into the true energy, δE, consistent with the thermodynamic definition given by eqn. 3.1 by the following thermodynamic relation

$$\delta E = \delta\varepsilon^* - \mu_A \delta N_A - \mu_B \delta N_B \tag{3.3}$$

where μ_A and μ_B are the chemical potentials of the two species of atoms at zero temperature. The chemical potentials are related to ε_c and $\Delta\mu$ by

$$\varepsilon_c = (\mu_A + \mu_B)/2 \tag{3.4}$$

$$\Delta\mu = \mu_A - \mu_B \tag{3.5}$$

where ε_c is the cohesive energy of a perfect crystal per atom and $\Delta\mu$ is the difference in chemical potentials. Using these equations, the chemical potentials, and subsequently eqn. 3.3, can be expressed in terms of ε_c and $\Delta\mu$.

$$\delta E = \delta\varepsilon^* - \varepsilon_c \left(\delta N_A + \delta N_B\right) - \frac{\Delta\mu}{2} \left(\delta N_A - \delta N_B\right) \tag{3.6}$$

For cases where an equal number, δN , of A and B atoms (ie.$\delta N_A = \delta N_B \equiv \delta N$) are added or removed in the creation of the defect, the stoichiometry of the block is maintained. Eqn. 3.6 becomes

$$\delta E = \delta\varepsilon^* - 2\varepsilon_c \delta N. \tag{3.7}$$

In such cases the calculation of the true formation energy of the defect only requires the "raw" energy and the cohesive energy of the perfect crystal, which are both readily available from the

simulations. Eqn. 3.6 becomes

$$\delta E = \delta\varepsilon^* - \Delta\mu\delta N \tag{3.8}$$

in situations where $\delta N_A = -\delta N_B \equiv \delta N$. This usually implies substitution of one type by another and results in the conservation of the total number of atoms in the block, but achieves local off-stoichiometry. In these cases the difference in chemical potentials is required for calculation of the true formation energy of the defect.

In this study, we consider four binary compounds of the form AB where A=M and B=Al where M is Fe, Ni, Co or Ti for FeAl ,NiAl, CoAl or TiAl respectively. Tables 3.1 & 3.4 show the expressions of both the true formation energies and chemical potentials in terms of the "raw" energies for the B2 compounds (3.2) and TiAl respectively (3.5). The calculated values are shown in Tables 3.3 & 3.6.

3.3 Chemical Potentials

In the past, in the calculation of chemical potentials, it was assumed that the energy contributed by a mixed pairwise bond, the cohesive energy, ε_{coh}, is distributed equally among the two elements. Gao and Bacon pointed out that the chemical potential thus described is unique as long as the embedding function is uniquely defined [60]. Requiring that the embedding function be fit to Rose's equation of state, [51], ensure's its unique definition. The chemical potentials of the two species of atoms, μ_{Al} and μ_M, were calculated using this assumption. In the present work, we use the thermodynamically consistent method of calculating the chemical potentials in atomistic simulations proposed by Hagen and Finnis [61]. This method does not affect stoichiometric simulation blocks, since only the sum of the chemical potentials, ε_{coh}, is required (eqn. 3.7). For off-stoichiometric systems, however, the difference between the chemical potentials is required (eqn. 3.8).

Hagen and Finnis assume that in such cases the chemical potentials are functions of the formation energies of the predominating structural point defects that accommodate the departure from stoichiometry. It follows from this assumption that the energy of the point defect that ac-

commodates the deviation from stoichiometry is zero. The chemical potentials thus derived are composition-dependent and show a discontinuity at the 50/50 composition.

A result of using this technique is the energy dependence of the various defects on the stoichiometry of the total block. Off-stoichiometric boundary and free surface energies will greatly depend on the composition of the block that contains them. Tables 3.3 & 3.6 give the chemical potentials and the true formation energies.

3.4 Simulation Procedure

The atomistic simulations for this study were carried out using "molecular statics". This method allows the zero-temperature relaxed structure determination of a simulation system by minimization of the potential energy. The total energy of the block is minimized with respect to local displacements of the atoms from their initial positions.

The first step in the simulation of the structural point defects is the generation of the perfect crystal structure from a specific initial configurations. Periodic boundary conditions were used in all directions. The structural point defects were generated by either removing an atom to create a structural vacancy or by substituting the appropriate element to create a substitutional antisite, at the center of the simulation block and then allowing the block to relax around the defect. The energy of the defect is then calculated from the difference in energy of the block with and without the point defect.

3.5 B2 Compounds

It has been suggested that not only single defects (the formation of A_β antisites in A-rich alloys and B_α antisites in B-rich alloys), but triple defects (the formation of A_β antisites in A-rich alloys and V_α vacancies in B-rich alloys) are possible even at stoichiometry. The triple-defect mechanism is the formation of constitutional vacancies on the transition metal, M, sites in Al-rich compounds and the creation of M constitutional antisites on Al sites in Al-deficient compounds, that is two vacancies on one sublattice site with an antisite atom on the other sublattice.

Table 3.1: Expressions for the chemical potentials and the true formation energies of point defects in B2 Compounds (M-Al).

	M-rich alloy	Al-rich alloy
μ_{M}	$\varepsilon_{\mathrm{c}} + \varepsilon^*_{\mathrm{M_{Al}}}/2$	$-\varepsilon^*_{\mathrm{V_M}}$
μ_{Al}	$\varepsilon_{\mathrm{c}} - \varepsilon^*_{\mathrm{M_{Al}}}/2$	$2\varepsilon_{\mathrm{c}} + \varepsilon^*_{\mathrm{V_M}}$
$\Delta\mu$	$\varepsilon^*_{\mathrm{M_{Al}}}$	$-2(\varepsilon_{\mathrm{c}} + \varepsilon^*_{\mathrm{V_M}})$
$\varepsilon_{\mathrm{V_M}}$	$\varepsilon_{\mathrm{c}} + \varepsilon^*_{\mathrm{V_M}} + \varepsilon^*_{\mathrm{M_{Al}}}/2$	0
$\varepsilon_{\mathrm{V_{Al}}}$	$\varepsilon_{\mathrm{c}} + \varepsilon^*_{\mathrm{V_{Al}}} - \varepsilon^*_{\mathrm{M_{Al}}}/2$	$2\varepsilon_{\mathrm{c}} + \varepsilon^*_{\mathrm{V_{Al}}} + \varepsilon^*_{\mathrm{V_M}}$
$\varepsilon_{\mathrm{M_{Al}}}$	0	$2(\varepsilon_{\mathrm{c}} + \varepsilon^*_{\mathrm{V_M}}) + \varepsilon^*_{\mathrm{M_{Al}}}$
$\varepsilon_{\mathrm{Al_M}}$	$\varepsilon^*_{\mathrm{M_{Al}}} + \varepsilon^*_{\mathrm{Al_M}}$	$-2(\varepsilon_{\mathrm{c}} + \varepsilon^*_{\mathrm{V_M}}) + \varepsilon^*_{\mathrm{Al_M}}$

Table 3.2: Point defect "raw" energies (in eV) in the B2 aluminides.

Point defect	CoAl	NiAl	FeAl
V_M	5.686	5.978	5.329
V_{Al}	5.942	5.471	5.486
M_{Al}	-0.512	-0.920	-0.761
Al_M	4.091	3.457	2.719

It is well established, experimentally [62], [63], that the B2 aluminides under study; FeAl, NiAl and CoAl accommodate the deviation from stoichiometry via the triple-defect mechanism as is the case for NiAl which has two vacancies on the Ni sites and a Ni atom at the Al site. These triple defects would explain the anomalously low formation energies for vacancies, that were calculated assuming single vacancy formation and the very high concentrations of vacancies present at elevated temperatures. For example, in FeAl at 1073 K the thermal vacancy concentration is forty times greater than in a pure metal at its melting point and in Al-rich compositions constitutional vacancies may occupy up to 10% of lattice sites, mostly on the Fe sublattice [64]. Stoichiometric NiAl on the other hand, has similar vacancy concentrations as pure metals at high temperatures. A large number of vacancies can be retained on quenching from elevated temperatures, as in FeAl.

Cooling rate after annealing affects ductility by retention of a large number of vacancies after quenching as seen in FeAl. The number of retained vacancies increases with increasing annealing temperature. This increase leads to an increase in yield strength and probability of intergranular

Table 3.3: Chemical Potentials and true formation energies (in eV) of point defects in the B2 aluminides.

		CoAl	NiAl	FeAl
Al-rich alloy	μ_M	-5.686	-5.978	-5.329
	μ_{Al}	-3.001	-3.010	-2.989
	$\Delta\mu$	-2.434	-2.968	-2.340
	$\varepsilon_{\mathrm{V_M}}$	0	0	0
	$\varepsilon_{\mathrm{V_{Al}}}$	2.690	2.461	2.497
	$\varepsilon_{\mathrm{M_{Al}}}$	1.922	2.048	1.579
	$\varepsilon_{\mathrm{Al_M}}$	1.657	0.489	0.379
Al-deficient alloy	μ_M	-4.953	-4.954	-4.539
	μ_{Al}	-4.035	-4.034	-3.778
	$\Delta\mu$	-0.512	-0.920	-0.761
	$\varepsilon_{\mathrm{V_M}}$	0.961	1.024	0.790
	$\varepsilon_{\mathrm{V_{Al}}}$	1.729	1.437	1.708
	$\varepsilon_{\mathrm{M_{Al}}}$	0	0	0
	$\varepsilon_{\mathrm{Al_M}}$	3.579	2.537	1.958

fracture and a decrease in ductility. [65].

Table 3.1 shows the expressions of both the true formation energies and chemical potentials in terms of the "raw" energies for the B2 compounds The calculated values are shown in Table 3.2 where as Table 3.3 gives the chemical potentials and the true formation energies for these compounds.

3.6 TiAl

For most intermetallic compounds, deviations from the stoichiometric composition are accommodated by antisite atoms, as is the case for TiAl. Unlike the B2 compounds, deviations from stoichiometry in TiAl are accommodated by the formation of antisites on both sides of stoichiometry; Ti_{Al} antisites in Ti-rich alloys and Al_{Ti} antisites in al-rich alloys [66] [67]. This absence of structural vacancies has been verified for TiAl using positron annihilation [66]. Thermal vacancies do however form at high temperatures. Table 3.4 shows the expressions of both the true formation energies and chemical potentials in terms of the "raw" energies for TiAl. The calculated values are

Table 3.4: Expressions for the chemical potentials and the true formation energies of point defects in γ-TiAl.

	Ti-rich alloy	Al-rich alloy
μ_{Ti}	$\varepsilon_{\mathrm{c}} + \varepsilon^*_{\mathrm{Ti_{Al}}}/2$	$\varepsilon_{\mathrm{c}} - \varepsilon^*_{\mathrm{Al_{Ti}}}/2$
μ_{Al}	$\varepsilon_{\mathrm{c}} - \varepsilon^*_{\mathrm{Ti_{Al}}}/2$	$\varepsilon_{\mathrm{c}} + \varepsilon^*_{\mathrm{Al_{Ti}}}/2$
$\Delta\mu$	$\varepsilon^*_{\mathrm{Ti_{Al}}}$	$-\varepsilon^*_{\mathrm{Al_{Ti}}}$
$\varepsilon_{\mathrm{V_{Ti}}}$	$\varepsilon_{\mathrm{c}} + \varepsilon^*_{\mathrm{V_{Ti}}} + \varepsilon^*_{\mathrm{Ti_{Al}}}/2$	$\varepsilon_{\mathrm{c}} + \varepsilon^*_{\mathrm{V_{Ti}}} - \varepsilon^*_{\mathrm{Al_{Ti}}}/2$
$\varepsilon_{\mathrm{V_{Al}}}$	$\varepsilon_{\mathrm{c}} + \varepsilon^*_{\mathrm{V_{Al}}} - \varepsilon^*_{\mathrm{Ti_{Al}}}/2$	$\varepsilon_{\mathrm{c}} + \varepsilon^*_{\mathrm{V_{Al}}} + \varepsilon^*_{\mathrm{Al_{Ti}}}/2$
$\varepsilon_{\mathrm{Ti_{Al}}}$	0	$\varepsilon^*_{\mathrm{Ti_{Al}}} + \varepsilon^*_{\mathrm{Al_{Ti}}}$
$\varepsilon_{\mathrm{Al_{Ti}}}$	$\varepsilon^*_{\mathrm{Ti_{Al}}} + \varepsilon^*_{\mathrm{Al_{Ti}}}$	0

Table 3.5: Point defect "raw" energies (in eV) in γ-TiAl.

Point defect	TiAl
V_{Ti}	6.206
V_{Al}	5.143
Ti_{Al}	-1.033
Al_{Ti}	1.811

shown in Table 3.5 where as Table 3.6 gives the chemical potentials and the true formation energies for this compound.

Table 3.6: Chemical potentials and true formation energies (in eV) of point defects in γ-TiAl.

	Ti-rich alloy	Al-rich alloy
μ_{Ti}	-4.906	-5.295
μ_{Al}	-3.873	-3.484
$\Delta\mu$	-1.033	-1.811
$\varepsilon_{\mathrm{V_{Ti}}}$	1.301	0.912
$\varepsilon_{\mathrm{V_{Al}}}$	1.271	1.660
$\varepsilon_{\mathrm{Ti_{Al}}}$	0	0.778
$\varepsilon_{\mathrm{Al_{Ti}}}$	0.778	0

Chapter 4

ATOMISTIC STRUCTURE OF HIGH INDEX SURFACES

4.1 Introduction

Atomistic simulations of surface structure in metals and alloys have been carried out for many years. Recent calculations of surface energies and surface relaxation use a local volume term in the interatomic potential either in the manner of Finnis and Sinclair [68] or that of Daw and Baskes' embedded atom method [50]. One of the main achievements of these methods is the successful prediction of experimental surface relaxation behavior [50, 69].

The question of surfaces in ordered materials poses particular interest and challenges, since variations in composition are possible when considering the surface with respect to the bulk. The details of surface structure and composition are very important in a number of practical applications of intermetallic compounds. These range from the role of surfaces in the fracture process, to corrosion properties, diffusion and the role of surfaces in the bulk mechanical behavior of intermetallics. In these compounds the same crystallographic surface may occur with different terminations, giving rise to several possible structures for the same surface orientation. These effects are similar to those observed in grain boundaries in intermetallics where several different structures are possible for the same crystallographic grain boundary and the degree of order and composition may differ from that of the bulk. We present here atomistic simulations of the structure and energy of high index surfaces in bcc and fcc based pure and ordered materials. The pure materials studied were Fe and Al. The bcc-based FeAl and NiAl, with a B2 structure and the fcc-based γ TiAl with an $L1_0$ structure were the ordered materials studied. The results are compared with a simple structural unit model for high index surfaces.

4.2 Interatomic potentials and simulation technique

The interatomic potentials for NiAl used in this study incorporated the Ni-Ni and Al-Al pair potentials developed by Farkas et al [58]. The electron density functions and embedding functions for both Ni and Al were those developed by Voter and Chen [53]. The mixed Ni-Al potentials differ from those of Voter and Chen and were fit specifically to the properties of B2 NiAl [58]. The Fe-Fe potential utilized for the surface computations was developed by Simonelli et al. [55]. The necessary mixed potentials for Fe-Al were fitted to the properties of the B2 compound [70]. For the work on TiAl, the Ti potentials were those of Pasianot and Savino [56] who accounted for the contribution of the inner elastic constants. The electron density and embedding functions for Al were again those developed by Voter and Chen [53]. The mixed Ti-Al potential, which reproduces the properties of $L1_0$ TiAl, was that developed by Farkas [54].

The initial, unrelaxed configuration of the surface was created by rotating the perfect crystal about the [001] axis by the proper angle, θ to give the desired orientation. The surfaces were simulated using the standard molecular statics technique. The technique is the same as that used in previous work [71] and summarized in Chapter 2. The structural relaxation of the surface was achieved by means of the conjugate gradient method for the minimization of the defect energy. Periodic boundary conditions were imposed in the directions parallel to the surface plane, while fixed boundary conditions were applied normal to the plane of the surface. At least 120 crystalline planes parallel to the surface plane were included in the simulation block.

4.3 Structural unit model for surfaces

A structural unit model can be developed to model surface structure and energies in the absence of reconstruction. We summarize the main features of this model, restricting our discussion to surfaces containing the $\langle 001 \rangle$ type axis in bcc and fcc materials for simplicity. For these surfaces, structural units can be defined based on the structure of a few low energy surfaces. The structural units, called here A and B, are associated with the low index surfaces, {100} and {110} corresponding to the angles of 0^0 and 45^0, respectively. These are shown in Fig. 4.3 for a B2 compound and

in Fig. 4.8 for $L1_0$ TiAl. In our simple model, these structural units are the base structures and any surface containing the $\langle 001 \rangle$ axis can be completely described using these units. The number of these structural units can be determined *a priori* by the following relation:

$$1 \text{ period of } (hk0) = \alpha \text{ periods of } (100) + \beta \text{ periods of } (110) \tag{4.1}$$

The values of α and β are dependent on the indices, h and k. For all positive h and k, they can be calculated for h > k > 0 from the following condition:

$$[hk0] = \alpha\ [100] + \beta\ [110]$$

$$\text{This gives the result:} \quad \alpha = h - k, \qquad \beta = k$$

Using the underlying assumption that the energies are additive in the same manner as the periods, the energies of these low index surfaces can then be used to predict the energy of the higher index:

$$\gamma_{hk0} = \frac{\alpha\gamma_{100} + \beta\sqrt{2}\gamma_{110}}{\sqrt{h^2 + k^2}} \tag{4.2}$$

4.4 Results for pure metals; Fe and Al

For a particular angle, the fraction of the number of the two type of structural units present can be determined from the model and is found to be in good agreement with the simulation results. For example, using the model, the structural unit sequence at $\theta = 23.19^0$ (730) is comprised of 4 A units and 3 B units. In pure metals there is only one possible termination and thus the structural units are unique. On the basis of this model, surface energies were calculated using Eq. 4.2 and were compared with the simulated values. The results for the surface energy as a function of the orientation angle are shown in Figs. 4.1 and 4.2. The maximum difference between the simulated and calculated surface energies is 2% for both metals.

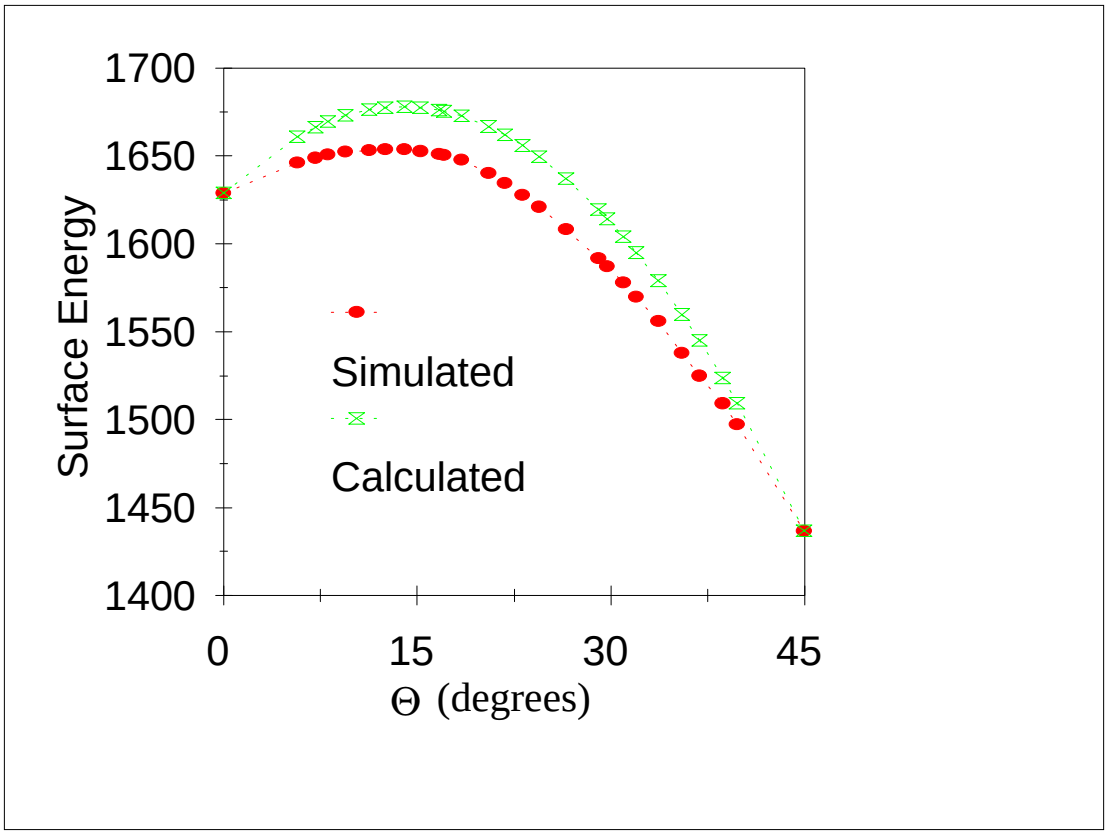

Figure 4.1: Simulated and Calculated surface energies (in mJ/m^2) of Fe as a function of orientation angle. (The dashed lines serve only as guides for the eye)

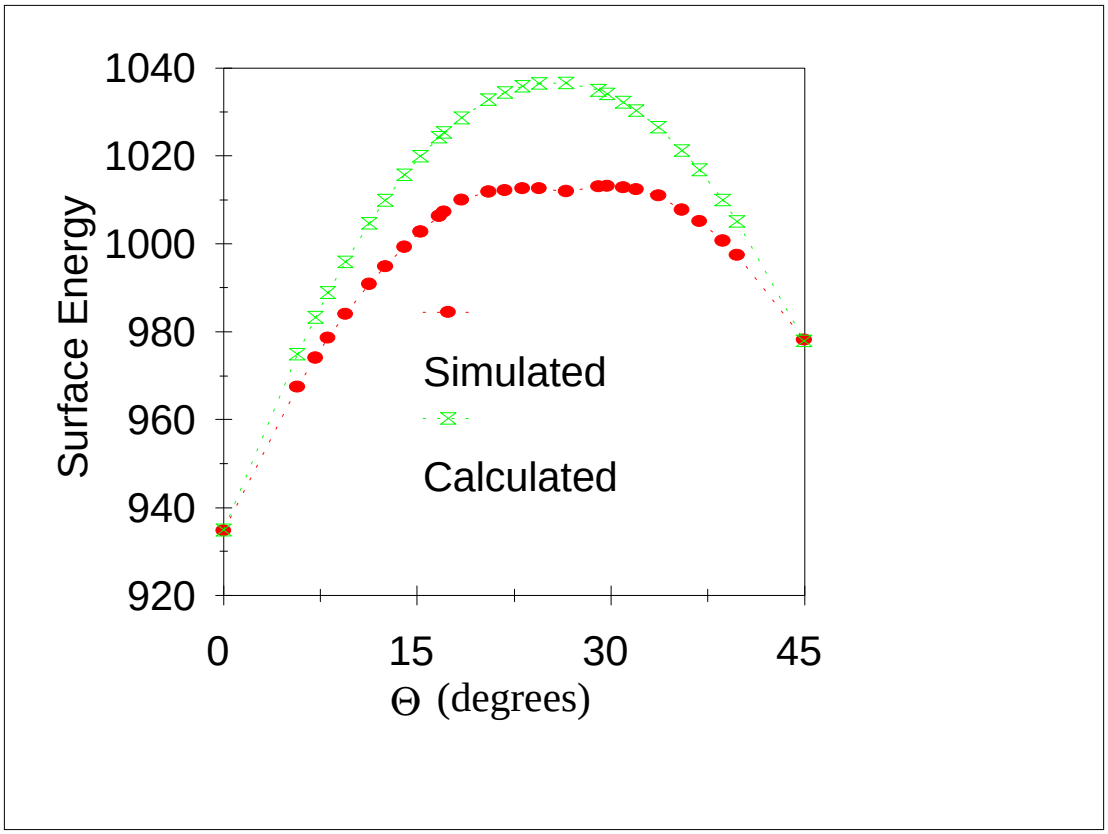

Figure 4.2: Simulated and Calculated surface energies (in mJ/m^2) of Al as a function of orientation angle. (The dashed lines serve only as guides for the eye)

4.5 Ordered alloys

The calculation of the surface energies of the ordered alloys is complicated by the different energies possible for the structural units depending on both surface composition and bulk stoichiometry. It is important to note that for these compounds, to accommodate off-stoichiometry, one of the structural units can have more than one possible termination. In this work, the energies of the off-stoichiometric surfaces are calculated using the proper method for the calculation of the chemical potentials in the alloy as described by Finnis and Hagen [61]. An important consequence of such calculations is that the surface energy depends on the bulk stoichiometry which contains the surface. The surface energies for the different terminations calculated herein, were carried out using the same bulk.

4.5.1 Results for FeAl and NiAl surfaces

The model was tested for two B2 ordered compounds; FeAl and NiAl. The study was carried out for surfaces containing the $\langle 001 \rangle$ type axis. It is important to note that for such compounds the structural unit A $\left(\text{at } \theta = 0^0\,(100)\right)$ now has two possible terminations, A_1 for the 100% Ni or 100% Fe termination (Fig. 4.3(a)), or A_2 (Fig. 4.3(b)) for the 100%Al termination. For both cases there are no real topological differences. The structural unit B $\left(\text{ at } \theta = 45^0\,(110)\right)$ is unchanged because it has only one stoichiometric termination (Fig. 4.3(c)). For the off-stoichiometric surfaces the deviation from stoichiometry is accomplished by an extra A-type unit of the same excess as the surface. For example, the surface at $\theta = 20.56^0\,(830)$ has a different combination of units depending on whether it is Al-deficient $(3A_1 + 2A_2 + 3B)$ or Al-rich $(2A_1 + 3A_2 + 3B)$ as shown in Fig. 4.4.

For stoichiometric surfaces, the number of A-type units is even and each A_1 unit is matched with an A_2 unit. This gives rise to the energy of the surface being independent of the bulk stoichiometry which contains it, since the B unit is stoichiometric and the energies of the two types of A-type units average out to give a stoichiometric energy. However, for off-stoichiometric surfaces it was observed that the number of A-type units is odd and that one of the A-type units is unmatched. The off-stoichiometric surface energy is dependent on this unmatched A-type unit since the rest

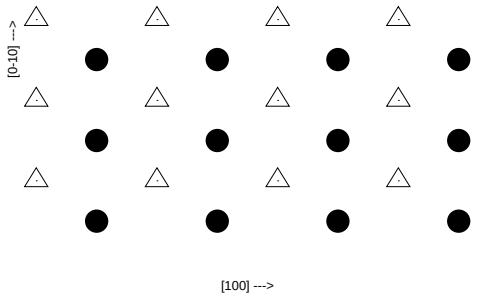

(a) unit A_1

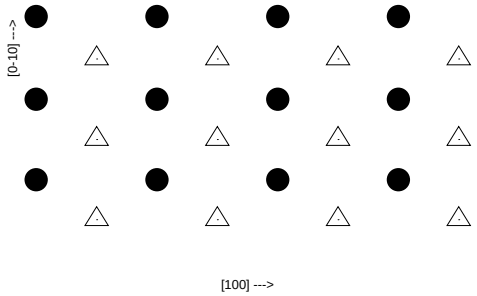

(b) unit A_2

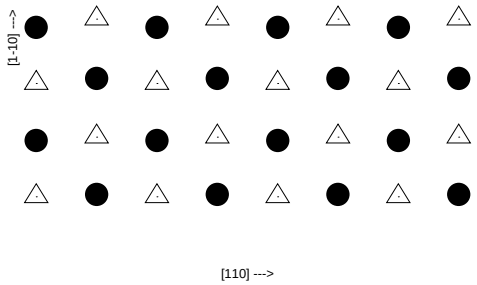

(c) unit B

Figure 4.3: Structural units for NiAl and FeAl

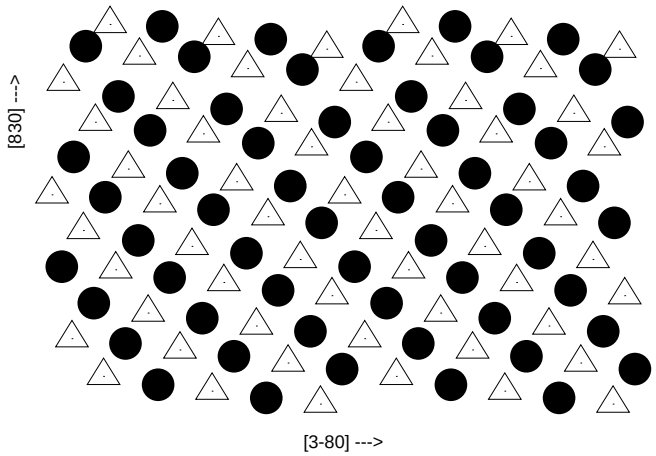

(a) Al-rich

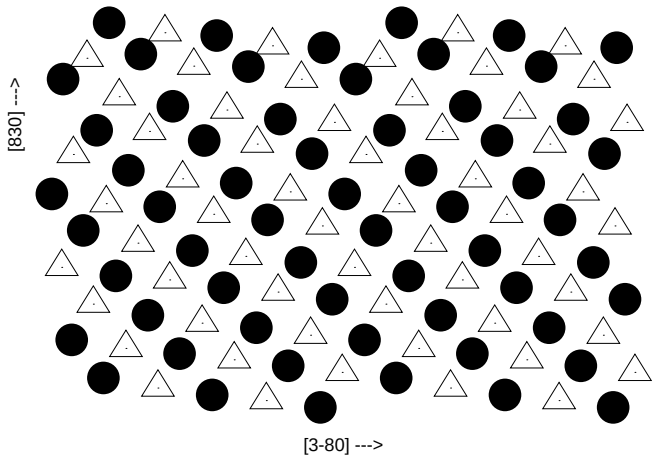

(b) Al-deficient

Figure 4.4: Structural units in the (830) surface in the ordered compounds showing two possible surface terminations.

of the surface structure is stoichiometric. The energy of this unit is in turn dependent on the stoichiometry of the bulk which contains the surface.

A comparison of the calculated versus simulated surface energies was done, and again very good agreement was observed. Figs. 4.5 and 4.6 show this comparison for the stoichiometric and average surfaces in FeAl and NiAl respectively. For surfaces where different terminations are possible, depending on the plane of cut, the average energy of the two terminations, within a given bulk, was used.

The difference in energy between two possible terminations in a given bulk was investigated, Fig. 4.7. A decrease in the difference in energy between two terminations was observed with increasingly higher index surfaces, with the biggest difference being attained by the (100) surface. This was attributed to the decrease in the relative contribution to the overall surface energy of the unmatched A-type unit, (100). For all off-stoichiometric surfaces there is only one unmatched A-type unit and thus the fraction of the total area occupied by this unit decreases for higher index surfaces, ie. as the area of the repeat unit of the surface increases. This means that the presence of the different terminations is not so important for high index surfaces.

4.5.2 Results for γ TiAl

The model was next tested for fcc-based ordered compounds, using γ TiAl as an example. As with the B2 ordered, it is important to note that one of the structural units has two possible terminations. Unlike the bcc ordered structures studied, the structural unit A $\left(\text{at } \theta = 0^0\,(100)\right)$, has one stoichiometric termination in the $L1_0$ case and the structural unit B $\left(\text{ at } \theta = 45^0\,(110)\right)$ now has two possible terminations, B_1 for the 100% Ti (Fig. 4.8(b)), or B_2 (Fig. 4.8(c)) for the 100%Al termination. For the off-stoichiometric surfaces the deviation from stoichiometry is accomplished by an extra B-type unit of the same excess as the surface. Using the surface at $\theta = 30.97^0\,(350)$ as an example, it again has a different combination of units depending on whether it is Al-deficient $(2A + 2B_1 + B_2)$ or Al-rich $((2A + B_1 + 2B_2)$ as shown in Fig. 4.9.

For TiAl, the energy for off-stoichiometric surfaces is dependent on the B-type unit since the number of B-type units is odd and one of the B-type units is unmatched. The energy of this unit

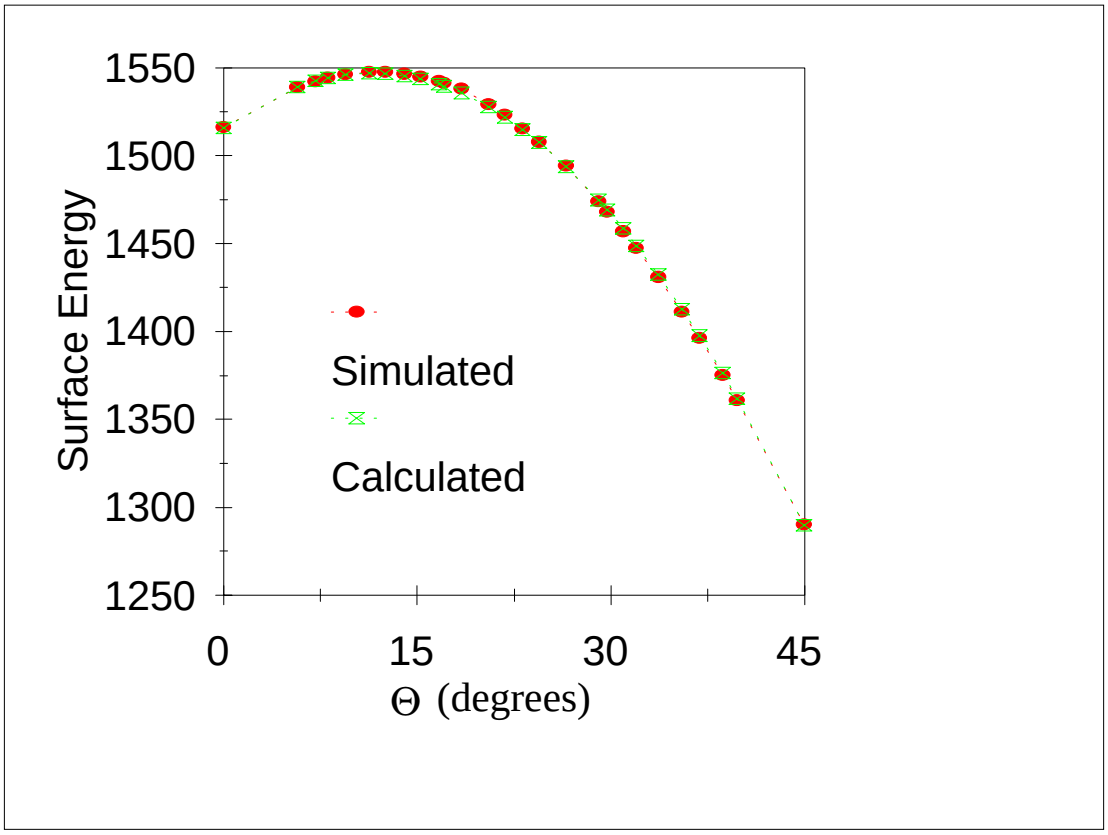

Figure 4.5: Simulated and Calculated Stoichiometric and average surface energies (in mJ/m^2) of FeAl as a function of orientation angle. (The dashed lines serve only as guides for the eye)

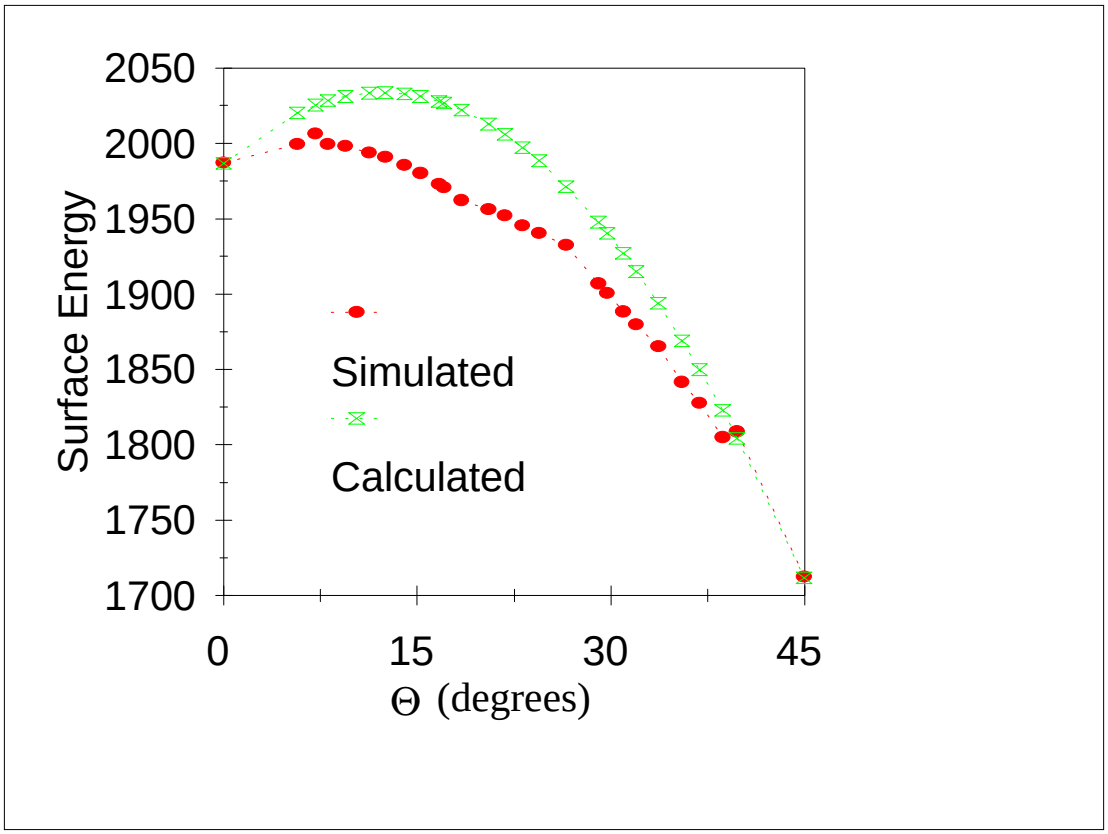

Figure 4.6: Simulated and Calculated Stoichiometric and average surface energies (in mJ/m^2) NiAl as a function of orientation angle. (The dashed lines serve only as guides for the eye)

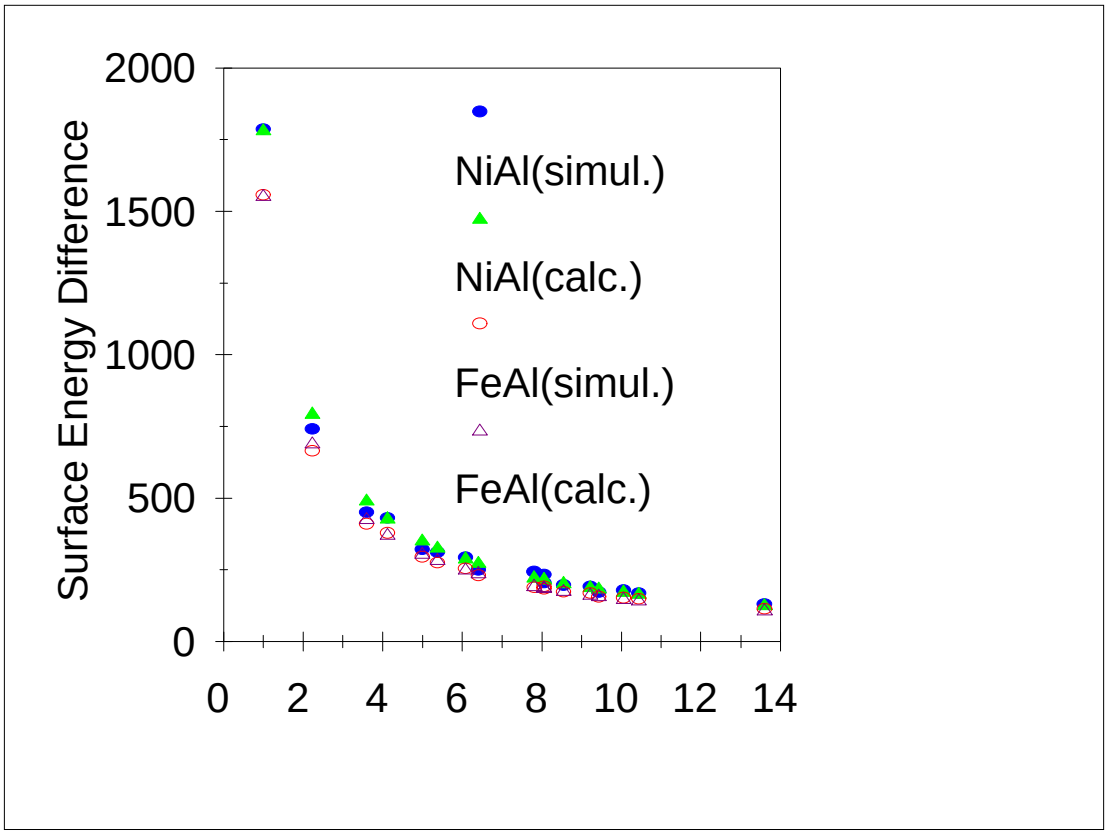

Figure 4.7: The energy difference (in mJ/m^2) (simulated and calculated) between two different terminations in FeAl and NiAl as a function of $\sqrt{h^2+k^2}$

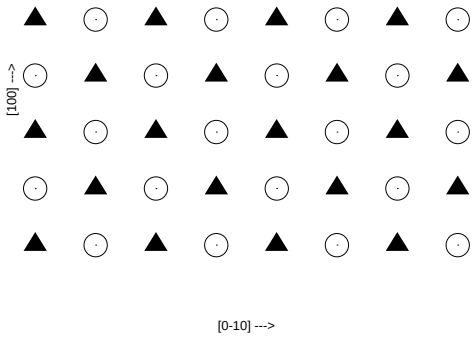

(a) unit A

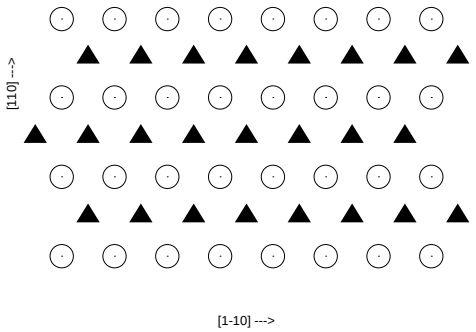

(b) unit B_1

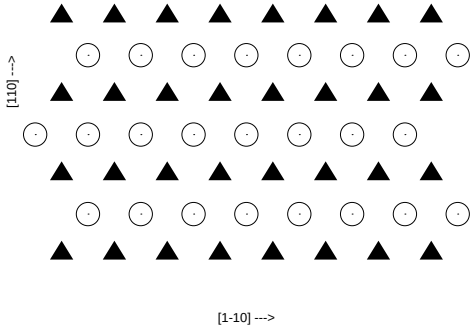

(c) unit B_2

Figure 4.8: Structural units for TiAl

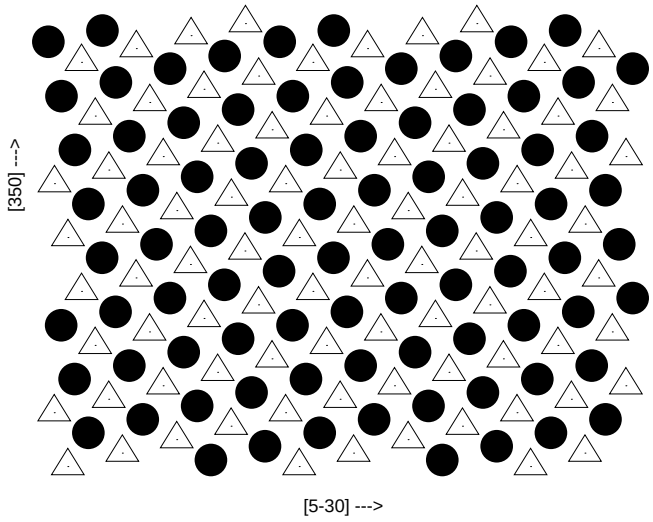

(a) Al-rich

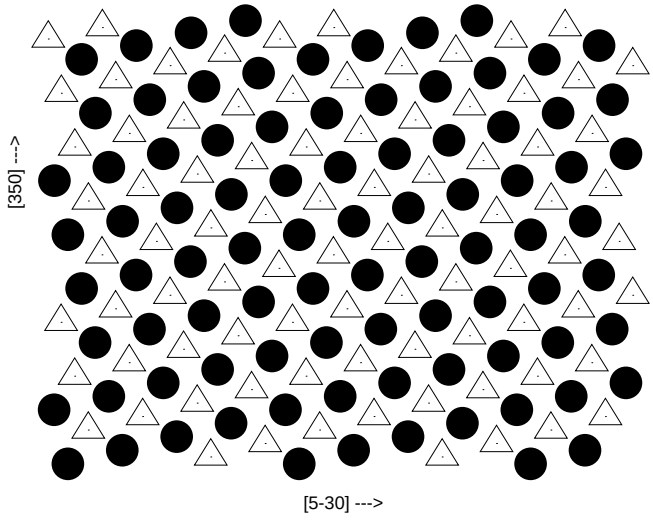

(b) Al-deficient

Figure 4.9: Structural units in the (350) surface in TiAl showing two possible surface terminations.

is dependent on the stoichiometry of the bulk which contains the surface. However, the number of B-type units is even for stoichiometric surfaces and each B_1 unit is matched with a B_2 unit. This gives rise to the energy of the surface being independent of the bulk stoichiometry which contains it, since the A unit is stoichiometric and the energies of the two types of B-type units average out to give a stoichiometric energy. The surface energies and structures calculated based on the structural unit model were compared to those derived from the simulations. Figs. 4.10 shows this comparison for the stoichiometric and average surfaces in TiAl. The calculated results showed very good agreement to the simulations.

4.6 Discussion

Atomistic simulations of surfaces containing the $\langle 001 \rangle$ axis were performed for both pure metals, Fe and Al and for ordered compounds, NiAl, FeAl and TiAl. A structural unit model can easily be developed to estimate the energies and structural features of higher index surfaces, using some low index surfaces as a basis. The structural unit model successfully predicts the fraction of the different units that comprise the surface and show very good agreement with the simulated structures and energies. The values of surface energy calculated on the basis of this model are consistent with those derived from simulations. The energy differences of the calculated versus simulated values were within 3% for both pure Fe and Al and for the ordered compounds NiAl, FeAl and TiAl. It was also shown that the surface energy difference within a given bulk decreases as one moves from low to high index surfaces in the absence of reconstruction. This suggests that the effect of different surface terminations is not as important for high index surfaces as it is for the low index surfaces.

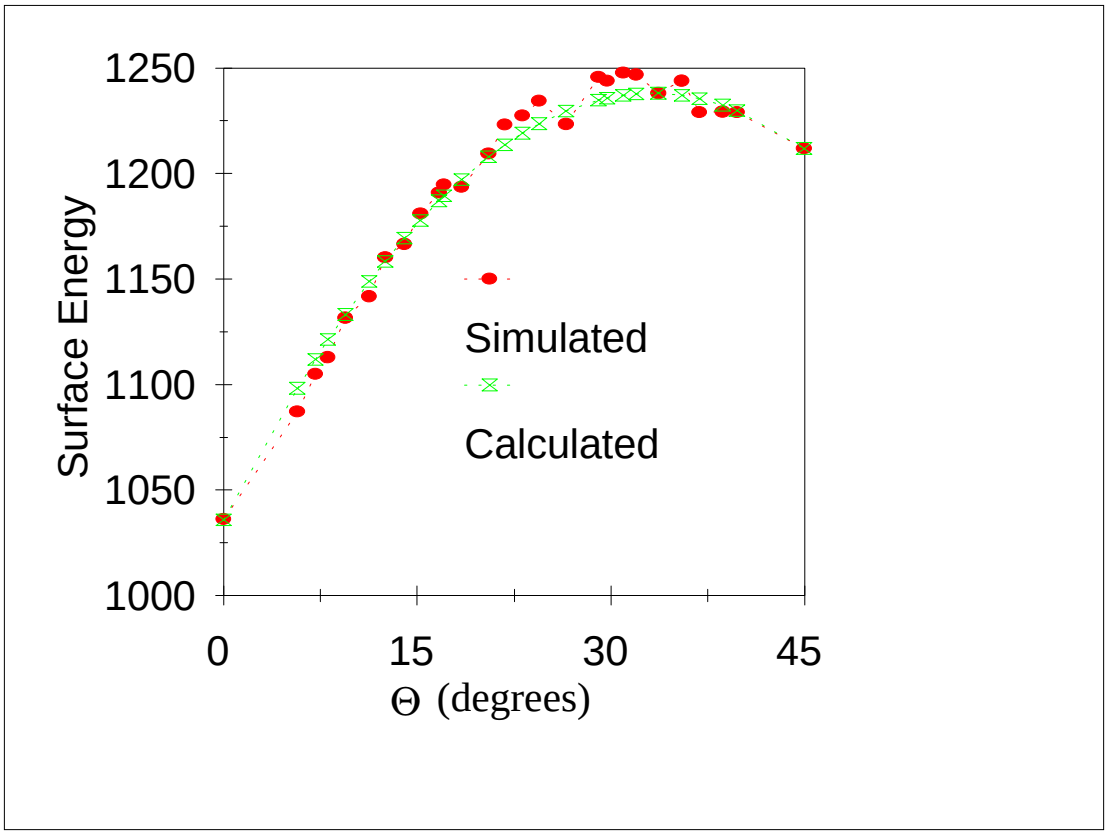

Figure 4.10: Simulated and Calculated Stoichiometric and average surface energies (in mJ/m^2) of TiAl as a function of orientation angle. (The dashed lines serve only as guides for the eye)

Chapter 5

GRAIN BOUNDARIES IN B2 COMPOUNDS

5.1 Simulation Procedure

The first step in the simulation of a planar defect is the generation of the perfect crystal structure from a specific initial configurations. The crystal structure is generated based on information of the Bravais lattice and repeating this along the cartesian coordinates. The lengths of the orthogonal vectors are defined as the lattice parameters of the respective unit cells. A limiting block is then defined within which all atoms are located. The atoms within this block are allowed to move freely according to interactions defined by the potentials. An outer block, embedding the first is then created with atoms that are only influenced by the long range elastic fields of the defect.

The initial structures of $\Sigma = 5(310)$ and $\Sigma = 5(210)$ grain boundaries were generated by reflecting a semi-infinite perfect crystal against the $(1\bar{3}0)$ and $(1\bar{2}0)$ planes. Additional variants of the boundary structures were obtained by changing the sublattice positions occupied by Al and Ni atoms in the upper and lower crystals, eliminating an atomic layer in the boundary region, or displacing one crystal with respect to the other in the z-direction (normal to the boundary plane). The above procedures are essentially equivalent to rigid-body translations applied to one of the crystals and lead to different types of matching between the two crystals without changing their misorientation or the position of the boundary plane. Importantly, the structural variants thus obtained differ not only in the atomic distribution but also in the local chemical composition in the grain boundary region.

The boundary structures obtained by the above geometrical constructions were used as starting configurations for the subsequent structural relaxations. The structural relaxation procedure was the standard "molecular statics" technique using the conjugate gradient method for the energy

minimization. Periodic boundary conditions were imposed in the directions parallel to the boundary plane, while fixed boundary conditions were applied normal to the boundary plane. The total energy was also minimized with respect to possible rigid body displacements of one crystal relative to the other.

5.2 Boundary Energy Calculations

The grain boundary energy, γ_{gb}, can be considered as the difference in energy between a crystal with the defect, E_d, and the energy of a perfect crystal, E_p:

$$\gamma_{gb} = \frac{1}{A}(E_d - E_p), \tag{5.1}$$

where A is the area of the grain boundary. In our computer simulations, the energies E_d and E_p are calculated for simulation blocks consisting of equal number of atoms of each species. This grain boundary energy, γ_{gb}, can also be represented as:

$$\gamma_{gb} = \frac{1}{A}\left[E_d - (N_M\mu_M + N_{Al}\mu_{Al})\right] \tag{5.2}$$

where M represents the transition metal (Co, Ni or Fe), N_x is the number of atoms of M or Al in the crystal, and μ_x is the chemical potential of these elements.

5.2.1 Off-stoichiometric Boundaries

In the past, energies of boundaries that were not stoichiometric have, in general, been computed by assuming an equal division of the energy of the mixed bond between the two atoms. Ackland pointed out that the chemical potential thus described is unique as long as the embedding function is uniquely defined [60]. Requiring that the embedding function be fit to Rose's equation of state, [51], ensure's its unique definition. The chemical potentials of the two species of atoms, μ_{Al} and μ_M, were also calculated using this assumption. The chemical potentials are related to E_{coh} by:

$$E_{coh} = \mu_M + \mu_{Al} \tag{5.3}$$

In the present work we use the thermodynamically consistent method of calculating the chemical potentials in atomistic simulations proposed by Hagen and Finnis [61]. This method does not affect stoichiometric simulation blocks with locally stoichiometric boundaries, since only the sum of the chemical potentials,γ_{coh}, is required. For off-stoichiometric systems, however, the difference between the chemical potentials is required:

$$\Delta\mu = \mu_M - \mu_{Al} \tag{5.4}$$

Hagen and Finnis assume that in such cases the chemical potentials are functions of the formation energies of the predominating structural point defects that accommodate the departure from stoichiometry. Thus, for an off-stoichiometric alloy, the reference state contains the point defects; antisites dominate on the Al-deficient side and vacancies are predominant on the Al-rich side. It follows from this assumption that the energy of the point defect that accommodates the deviation from stoichiometry is zero. The chemical potentials thus derived are composition-dependent and show a discontinuity at the 50/50 composition.

A result of using this technique is the energy dependence of the various defects on the stoichiometry of the total block which contains the boundary. Off-stoichiometric boundary and free surface energies will greatly depend on the composition of the block that contains them. Table 3.3 gives the chemical potentials and the true formation energies of the point defects. The surface energies are shown in Table 5.1. The energies of grain boundaries with different local composition (boundary stoichiometry) calculated in systems of different stoichiometries (block stoichiometry) are shown in Figures 5.19 to 5.22.

5.2.2 Boundary Cohesive Energy

Of interest in the compounds being studied is the propensity for intergranular fracture which could be attributed to low cohesive energies of the grain boundaries. This cohesive energy represents the energy required to cleave the boundary. Fracture of the boundary creates two free surfaces (S1 and S2) which may or may not have the same termination. The grain boundary cohesive energy,

γ_{coh}, can be represented as the sum of the surface energy of the two surfaces created minus the energy of the boundary which is cleaved.

$$\gamma_{coh} = \gamma_{S1} + \gamma_{S2} - \gamma_{gb}. \tag{5.5}$$

The grain boundary energy and the cohesive energy of the boundary are thus inversely related. Thus the higher the boundary energy, the lower the boundary cohesive energy, and the easier it is to fracture the crystal intergranularly.

The technique for the calculation of the chemical potentials described in chapter 3 does not affect, however, either the energies of stoichiometric boundaries or cohesive energies of any boundaries. The cohesive energies are unaffected because they are a result of creating two free surfaces from a grain boundary without changing the block composition which contains the defect. The cohesive energies obtained by using this method are presented in Figures 5.23

5.3 Grain Boundary γ Surfaces

Grain boundary γ-surfaces were computed for CoAl, NiAl and FeAl along the {210} and {310} planes. The two blocks of atoms defined on both sides of the boundary plane were rigidly displaced according to fault vectors with components in the X and Z directions (within the boundary plane). The faults' simulation method is similar to that originally proposed by Vitek [72]. This gives rise to a multiplicity of possible grain boundary structures and accompanying energies that can be created within the CSL theory by rigid body translations of one grain with respect to the other. The energetics of this multiplicity can be studied by plotting the energy of the boundary against the rigid body displacements parallel to the grain boundary plane. This is termed the grain boundary γ-surface. The energies for these grain boundary γ-surface configurations were computed after relaxation in only the Y direction (perpendicular to the boundary plane).

This method of grain boundary representation gives a good visual method for determination of local minima and directions of lowest energy. The structures that coincide with the minima are the stable structures. The γ-surfaces are visualized as contour plots of the energy as a function of

the rigid body displacements. These γ-surfaces were created by the computation of 300 to 2000 boundary energies in order to scan the entire plane under study. From the scan of the planes, the positions of the minima were identified and the corresponding structures and their resultant energies were computed, allowing for complete relaxation parallel and perpendicular to the boundary plane. The contour plots of the simulated {210} and {310} grain boundary γ-surfaces in FeAl, NiAl and CoAl are presented in Figures 5.1 to 5.6. Darker shades correspond to lower energies.

5.4 Results

5.4.1 {210} Grain Boundary γ Surfaces

The stoichiometric {210} grain boundary γ-surfaces were computed for FeAl, NiAl, and CoAl such that the rigid body displacements parallel to the grain boundary plane were along $[1\bar{2}0]$ and [001], Figures 5.1, 5.2 and 5.3 respectively. The {210} grain boundary γ-surfaces showed very similar characteristics with a general increase in grain boundary energy from FeAl to CoAl for the intermetallics. Minima were observed at the complete grain boundary period, perpendicular to the tilt axis along $[1\bar{2}0]$, with and without a shift by 1/2a boundary period in [001]. The structures, corresponding to these minima, are shown in Figures 5.12(a) and 5.12(b) respectively. The grain boundary period is given by $a\sqrt{h^2+k^2+l^2}$ of the respective directions parallel to the grain boundary plane.

The off-stoichiometric {210} grain boundary γ-surfaces, were also computed for an excess of one atom per boundary plane. It is important to note that, for these compounds, the {210} planes alternate between 100% Al and 100% Fe, Ni, or Co. The computation of the off-stoichiometric γ-surfaces was accomplished by removal of one layer at the boundary plane and then applying rigid body displacements along the boundary plane, and again only letting the boundaries relax in the direction of the boundary normal. All possible structures are accounted for by the rigid body displacements. The γ-surfaces, were again very similar. An example of the topology of these γ-surfaces is given, for both Al-deficient and Al-rich boundaries, in CoAl and the energies are given for an Al-deficient bulk. The results are shown in Figures 5.9 and 5.10 respectively.

5.4.2 {310} Grain Boundary γ Surfaces

Stoichiometric {310} grain boundary γ-surfaces were computed for CoAl, NiAl and FeAl such that the rigid body displacements parallel to the grain boundary plane were along $[1\overline{3}0]$ and [001]. The three {310} grain boundary γ-surfaces, again, showed very similar characteristics with a general increase in grain boundary energy from FeAl to CoAl. The γ-surfaces exhibit two fold symmetry in the boundary plane. Two metastable minima were located at two symmetric positions, at the complete and at 1/2 the grain boundary period along $[1\overline{3}0]$, with a shift along [001] by 1/2a. Minima, with slightly higher energies, were also located at two symmetric positions without a shift in [001]. For a more detailed look at the γ-surface topology, a profile (cut) of the surface was made at 1/2 of the period along [001] (Figure 5.7) and at 1/2 of the period along $[1\overline{3}0]$ (Figure 5.8). The example given is for the computed stoichiometric {310} grain boundary γ-surface in NiAl. From Figure 5.7, the structures at the minima at 1/2 the period along [001] were found to have the same energy. Details of the structures are discussed in section 5.4.3. The structures corresponding to the minima at 1/2 the period along $[1\overline{3}0]$ from Figure 5.8, include the lowest energy structure mentioned above and the structure at the higher minima. The structures are shown in Figures 5.16(a) and 5.16(b).

Since each {310} plane contains equal number of atoms of each type; off-stoichiometry at the boundary is attained by atom substitution, and subsequent rigid body displacements, along the directions within the boundary plane, would not necessarily give rise to all possible structures. Off-stoichiometric γ-surfaces were thus not computed for this boundary plane.

It is important to note that from the γ-surfaces that the minima, for both $\Sigma = 5$ boundary planes considered, occur at either half or at the complete periodicity of the boundary and not at any arbitrary position. It must also be noted that, for stoichiometric boundaries, the global minimum occurs at 1/2 a shift along the tilt axis.

5.4.3 Relaxed Structures

From the computed γ-surfaces, the positions of the minima were identified and the corresponding structures and their resultant energies were computed, allowing for complete relaxation parallel

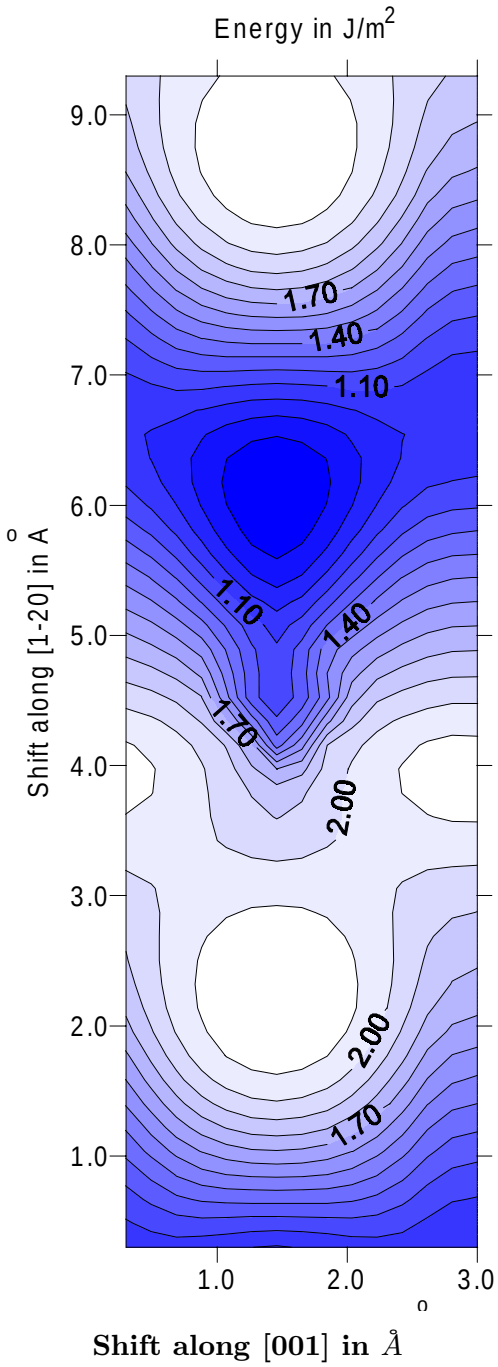

Figure 5.1: Computed stoichiometric {210} grain boundary γ-surface in FeAl. (Energies are in J/m^2)

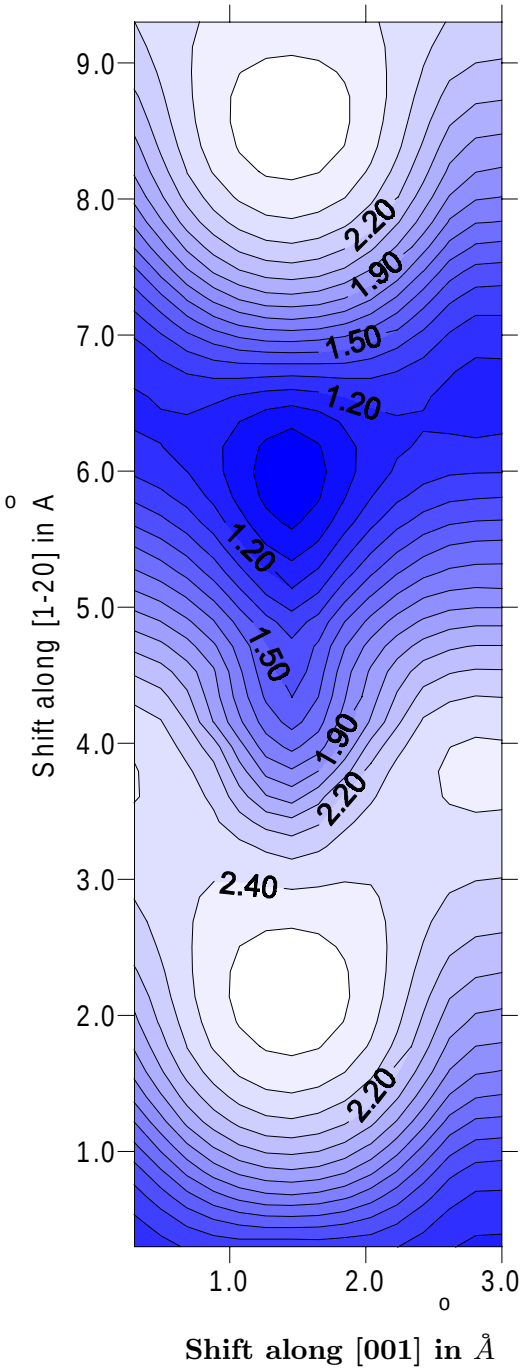

Figure 5.2: Computed stoichiometric {210} grain boundary γ-surface in NiAl. (Energies are in J/m^2)

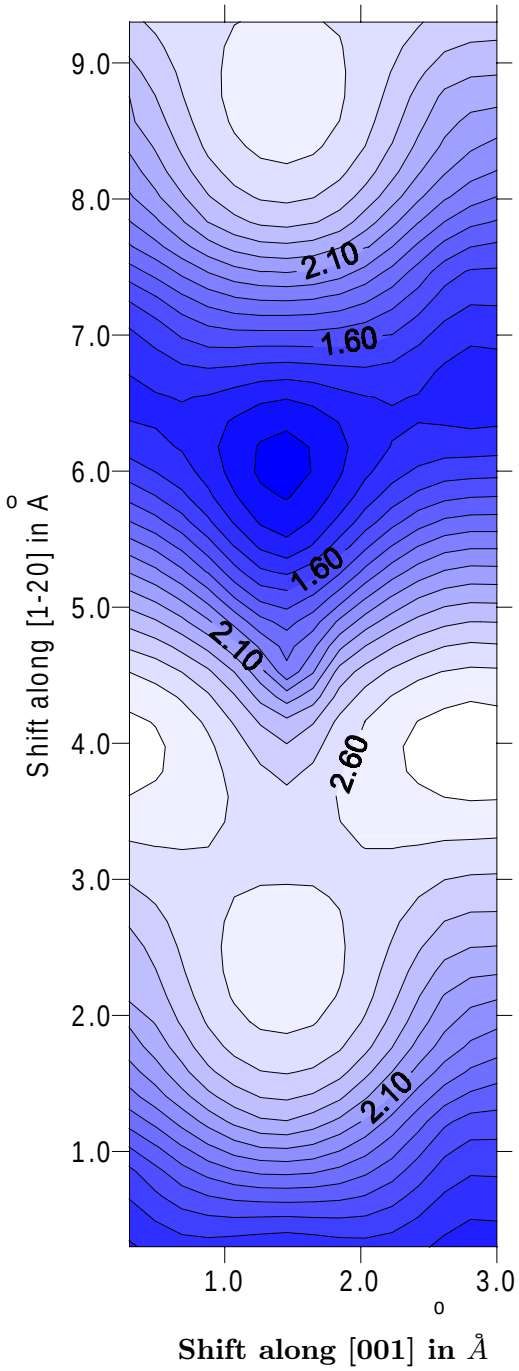

Figure 5.3: Computed stoichiometric {210} grain boundary γ-surface in CoAl. (Energies are in J/m^2)

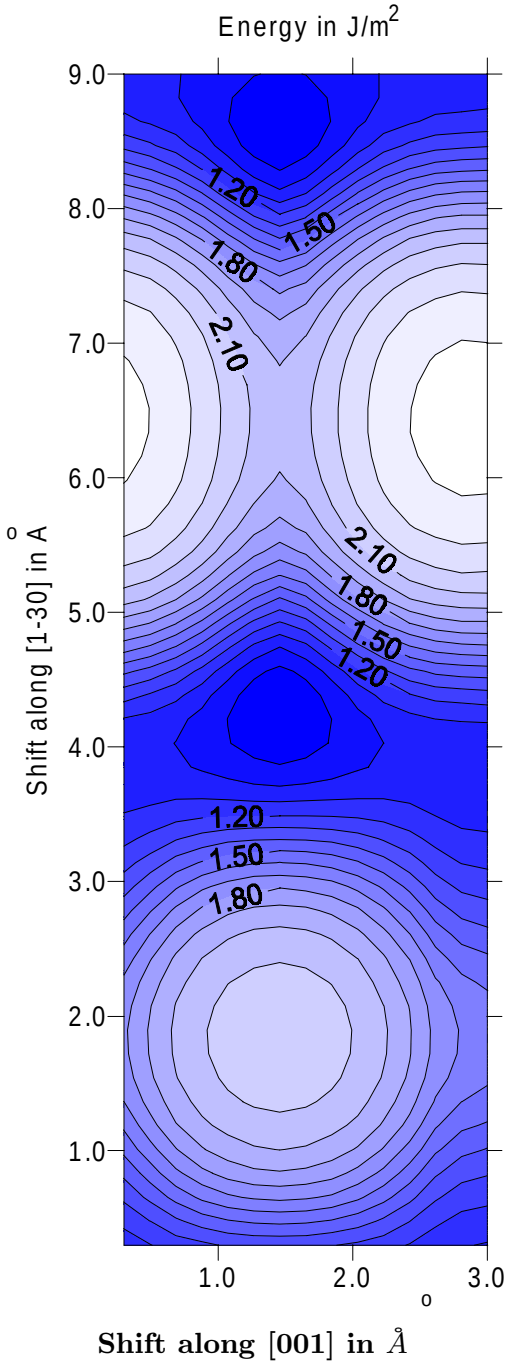

Figure 5.4: Computed stoichiometric {310} grain boundary γ-surface in FeAl. (Energies are in J/m^2)

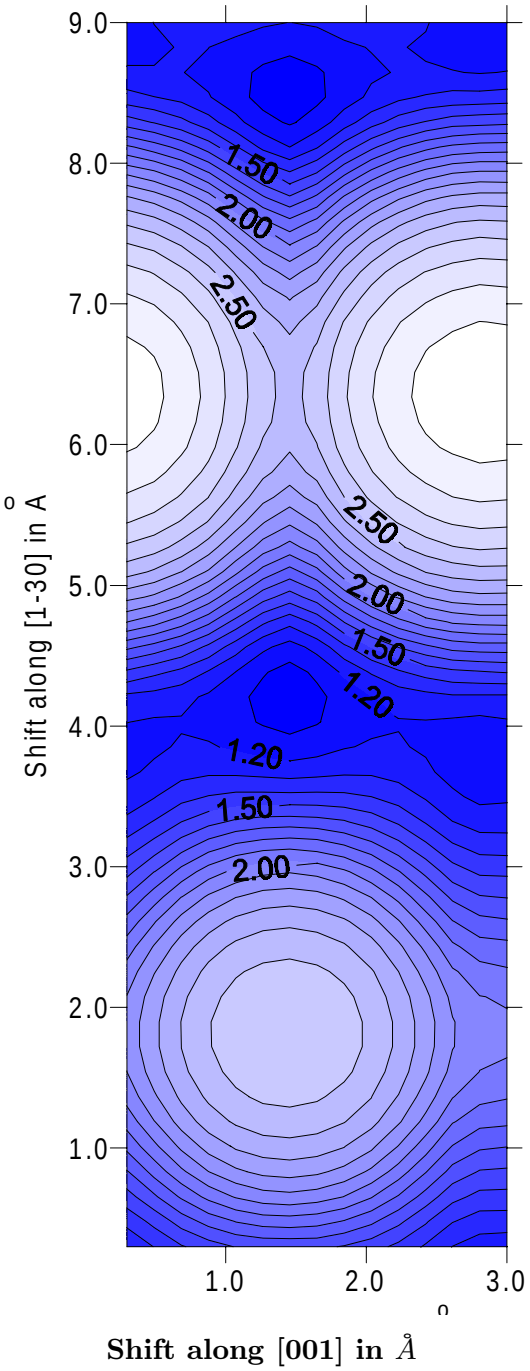

Figure 5.5: Computed stoichiometric {310} grain boundary γ-surface in NiAl. (Energies are in J/m^2)

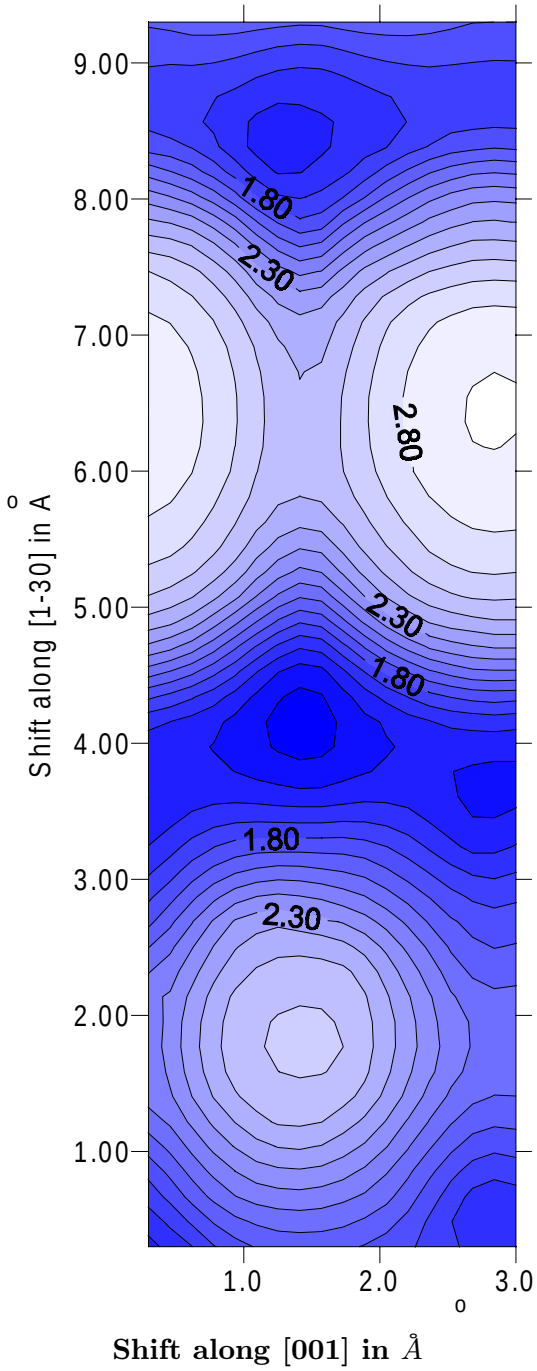

Figure 5.6: Computed stoichiometric {310} grain boundary γ-surface in CoAl. (Energies are in J/m^2)

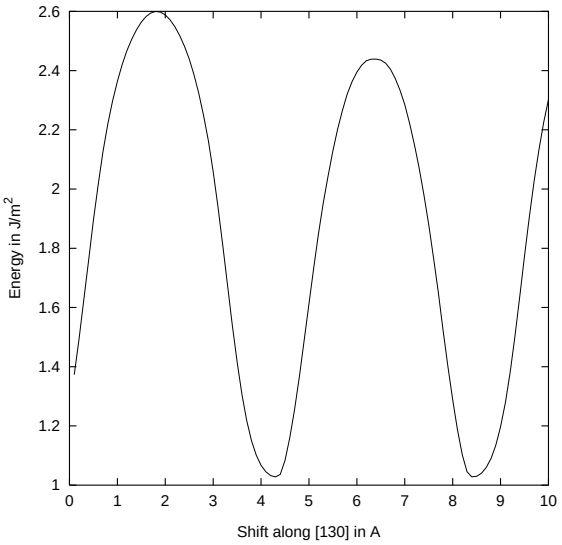

Figure 5.7: Profile of the stoichiometric {310} grain boundary γ-surface at 1/2 the period along [001]

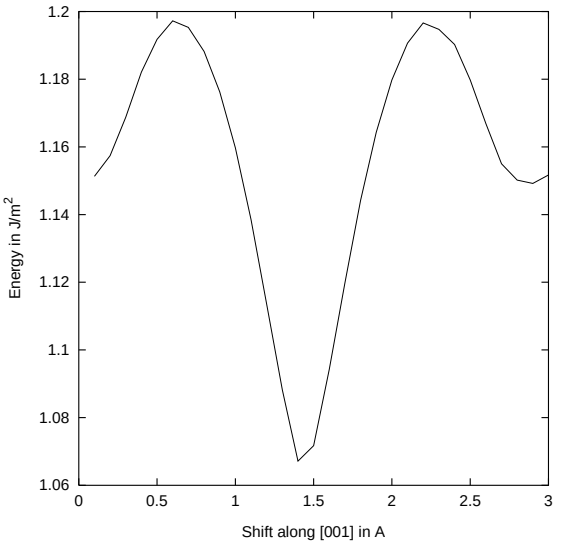

Figure 5.8: Profile of the stoichiometric {310} grain boundary γ-surface at 1/2 the period along [$1\bar{3}0$]

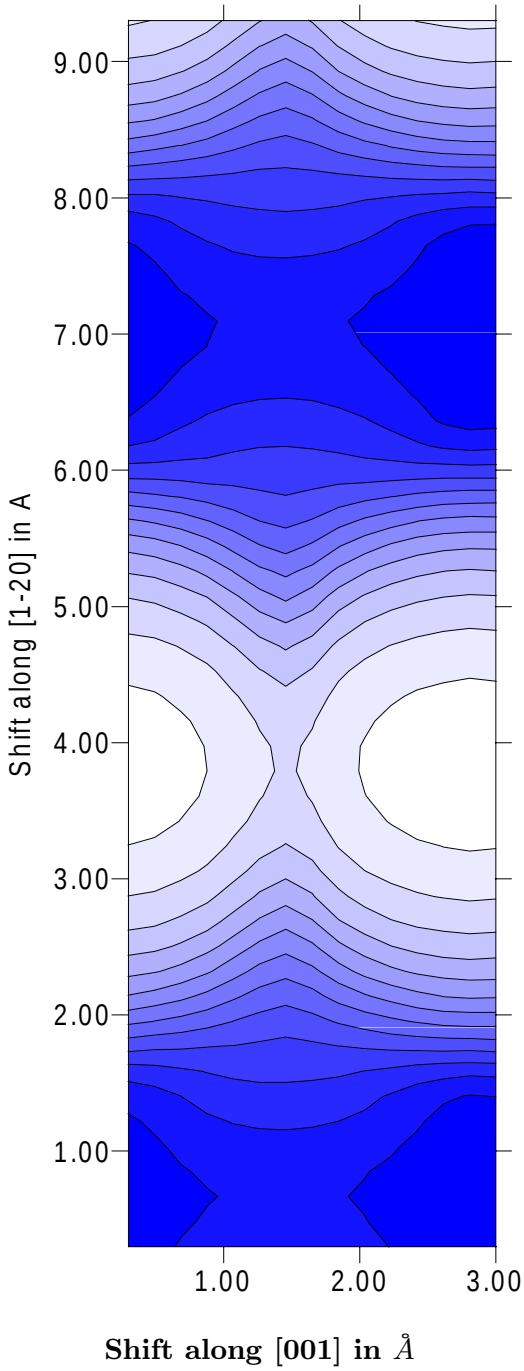

Figure 5.9: Example of the topology of the grain boundary γ-surface for the Al-deficient boundaries in {210} B2 compounds.

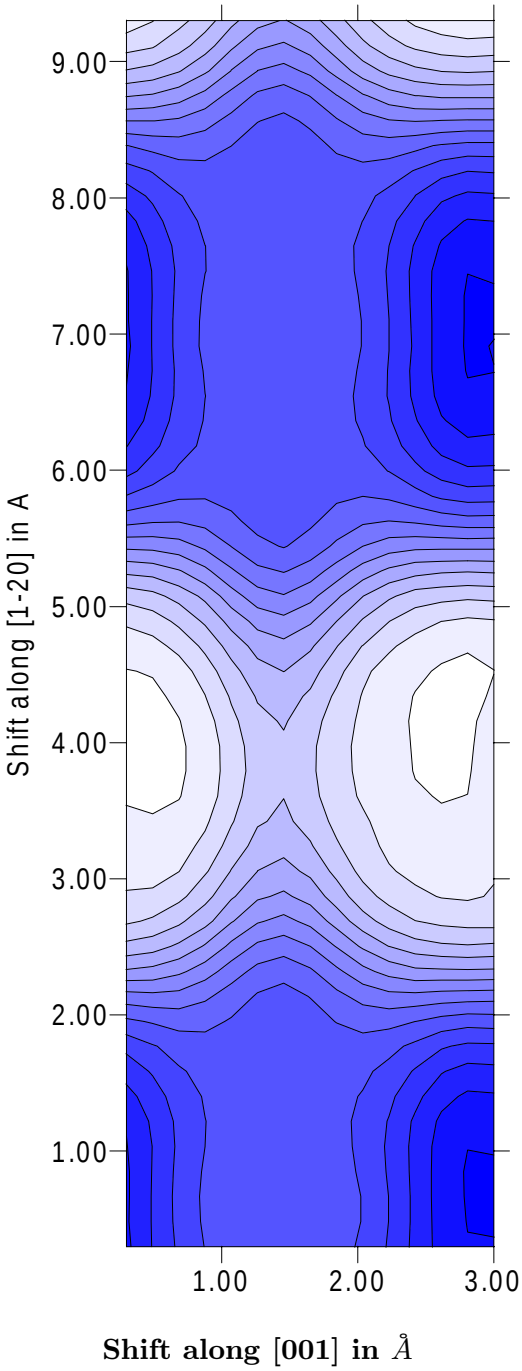

Figure 5.10: Example of the topology of the grain boundary γ-surface for the Al-rich boundaries in {210} B2 compounds.

and perpendicular to the boundary plane. Figures 5.11 to 5.18 show the relaxed structures of the $\Sigma = 5[001]$ symmetric tilt grain boundary in these B2 compounds for both stoichiometric and off-stoichiometric boundaries. The off-stoichiometric boundaries, Al-rich or Al-deficient, are computed for cases where there is either 1 or 2 atoms in excess per boundary period. The circles depict Al and the triangles the transition metal atoms. Color variations of the symbols represent different (002) planes. The polyhedra delineate grain boundary repeat units. The common topological features, exhibited by the three compounds studied, from the computed γ-surfaces corresponded to common structural features of the relaxed structures. For this reason only one structure is shown for the three compounds, because of the structural feature similarity.

Stoichiometric Boundaries

It is important to note that the fully relaxed lowest energy stoichiometric structure for a {210} boundary in the B2 structures, Figure 5.12(a) differs from that expected from geometric considerations alone, Figure 5.12(b), which corresponds to the minima with the higher energy. The resultant lowest energy relaxed grain boundary structure has a shift of 1/2a along [001] and it reduces the 'open structure' inherent to the geometrically expected structure. The energies for the lowest energy structures are 617, 772 and 1082 mJ/m^2 for FeAl, NiAl and CoAl respectively. The higher minima yields structures with energies that are at least 200 m J/m^2 higher; 884, 976, 1228 mJ/m^2 for FeAl, NiAl and CoAl respectively.

In the case of {310} stoichiometric boundaries, it can be seen from the profile of the γ-surface made at 1/2 the period along [001] (Figure 5.7) were the lowest minima were located that the two structures have the exactly the same energy. On full relaxation, the structures at these two positions still had the same energy. The displacements required to produce these structures resulted in equivalent structures due to the symmetry of the crystal. The two structures are related by a symmetry operation of the crystal and are thus energetically degenerate and therefore only one structure is shown. This structure (Figure 5.16(a)) was found to, not only, have displacements in the boundary plane, but also have a non-zero component parallel to the tilt axis. This component was equivalent to 1/2 a shift along the [001] direction. The energies correspond to 714, 930, and 1232

mJ/m^2 for FeAl, NiAl and CoAl respectively. The higher minima yields structures (Figure 5.16(b)) with energies of 908, 989 and 1330 mJ/m^2 for FeAl, NiAl and CoAl respectively.

Off-stoichiometric Boundaries

The off-stoichiometric boundaries computed have either 1 or 2 atoms in excess per boundary period. The procedure used to simulate these boundaries differed for the two boundary systems due to the difference in composition of successive crystallographic planes. The {210} planes consist of alternating planes of 100% Fe, Ni or Co and 100% Al. The {310} planes are composed of equal numbers of the transition metal and Al. The proper thermodynamically consistent method of calculating the defect energy is used for these boundaries. As discussed earlier in section 5.2.1, off-stoichiometric boundary energies depend on the composition of the block that contains them. Figures 5.19 to 5.22 show the energies of these grain boundary structures calculated in systems of different stoichiometries (block stoichiometry). A result of using this technique is the energy dependence of the various defects on the stoichiometry of the total block which contains the boundary.

Off-stoichiometry in the {210} planes was achieved by removal of one layer of atoms to get either Al-deficient (Figure 5.11) or Al-rich (Figure 5.13) boundaries. This was done for an excess of one atom per boundary plane. One of the structures resultant from the full relaxation of displacements indicated from the γ-surfaces minima, had a non-zero component parallel to the tilt axis and the other did not. This was similar to the results for the stoichiometric boundaries. In the {310} planes, off-stoichiometry was achieved by two methods, namely; atom removal around the boundary plane to get boundaries with one atom in excess or atom substitution around the boundary plane to get boundaries with two atoms in excess. The lowest energy stoichiometric boundaries were used as the initial configurations. Atoms were systematically removed or substituted at different positions of the boundary unit. Rigid body displacements were applied along the [130] direction after the atom removal or substitution. The fault vectors were, again, based on multiples of the DSC vectors. A sampling of the low energy structures so derived is shown in Figures 5.14, 5.15, 5.17 and 5.18.

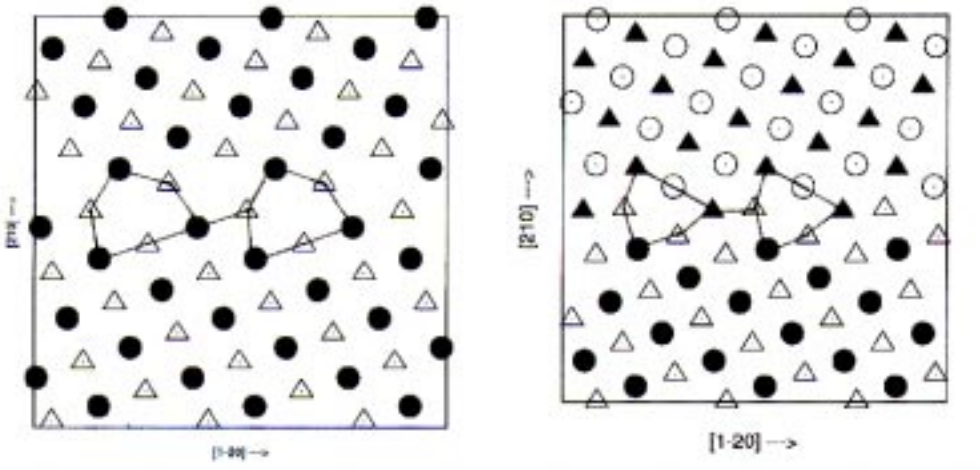

(a) (b)

Figure 5.11: Al-Deficient structures of the $\Sigma = 5(210)[001]$ symmetric tilt grain boundary in B2 intermetallic compounds.

5.4.4 Multiplicity of Boundary Structures

The basic structures obtained were similar for the three B2 compounds analyzed. A sampling of the structure variations of the $\Sigma = 5(210)[001]$ and the $\Sigma = 5(310)[001]$ symmetrical tilt grain boundaries are shown in Figures 5.11 to 5.18. In agreement with previous work on NiAl [47], a variety of structures of the same grain boundary with similar energies is possible in these B2 compounds. From examination of the γ-surfaces it is apparent that the possible variants are not local minima, but rather strained variants of the minima. These variants can result in structural configurations with higher energies. Temperature changes or interactions with dislocations or APB's can cause transformations between the different structures, both minima and strained variants of the minima, and this may influence the mechanical response of the grain boundary region.

5.4.5 Trends

To determine the effects of both boundary stoichiometry and bulk stoichiometry on boundary energetics in these materials, a comparison of boundary energy as a function of grain boundary

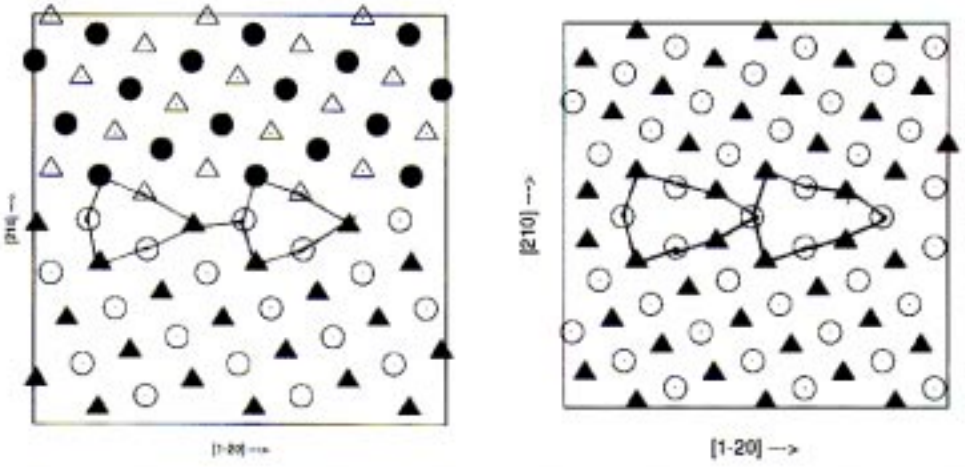

(a) (b)

Figure 5.12: Stoichiometric structures of the $\Sigma = 5(210)[001]$ symmetric tilt grain boundary in B2 intermetallic compounds.

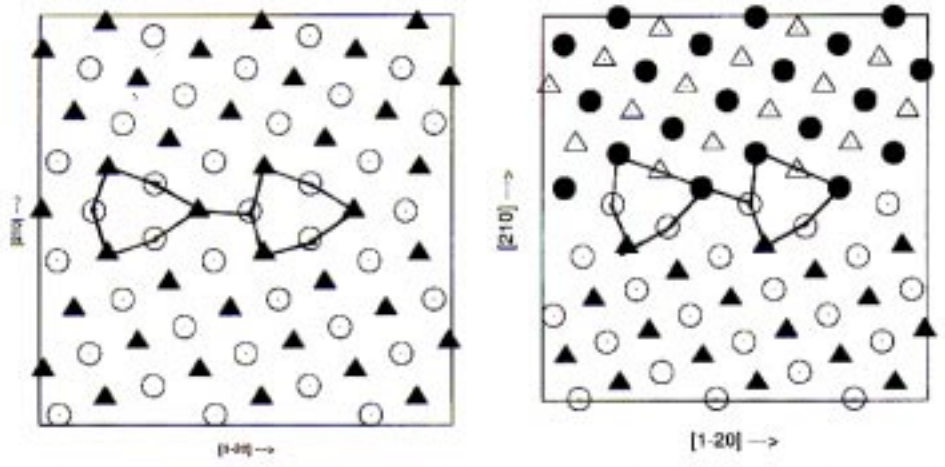

(a) (b)

Figure 5.13: Al-rich structures of the $\Sigma = 5(210)[001]$ symmetric tilt grain boundary in B2 intermetallic compounds.

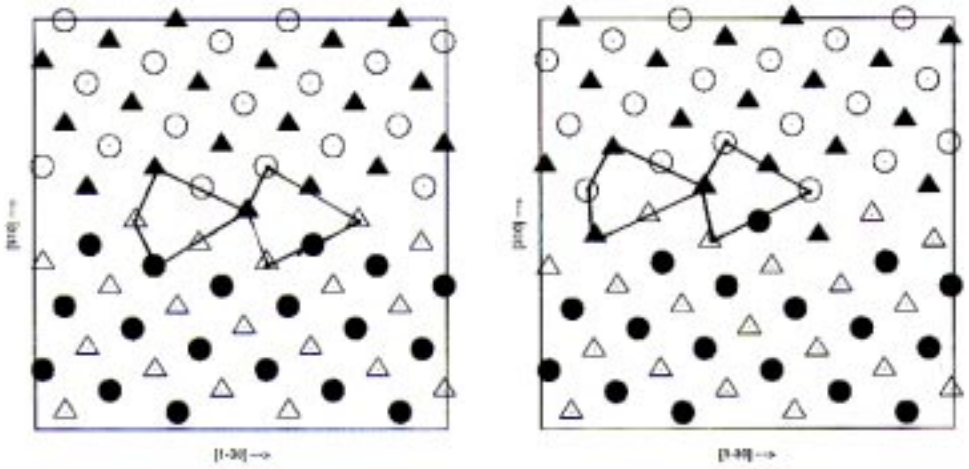

(a) (b)

Figure 5.14: Two Al-Deficient structures of the $\Sigma = 5(310)[001]$ symmetric tilt grain boundary in B2 intermetallic compounds.

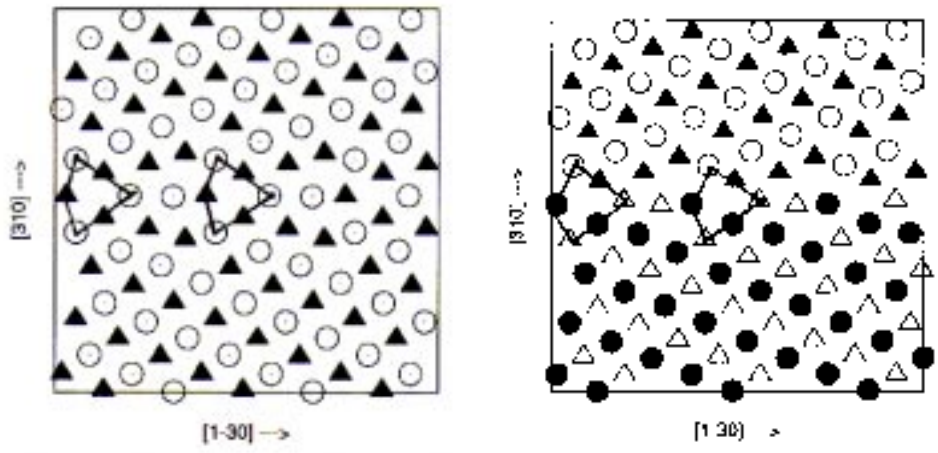

(a) (b)

Figure 5.15: One Al-Deficient structures of the $\Sigma = 5(310)[001]$ symmetric tilt grain boundary in B2 intermetallic compounds.

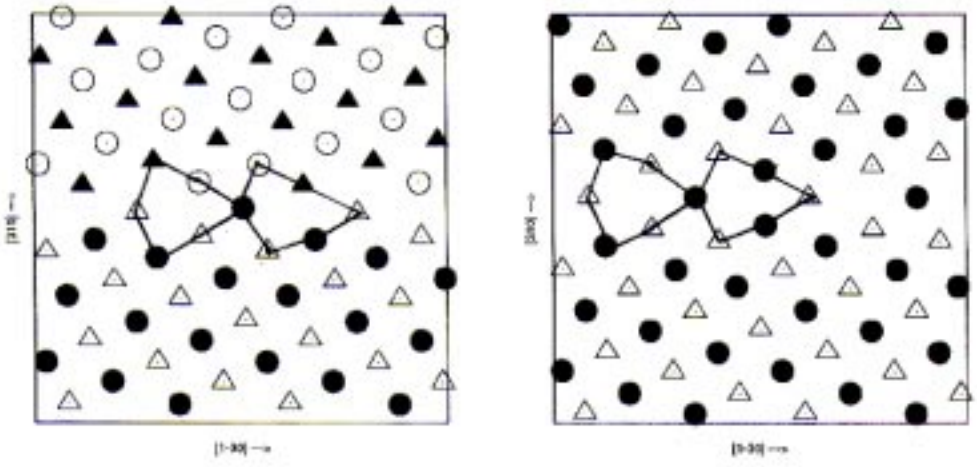

(a) (b)

Figure 5.16: Stoichiometric structures of the $\Sigma = 5(310)[001]$ symmetric tilt grain boundary in B2 intermetallic compounds.

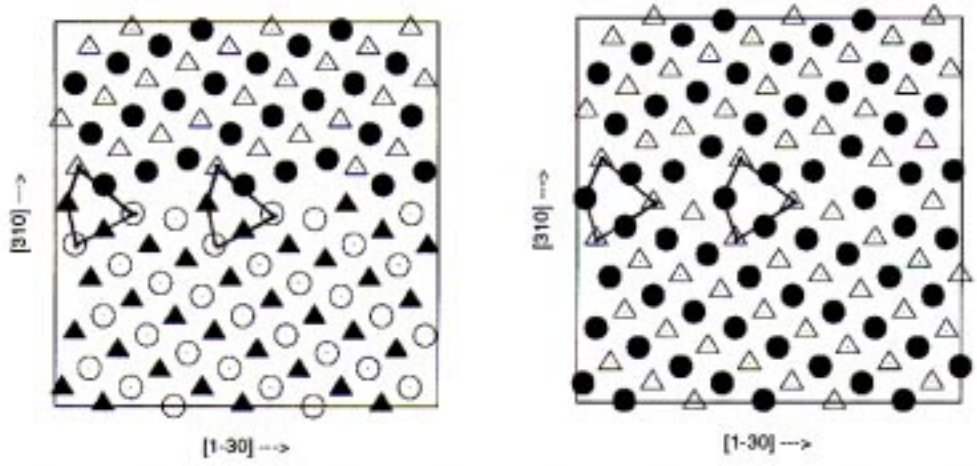

(a) (b)

Figure 5.17: One Al-rich structures of the $\Sigma = 5(310)[001]$ symmetric tilt grain boundary in B2 intermetallic compounds.

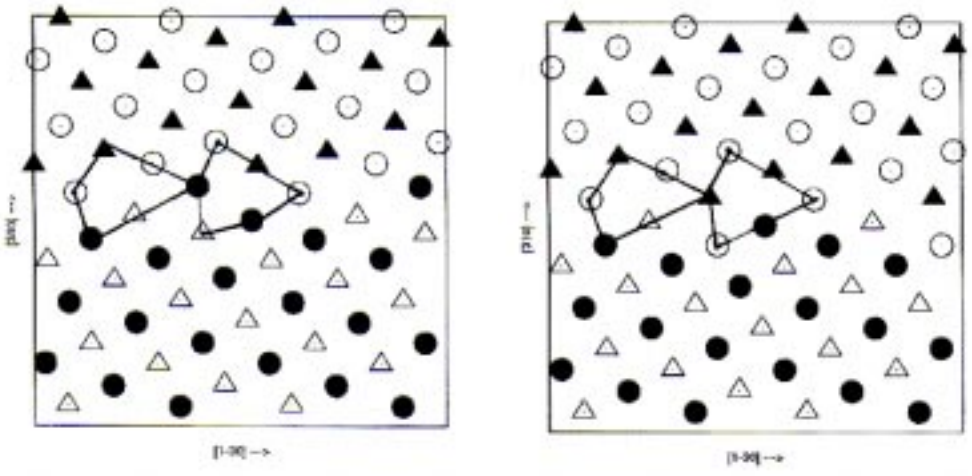

(a) (b)

Figure 5.18: Two Al-rich structures of the $\Sigma = 5(310)[001]$ symmetric tilt grain boundary in B2 intermetallic compounds.

composition was undertaken. This was done using the structures at the minima and some low energy strained variants of these minima structures. Trends between the materials were also obtained for cohesive energies. The trends as a function of grain boundary composition are similar, for both the $\Sigma = 5(310)[001]$ and $\Sigma = 5(210)[001]$ grain boundaries.

The energies of grain boundaries with different local composition (boundary stoichiometry) calculated in systems of different bulk stoichiometries are shown for the $\Sigma = 5(210)[001]$ case in Figures 5.20 and 5.19 and for the $\Sigma = 5(310)[001]$ case in Figures 5.22 and 5.21. From the simulations of grain boundary structures it was found that CoAl tends to have the highest grain boundary energies and FeAl the lowest, except for some structures in which NiAl has lower grain boundary energies than FeAl. The energy ratio of FeAl/CoAl is fairly constant. In agreement with previous work on $L1_2$ Ni_3Al [73], [46] and B2 NiAl [47], it was found in this study that boundary energy is related to the local stoichiometry. It was also ascertained that off-stoichiometric boundary energy is not only related to local composition, but also related to the stoichiometry of the bulk containing the boundary.

In an Al-deficient bulk, increasing the Al content in the grain boundary leads to an increase in the boundary energy. The energies of the Al-rich boundaries (Figures 5.20 and 5.22) are higher than those of stoichiometric boundaries as well as Ni, Fe, and Co-rich boundaries (Figures 5.11 and 5.15). This effect is observed in all three B2 MAl (M=Ni, Fe, or Co) compounds that were studied. The Al-Al interaction tends to be repulsive between nearest neighbors. The effect is more pronounced for the grain boundaries having the $\Sigma = 5(210)[001]$ orientation than for boundaries with the $\Sigma = 5(310)[001]$ orientation.

In an Al-rich bulk, Al-rich boundaries are favored much more than Al-deficient boundaries are favored in an Al-deficient bulk (Figures 5.19 and 5.21) . There is a more pronounced preference for boundaries that increase the Al-Al interactions. It can be inferred from this that in an Al-rich system the excess Al tends to segregate to the boundary, which has a lower packing density than the bulk, to decrease the energy of the system.

Similar trends were observed for the free surface energy in the compounds studied with the highest energies for NiAl and the lowest for FeAl. Table 5.1 shows the surface energies for the various terminations and the average surface energy for the B2 compounds. The (210) surface has the possibility of terminating as either Al-rich or Al-deficient, whereas the (310) surface plane has a unique, equiatomic termination. The (210) plane showed the higher grain boundary cohesive energies for all the structures studied. Figure 5.23 shows the trends observed in grain boundary cohesive energies in (310) boundaries. The cohesive energies are unaffected by the stoichiometry of the block which contains the boundary since they are a result of creating two free surfaces from a grain boundary without changing the block composition which contains the defect. This was checked by computing the cohesive energies for different boundary stoichiometries in the different bulk and ensuring that the correct surface composition within the given bulk was used. The results for cohesive energies are not quite what one would intuitively expect from the trends in grain boundary energy. NiAl exhibited the highest cohesive energy and FeAl the lowest for the grain boundaries studied. The boundary cohesive energy decreases with increasing Al content. This behavior is consistent with boundary composition trends in an Al-rich system.

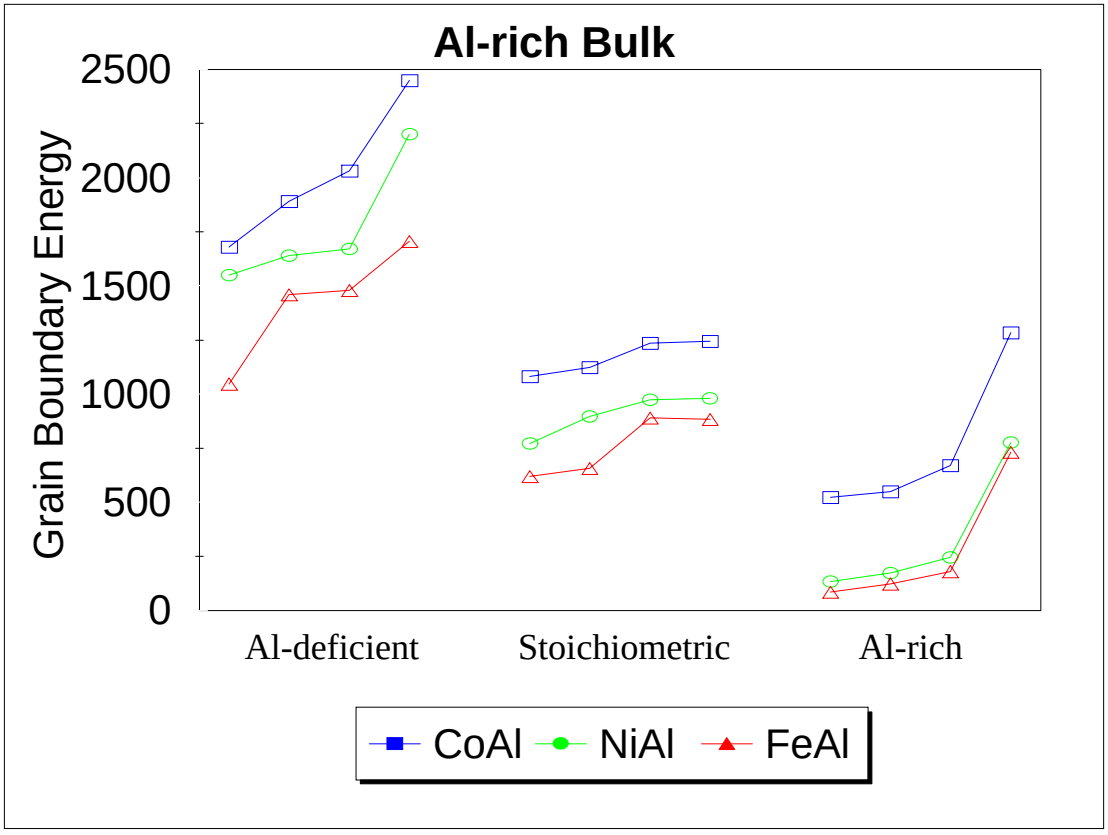

Figure 5.19: Stoichiometry trends of the grain boundary energy for the $\Sigma = 5(210)[001]$ symmetric tilt grain boundary in B2 intermetallic compounds. The energy (in mJ/m^2) is shown, in an Al-rich Bulk, as a function of the local grain boundary composition.

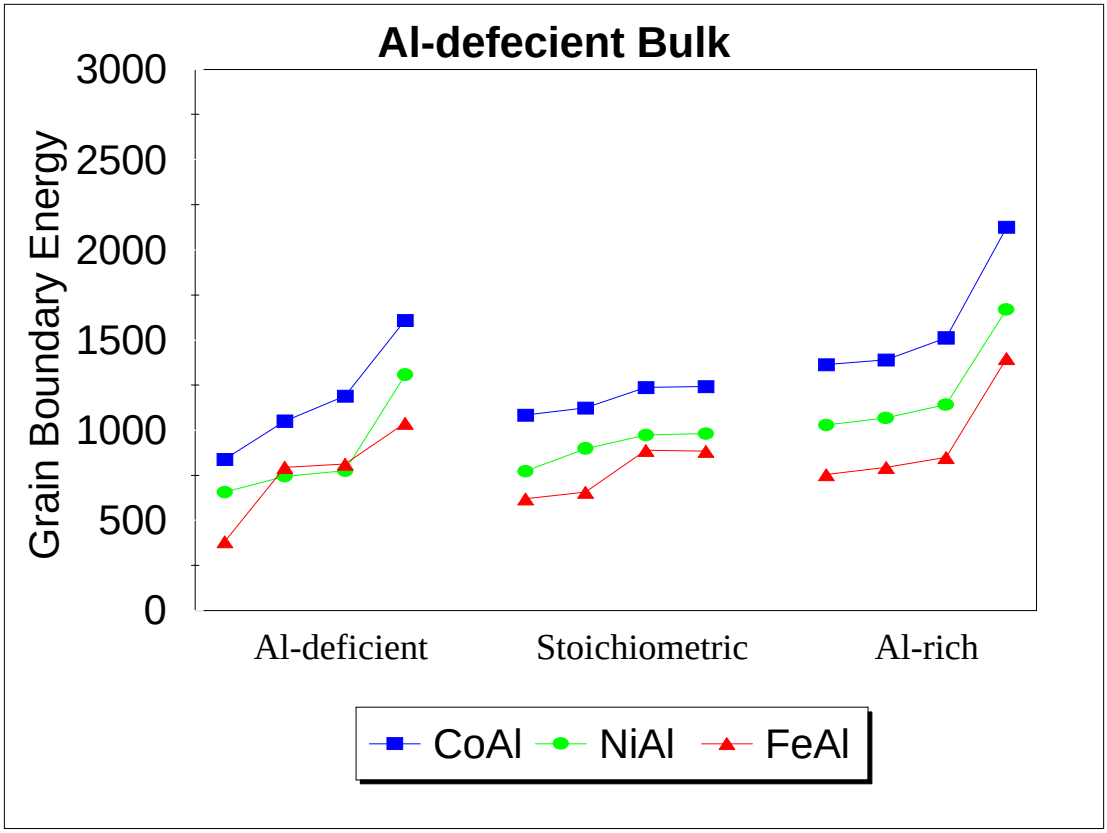

Figure 5.20: Stoichiometry trends of the grain boundary energy for the $\Sigma = 5(210)[001]$ symmetric tilt grain boundary in B2 intermetallic compounds. The energy (in mJ/m^2) is shown, in an Al-deficient Bulk, as a function of the local grain boundary composition.

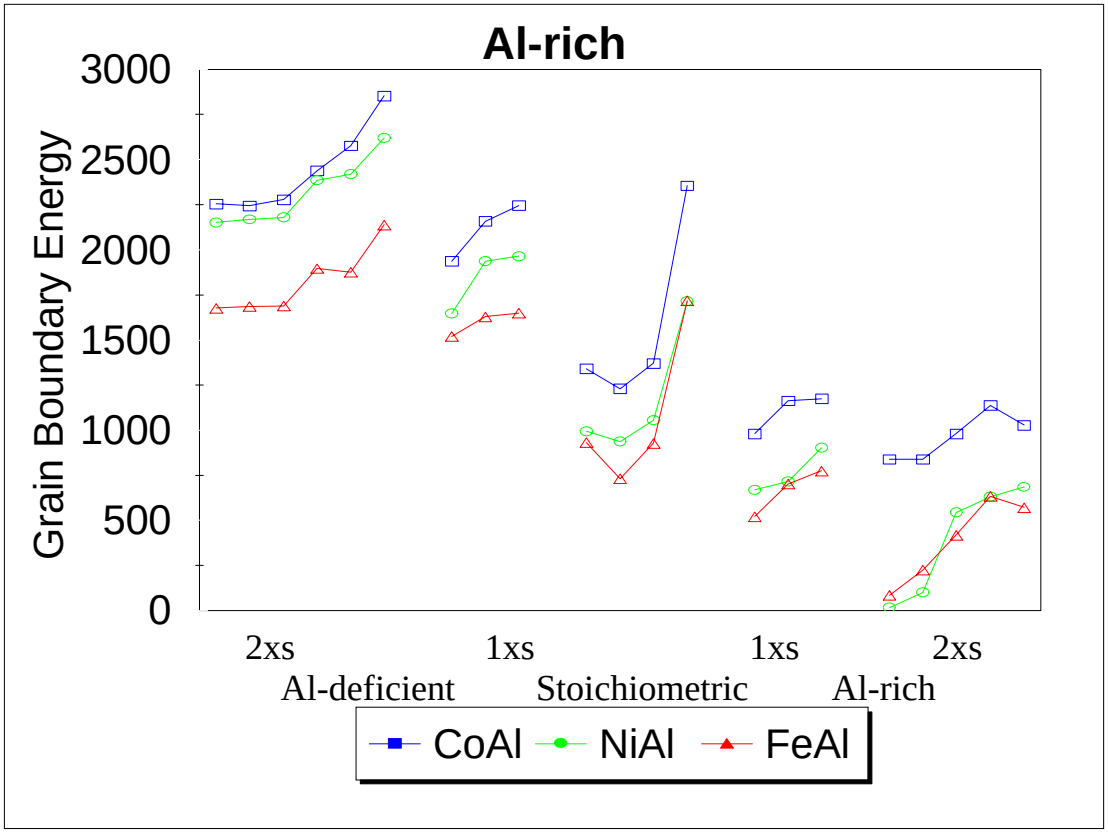

Figure 5.21: Stoichiometry trends of the grain boundary energy for the $\Sigma = 5(310)[001]$ symmetric tilt grain boundary in B2 intermetallic compounds. The energy (in mJ/m^2) is shown, in an Al-rich Bulk, as a function of the local grain boundary composition.

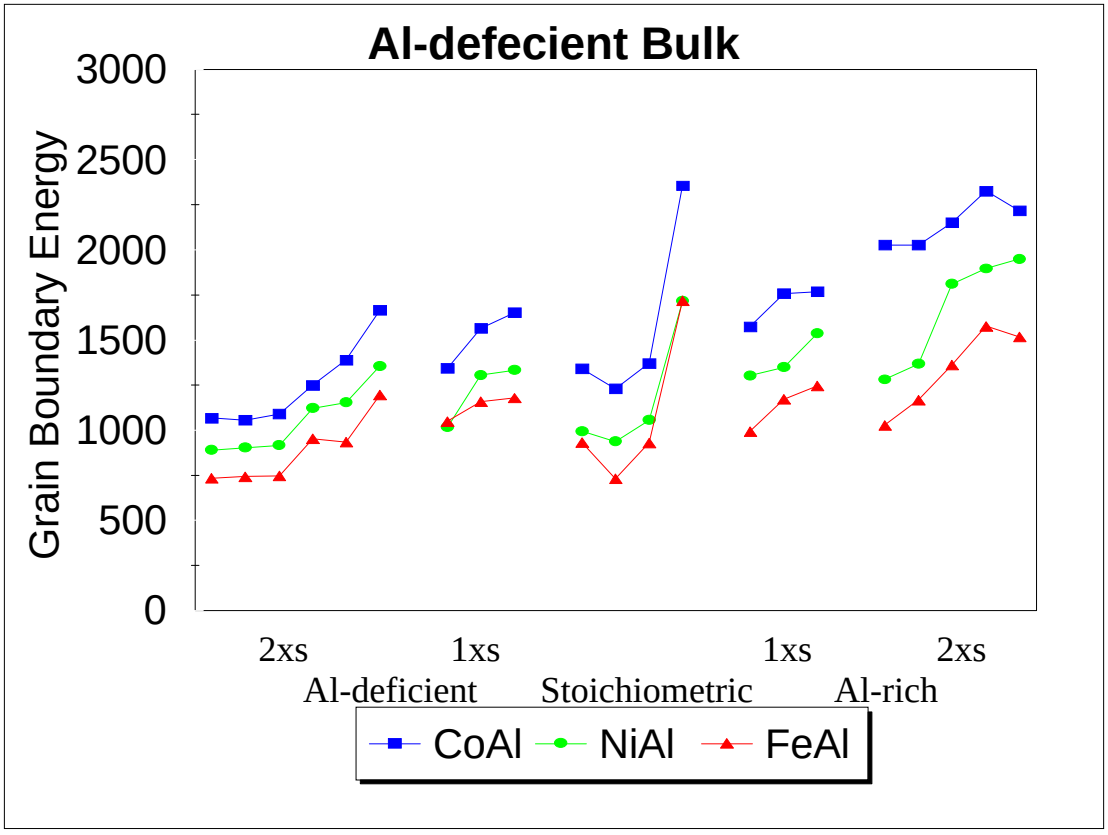

Figure 5.22: Stoichiometry trends of the grain boundary energy for the $\Sigma = 5(310)[001]$ symmetric tilt grain boundary in B2 intermetallic compounds. The energy (in mJ/m^2) is shown, in an Al-deficient Bulk, as a function of the local grain boundary composition.

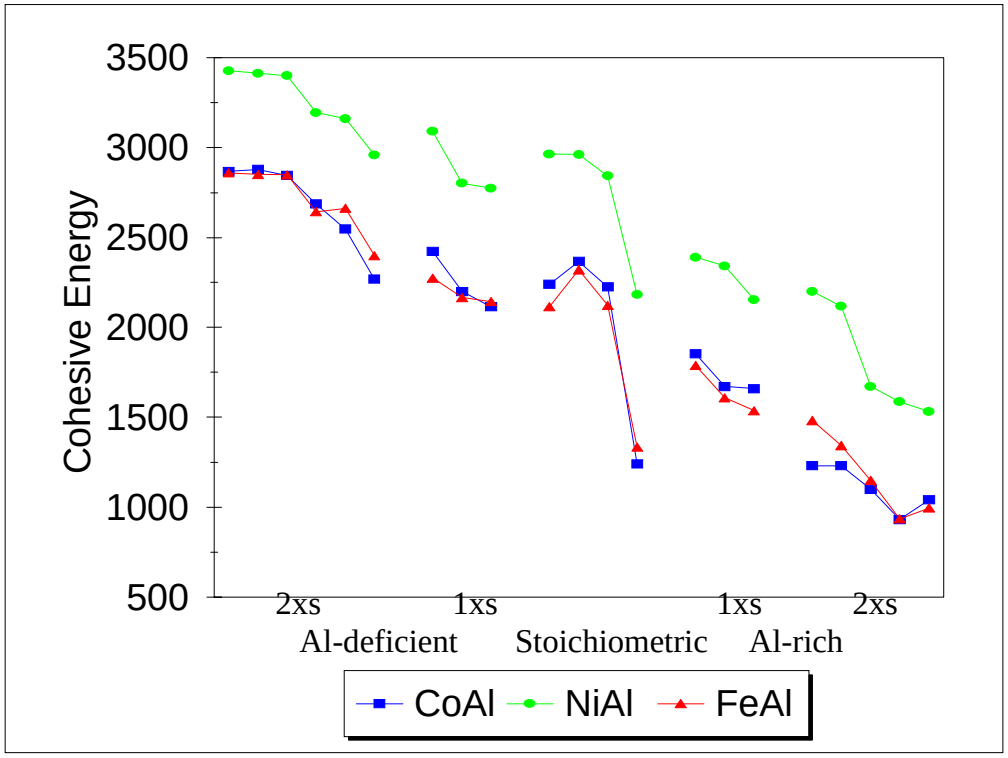

Figure 5.23: Cohesive energy trends for the $\Sigma = 5(310)[001]$ symmetric tilt grain boundary in B2 intermetallic compounds. The energy (in J/m^2) is shown as a function of the local grain boundary composition.

Table 5.1: Calculated relaxed surface energies (in mJ/m^2) showing different terminations in the B2 aluminides in an Al-deficient Alloy.

Surface Composition	Surface energy (mJ/m^2)		
	CoAl	NiAl	FeAl
{210} Surface			
Al-deficient (1xs)	1613	1767	1261
Al-deficient (2xs)	1494	1619	1069
Al-rich (1xs)	1915	2062	1695
Al-rich (2xs)	2035	2210	1887
Average	1764	1915	1478
{310}Surface			
Al-deficient (1xs)	1883	1845	1662
Al-deficient (2xs)	1798	1741	1255
Al-rich (1xs)	1713	2054	1391
Al-rich (2xs)	1797	2158	1798
Stoichiometric	1798	1949	1526

5.4.6 Boundary ductility criterion

Grain boundary energy and grain boundary cohesion are not the only factors that determine the measure of ductility of these compounds; other factors such as the shear modulus, unstable stacking faults and the modes of slip across the boundary may play a role. A possible criterion of grain boundary ductility can be developed by analogy to the Rice criterion for bulk materials [74]. The Rice criterion is a semi-quantitative criterion for determining the intrinsic ductile versus brittle behavior of materials in terms of the competition between crack cleavage and dislocation emission from the crack tip. We used $2\gamma_{us}/\gamma_{coh}$, where γ_{us} is the unstable stacking fault energy which is the energy barrier required for the block like sliding of one half of the crystal relative to the other along the slip plane. The values forγ_{us} were calculated for the $\langle 111\rangle\{110\}$ slip system. γ_{us} is used as a measure of the ease of dislocation emission from a crack tip, whereas the cohesive energy, γ_{coh}, is a measure of the ease of crack propagation along the grain boundary. The results obtained using this criterion are shown, for the $\Sigma = 5(310)[001]$ symmetric tilt grain boundary, in Figure 5.24

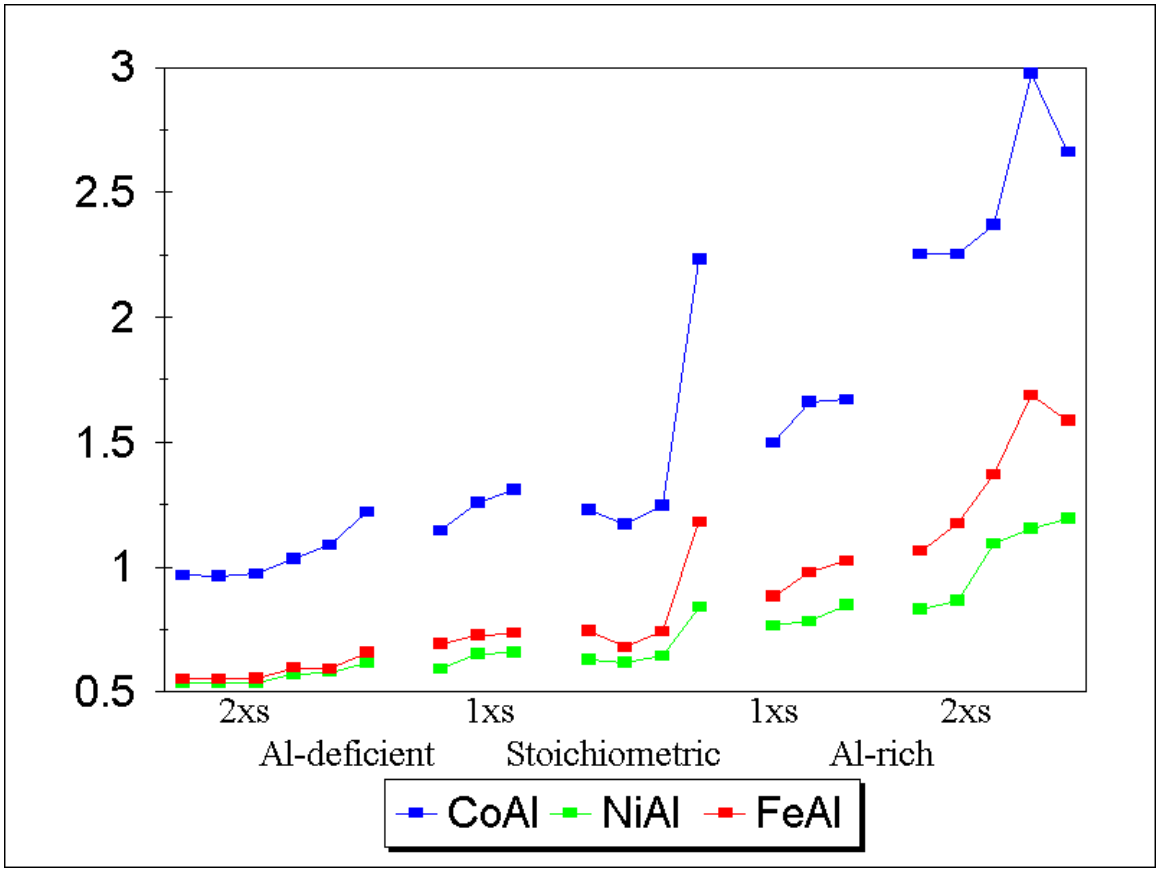

Figure 5.24: Trends in the criterion $2\gamma_{us}/\gamma_{coh}$ for the $\Sigma = 5(310)[001]$ symmetric tilt grain boundary in B2 intermetallic compounds.

5.5 Discussion

From the simulations of grain boundary structures it was found that CoAl tends to have the highest grain boundary energies and FeAl the lowest, except for some structures in which NiAl has lower grain boundary energies than FeAl. Specifically, CoAl grain boundary energies are, on average, 25 to 50% higher than those for NiAl and FeAl. In agreement with previous work on $L1_2$ Ni_3Al [73], [46] and B2 NiAl [47], it was found in this study that boundary energy is related to the local boundary composition. It was also found that there exists an energy dependence of the defect, on the stoichiometry of the total block which contains the boundary. Off-stoichiometric boundary and free surface energies not only depend on the composition of the boundary but also on the block that contains them. Namely, increasing the Al content in the grain boundary leads to an increase in the boundary energy if the bulk stoichiometry is Al-deficient, but leads to a decrease in the boundary energy if the bulk that contains the defect is Al-rich or stoichiometric (Figure 5.19 to 5.22) . This effect is observed in all the three B2 compounds that were studied: there is a 30 to 75% energy difference between the Al-deficient and Al-rich boundaries within a given bulk stoichiometry. The effect of Al content increase is more pronounced in Al-rich bulks than in the Al-deficient bulk stoichiometries.

In these compounds, the cohesive energy decreases with increasing Al content. These low cohesive energy structures have an Al-rich boundary composition and tend to appear in Al-rich and stoichiometric bulks. They are not favored in Al-deficient bulks. It can therefore be surmised that the tendency towards brittle behavior decreases for Al-deficient alloys.

Trends observed for the free surface energy in the compounds studied (Table 5.1) showed the highest energies for NiAl and the lowest for FeAl. This behavior is consistent with that of the cohesive energy of the boundaries. Using equation (4.2) it is seen that the (210) plane has the higher grain boundary cohesive energies for all the structures studied. NiAl has the highest boundary cohesive energies and FeAl the lowest for the grain boundaries studied.

The combination $2\gamma_{us}/\gamma_{coh}$ can be used as a criterion of grain boundary ductility. The values of $2\gamma_{us}/\gamma_{coh}$ between 0.2 and 0.4 are characteristic of the ductile to brittle transition in B2 inter-

metallics [75]. The values of $2\gamma_{us}/\gamma_{coh}$ for CoAl are above 0.6, which is consistent with the strong tendency of this compound for grain boundary brittleness.

5.6 Conclusions

Different grain boundaries for the series of B2 compounds, CoAl, NiAl to FeAl, were simulated using the embedded atom method, and their energies calculated using the thermodynamically consistent method proposed by Hagen and Finnis [61]. The structures and energies were compared to obtain trends in the B2 compounds. A variety of structures of the same grain boundary with very similar energies is possible in ordered intermetallic compounds. The defect structures that were simulated are very similar and the structural trends for the boundaries are consistent in the three compounds. Dislocations or APB's reaching the boundary can cause transformations between the different structures and this may influence the mechanical response of the grain boundary region. The grain boundary energies increase in the series of compounds FeAl-NiAl-CoAl. The energy of the boundaries were found to be dependent on the composition of the boundary and the composition of the bulk embedding the boundary.The energy ratio of FeAl/CoAl is fairly constant.

Chapter 6

INTERFACES IN γ-TiAl

6.1 Introduction

Considerable attention has been focused on intermetallic alloys based on γ-TiAl, with the $L1_0$ (CuAu) structure, as high-temperature structural materials because of their low density and attractive properties at high temperatures, such as good oxidation resistance and high mechanical strength. A major handicap, in their applicability, is their low ductility up to about 700^oC. Much effort has been concentrated on the two-phase $(\alpha + \gamma)$ lamellar structure because its properties are superior to those of either single-phase α *or* γ. Of interest in these materials are the γ-γ interfaces within the γ and $\alpha+\gamma$ lamellar domains, since their structure can affect dislocation and deformation twin propagation through the matrix.

The importance of deformation twinning in the mechanical behavior of intermetallic compounds has been studied [76] [33]. Twinning has been found to be a significant deformation mechanism, and the activation of twinning can possibly increase the number of independent deformation modes.

The present work addresses the question of both grain boundary and twin boundary structure in the $L1_0$ structure. Despite the technological importance of this material, few atomistic studies of the interfaces in this structure have been performed. The interface structures and energetics are of interest because it is widely accepted that the role of deformation twinning in generalized plastic deformation and fracture toughness is of special importance in the $L1_0$ structure and the activation of twinning can improve mechanical properties, such as ductility.

In this work, stoichiometric structures for symmetrical tilt boundaries were computed, as were twin interfaces with different orientations. The calculations for the twin interfaces were carried out for both twinning and pseudo-twinning orientations. The boundaries chosen for detailed study were

the $\Sigma5\{210\}$, $\Sigma3\{111\}$, $\Sigma3\{11\bar{2}\}$, and $\Sigma6\{1\bar{2}1\}$. The computations discussed herein were performed using "molecular statics" and the embedded atom method.

6.2 Interatomic Potentials and Simulation Procedure

The atomistic simulations for this work used EAM (Embedded Atom Method) local-volume dependent potentials proposed by Daw and Baskes [50]. The interatomic potentials used for TiAl incorporated the Ti potentials developed by Pasianot and Savino [56], who accounted for the contribution of the inner elastic constants. The electron density and embedding functions for Al were those developed by Voter and Chen [53]. The mixed Ti-Al potential, which reproduces the properties of the $L1_0$ phase in TiAl, was that developed by Farkas [54]. The c/a ratio is greater than unity, in agreement with experimental data. Details of the fitting procedure are discussed elsewhere [54]. The set of potentials used correctly predicts the point defects that accommodate off-stoichiometry; antisites on both sides. As part of the testing process of these potentials, properties of various defects were computed [54].

The initial structures for energy minimization were generated using a c/a ratio of one, with a = $4.025\mathring{A}$, to avoid lattice mismatch at the interfaces. The initial structures of (210) grain boundaries were generated by reflecting a semi-infinite perfect crystal against the $(1\bar{2}0)$ plane. Two (111) boundaries were computed by reflecting against $(1\bar{2}1)$ and $(11\bar{2})$ and both the $(11\bar{2})$ and $(1\bar{2}1)$ boundary structures were computed by reflecting against (111). Variants of the boundary structures were obtained by rigid-body translations applied to one of the crystals and lead to different types of matching between the two crystals without changing their misorientation or the position of the boundary plane. The difference in atomic distribution and sublattice occupation, thus obtained, leads to the structural variants in the boundary region.

The boundary structures obtained by the above geometrical constructions were used as starting configurations for the subsequent structural relaxations. The structural relaxation procedure was the standard "molecular statics" technique using the conjugate gradient method for the energy minimization. Periodic boundary conditions were imposed in the directions parallel to the boundary

plane, while fixed boundary conditions were applied normal to the boundary plane. The total energy was also minimized with respect to possible rigid body displacements of one crystal relative to the other.

6.3 Twins and Pseudo-Twins

In ordered compounds, since dislocation slip is usually restricted by the lower mobility of dislocations, twinning becomes an important mode of plastic deformation. Deformation twinning becomes important not only at lower temperatures and high strains but also at lower strains and higher temperatures. A deformation twin can be considered to be a region of a crystal that has undergone a shear such that the resulting structure is identical to the parent lattice, but oriented differently. In true twinning, the transformation changes the orientation, but does not alter the structure or symmetry of the crystal. It can be considered a special type of grain boundary, which results when mirror symmetry occurs on either side of the boundary plane. The crystallography of deformation twinning in cubic and non-cubic superlattice structures based on the bcc or fcc structures has been extensively investigated [76] . In non-cubic superlattices, twinning shears in variants of the usual disordered mode can result in true twins or pseudo-twins.

The ordered γ-TiAl phase has a face centered tetragonal structure with a c/a ratio of 1.02. The structure is composed of alternate (002) planes of 100% Ti and 100% Al. In the following, the mixed notation $\langle$hkl] is used to indicate a set of equivalent crystallographic directions which are generated by permutations of $\pm$h and $\pm$k; only a sign change is allowed for l. The structure possesses two non-equivalent projections along the $\langle 110 \rangle$ directions; $\langle 101]$ and $\langle 110]$ due to the tetragonality of the $L1_0$ structure as shown in Figure 6.1. The main difference between the $\langle 101]$ and $\langle 110]$ type directions is the stacking sequence. The $\langle 101]$ type directions are composed of 50% Ti and 50%Al, where as the $\langle 110]$ type directions consist of either 100% Ti or 100%Al.

Twinning observed in TiAl is of the $\{111\}\langle 11\bar{2}]$ type, which are the variants in which the $L1_0$ superlattices are mechanically twinned without disturbing the $L1_0$ symmetry of the lattice. When the $L1_0$ structure is deformed by shear corresponding to other variants of the twinning mode of the

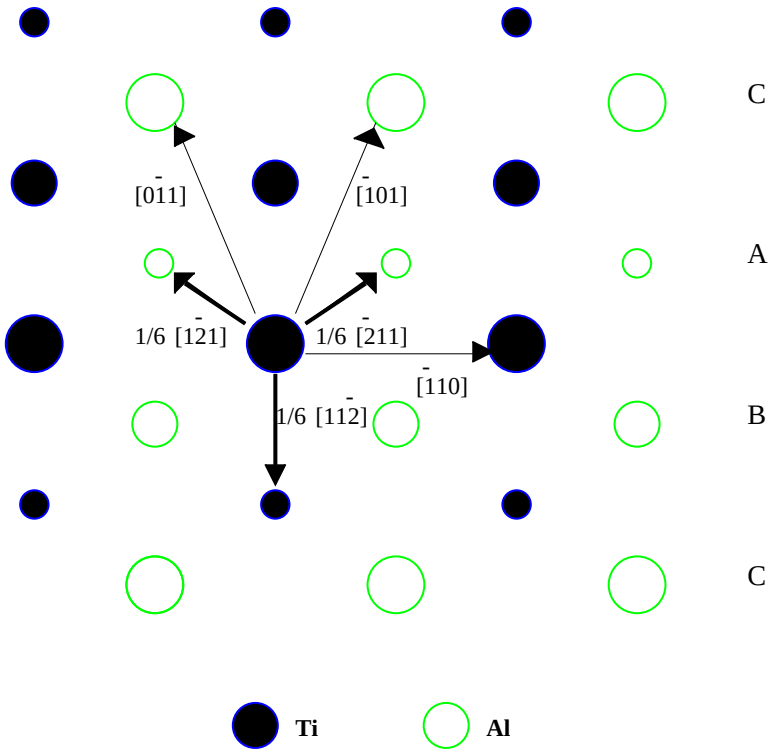

Figure 6.1: Schematic diagram of stacking sequence of (111) planes in TiAl

fcc structure, the $L1_0$ structure is no longer preserved. Figure 6.1 shows three possible twinning vectors (dark arrows); the $1/6[11\overline{2}]$ which leads to true twins and the $1/6[\overline{2}11]$ and $1/6[1\overline{2}1]$ which yield pseudo-twins. Twin boundaries can be described in the framework of the CSL model with $\Sigma 3$ true twins and $\Sigma 6$ pseudo twins. In ordered materials, even Σ values are possible and indicate a change in ordering across the interface.

6.4 Interfacial γ-Surfaces

Grain boundary γ-surfaces were computed for TiAl along the {210} planes and calculations were also carried out for the twin orientations; {111} and $\{1\overline{2}1\}$. The two blocks of atoms defined on both sides of the boundary plane were rigidly displaced according to fault vectors with components in the X and Z directions (within the boundary plane). The method for simulating the faults is similar to that originally proposed by Vitek [72]. Rigid body translations of one grain with respect to the other, gives rise to a multiplicity of possible boundary structures and accompanying energies. The energetics of this multiplicity can be studied by plotting the energy of the boundary against the rigid body displacements parallel to the grain boundary plane. This is termed the boundary γ-surface. The energies for these grain boundary γ-surface configurations were computed after relaxation in only the Y direction (perpendicular to the boundary plane). This method of computing and presenting the boundary was carried out for all the boundaries under consideration.

This technique of boundary representation gives a good visual method for determination of local minima and directions of lowest energy. The structures that coincide with the minima are the stable structures. The γ-surfaces are visualized as contour plots of the energy as a function of the rigid body displacements. These γ-surfaces were created by the computation of 300 to 2000 boundary energies in order to scan the entire plane under study. From the scan of the planes, the positions of the minima were identified and the corresponding structures and their resultant energies were computed, allowing for complete relaxation parallel and perpendicular to the boundary plane. The contour plots of the simulated {210} grain boundary γ-surface is presented in Figure 6.2. Figures 6.4 to 6.9 show the contour plots for the twin and pseudo-twin interfaces. Darker shades correspond to

lower energies. For all the γ-surface computation, a full boundary period is used in each direction. The boundary period is defined as $a\sqrt{h^2 + k^2 + l^2}$ of the respective directions parallel to the grain boundary plane.

6.5 Results and Discussion

γ-surfaces for the interfaces in TiAl were computed for {210}, {111} and $\{1\overline{2}1\}$ orientations. These γ-surfaces are shown in Figures 6.2, 6.4, 6.5, 6.9 and 6.10. From the computed γ-surfaces, the positions of the minima were identified and the corresponding structures and their resultant energies were computed, allowing for complete relaxation parallel and perpendicular to the boundary plane. Figures 6.3 6.7, 6.8, 6.11 and 6.12 show the relaxed structures for these interfaces. The circles depict Al and the triangles the Ti. Color variations of the symbols represent different planes of the respective tilt axis. The polyhedra delineate boundary repeat units and the line corresponds to the boundary plane.

6.5.1 {210} Boundary

γ-surfaces were computed for a stoichiometric {210} grain boundary in TiAl using rigid body displacements parallel to the grain boundary plane. These displacements were along the $[1\overline{2}0]$ and [001] directions. The [001] projection is mixed, in that it contains an equal number of Ti and Al atoms. This is shown in Figure 6.2. The topology of the {210} γ-surface is similar to that of the {310} γ-surface in B2 compounds shown in Chapter 5.

For this boundary, two minima were observed; one with no shift along either direction and another at half the boundary plane in both directions, $[1\overline{2}0]$ and [001]. The corresponding structures are shown in Figures 6.3(a)and 6.3(b). The deeper minima was observed at the position with no shift, Figure 6.3(a). The lowest energy structures has an energy of 857 mJ/m^2, while the structure with a shift along the tilt axis has an energy of 998 mJ/m^2.

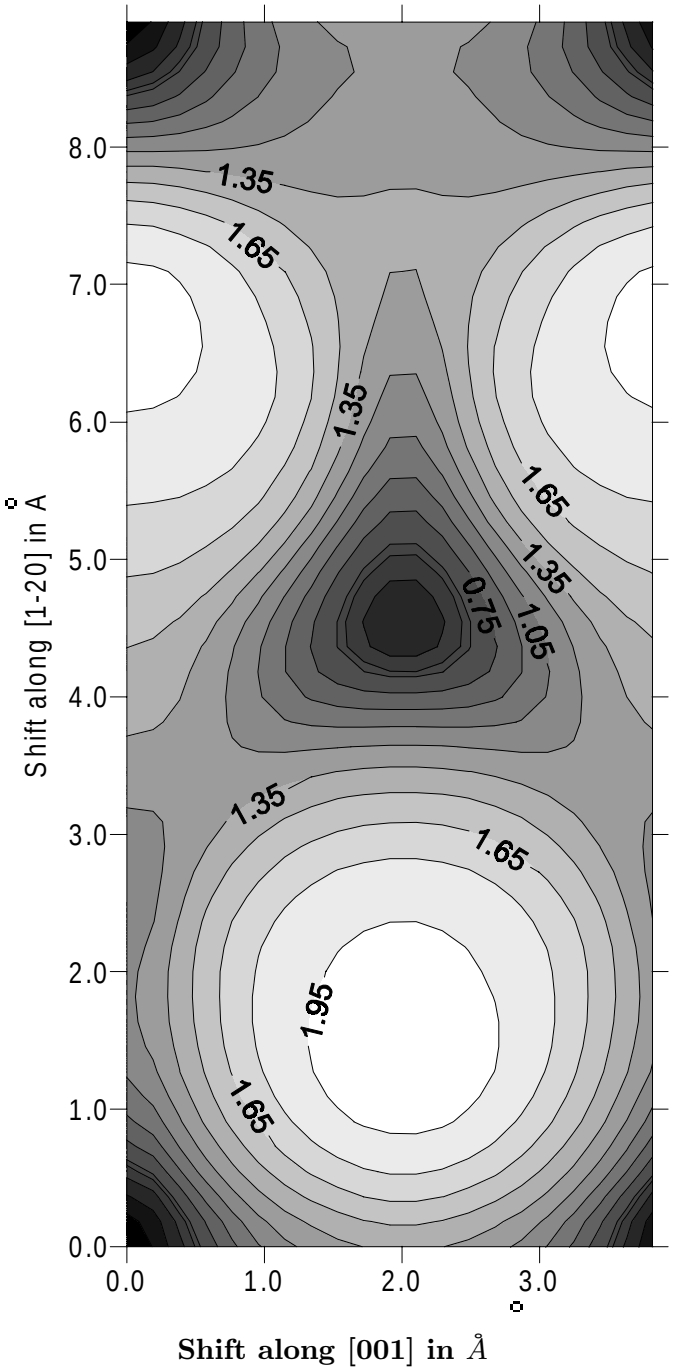

Figure 6.2: Computed stoichiometric {210} boundary γ-surface .

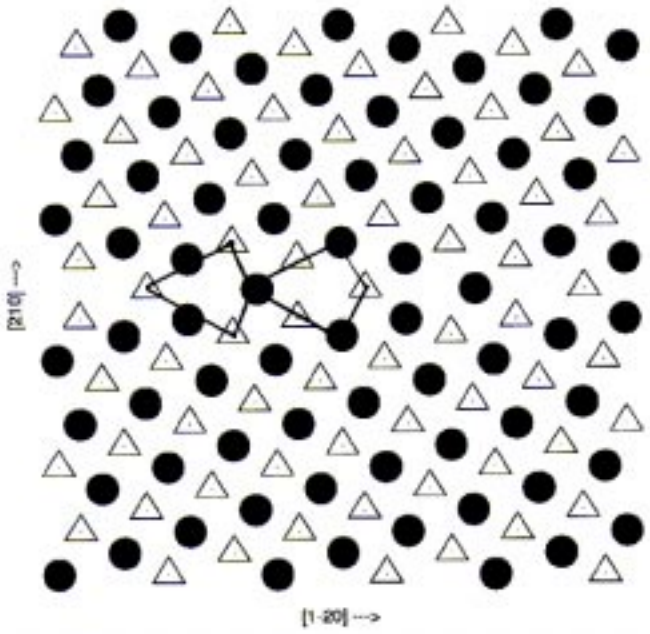

(a)

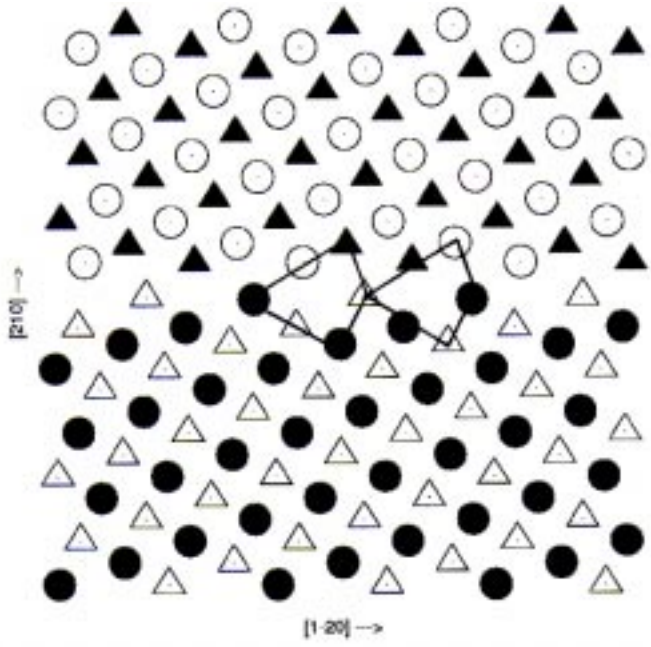

(b)

Figure 6.3: Stoichiometric structures of the $\Sigma_{\overline{103}} = 5(210)[001]$ symmetric tilt grain boundary.

6.5.2 {111} Boundaries

Because of the tetragonal nature of the $L1_0$ structure, in the (111) plane there are two non-equivalent projections along the $\langle 110 \rangle$ directions; $\langle 101]$ and $\langle 110]$. This difference as shown in Figure 6.1 is due to their stacking sequence. For this reason, two different types of {111} boundaries were computed with the $\langle 110 \rangle$ directions as the tilt axes. γ-surfaces were computed with rigid body displacements applied along the $[1\bar{1}0]$ and $[11\bar{2}]$ for one and along the $[10\bar{1}]$ and $[1\bar{2}1]$ for the other. The first orientation gives rise to twinning (Figure 6.4) and the second choice results in pseudo-twinning (Figure 6.5). The general topology of both γ-surfaces is the same. The difference lies, not only in the depth of the minima between the two γ-surfaces, but also in the relative depths of the minima within each γ-surface.

In the twinning orientation, two non-energetically equivalent minima were observed. The lowest minima type is located when no shifts are applied in any direction. Due to the crystal symmetry this is equivalent to the structure with a rigid body displacements of $1/6\langle 112]$ or $1/2[1\bar{1}0]$. This corresponds to the true twin position (Figure 6.7(a)). The other type of minima observed at a shift of $1/2\langle 10\bar{1}]$ and also at $1/6\langle 2\bar{1}\bar{1}]$ are energetically and structurally equivalent. It should be noted that the minima at this position is very shallow. The structure at this minima is shown in Figure 6.7(b).

Figure 6.7(a) shows the true twin {111} structure which exhibits no shifts in the directions contained within the twinning plane. The projection down the tilt axis, $[1\bar{1}0]$, shows rows consisting of either all Ti or Al. The energy of this structure is $30 \mathrm{mJ/m^2}$. The structure shown in Figure 6.7(b) is a twin with a shift of $1/2[10\bar{1}]$ of the upper crystal. This structure differs from the pure twin in that though the atomic site positions of the twin are maintained, a change in atom types in the upper grain is observed. This structure has an energy of 298 $\mathrm{mJ/m^2}$. From the γ-surface this structure corresponds to minima with positions close to a twin combined with an APB (anti phase boundary) or a twin combined with a CSF (complex stacking fault). A schematic of the {111} γ-surfaces showing the equivalent structures and their positions is shown in Figure 6.6. The energies of the APB and CSF have been computed elsewhere, using these potentials [77] with energies of

322 and 308 mJ/m^2 respectively.

The minima of the pseudo-twinning orientation, (Figure 6.5), are energetically degenerate and, as expected, the resultant structures at these minima are structurally equivalent. The only difference being in the position of the boundary plane. Figure 6.8 shows the resultant pseudo-twin. The projection down the tilt axis, $[10\overline{1}]$, shows rows consisting of 50% Ti and 50% Al. The energy of this structure is 109 mJ/m^2.

To summarize, the {111} orientation yields three distinct interfacial structures; the pure twin, the twin with either an APB or CSF and the pseudo-twin. As expected, the twin has the lowest energy. The energy of the twin with APB is more than twice that of the pseudo-twin. The ratios of energies from the simulations are 1:3.6:9.9 for twin: twin + APB: pseudo-twin. From the simulation results of the energies of an APB (322 mJ/m^2) and that of a twin + APB (298 mJ/m^2), it can be suggested that for systems which separately contain both an APB and a twin, it is energetically favorable for the two to combine and form a twin with an APB across the twinning plane.

6.5.3 $\{1\overline{2}1\}$ Boundaries

As discussed earlier the tetragonal ordering of the $L1_0$ lattice leads to the $(1\overline{2}1)$ and $(11\overline{2})$ planes being inequivalent. In a stoichiometric alloy, the $(11\overline{2})$ planes consist of alternating planes of 100% Ti and 100% Al and the $(1\overline{2}1)$ planes are composed of equal numbers of Ti and Al. Due to this inequivalency, the two types of γ-surfaces were computed for stoichiometric compositions. The resultant contour plots are shown in Figures 6.9 and 6.10 for the $(11\overline{2})$ and $(1\overline{2}1)$ boundaries respectively.

The $(11\overline{2})$ γ-surface is symmetric about the $[1\overline{1}0]$ direction and possess only two minima. These two minima were shown to be energetically and structurally degenerate. The structure is given in Figure 6.11. The upper grain shows a shift of a/4$[1\overline{1}0]$ with respect to the lower grain. The relative atomic site positions of the twin are maintained except for a small shift along [111]. The energy for this interface is 340 mJ/m^2.

The $(1\overline{2}1)$ γ-surface is shown in Figure 6.10. Due to the inequivalency of the $\langle 110 \rangle$ directions, no symmetry was observed along the $[10\overline{1}\,]$ direction, as in the previous case. Three minima were

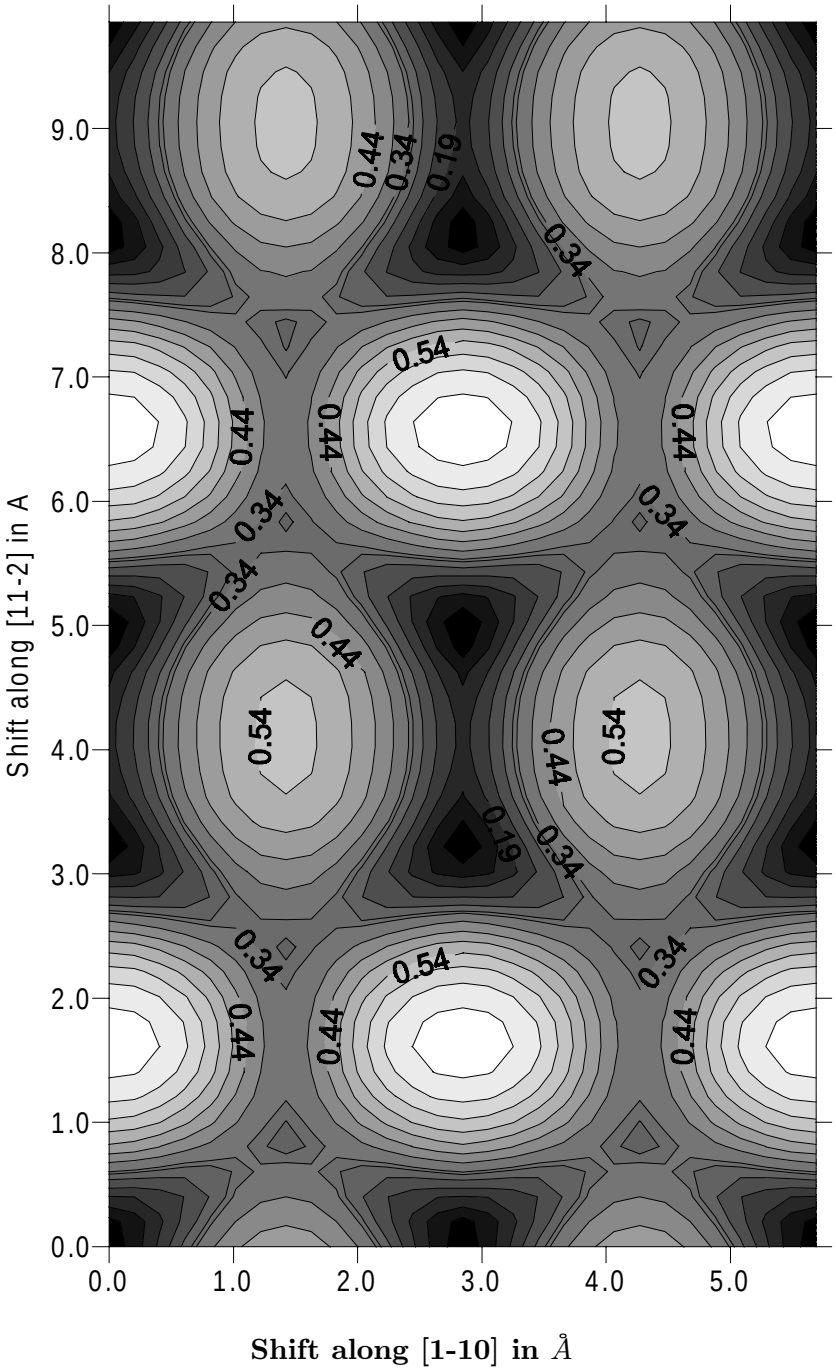

Figure 6.4: Computed {111} twin boundary γ-surface. (Energies are in J/m^2)

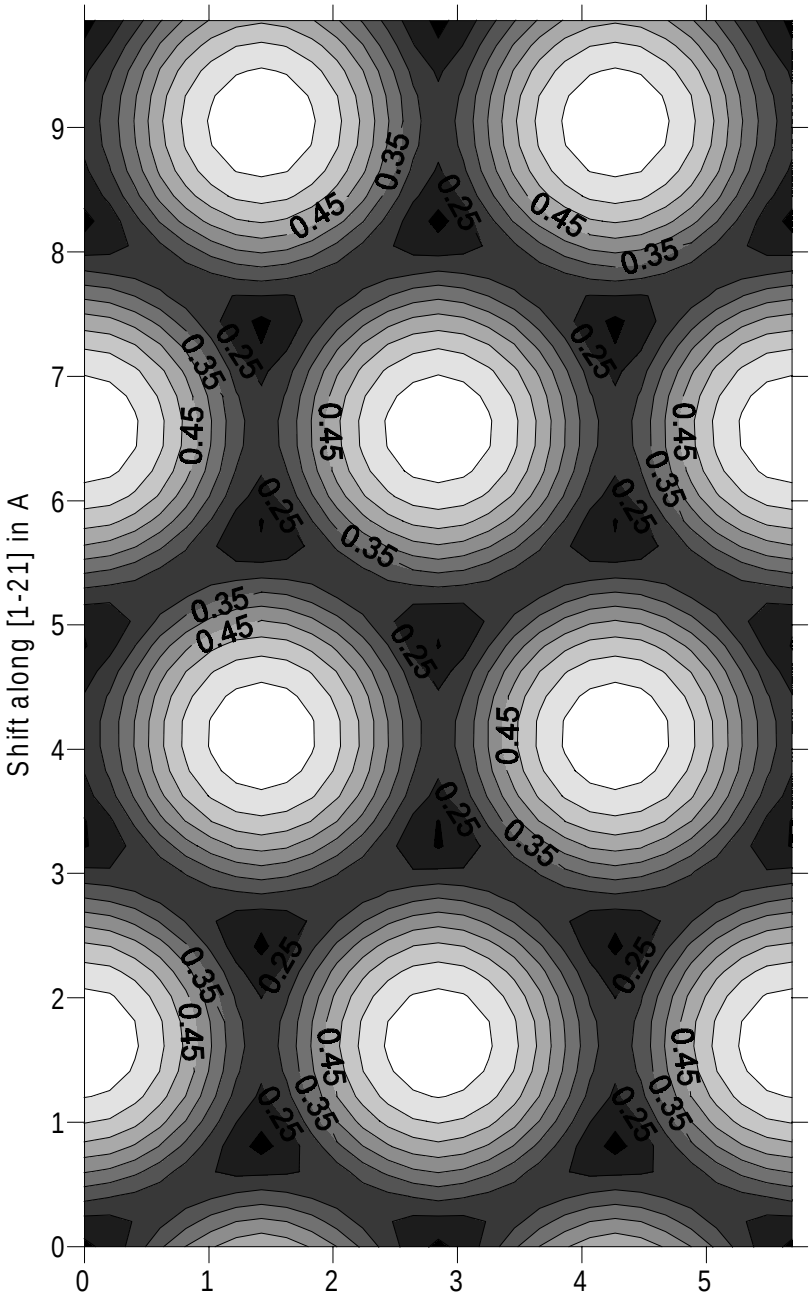

Figure 6.5: Computed {111} pseudo-twin boundary γ-surface. (Energies are in J/m^2)

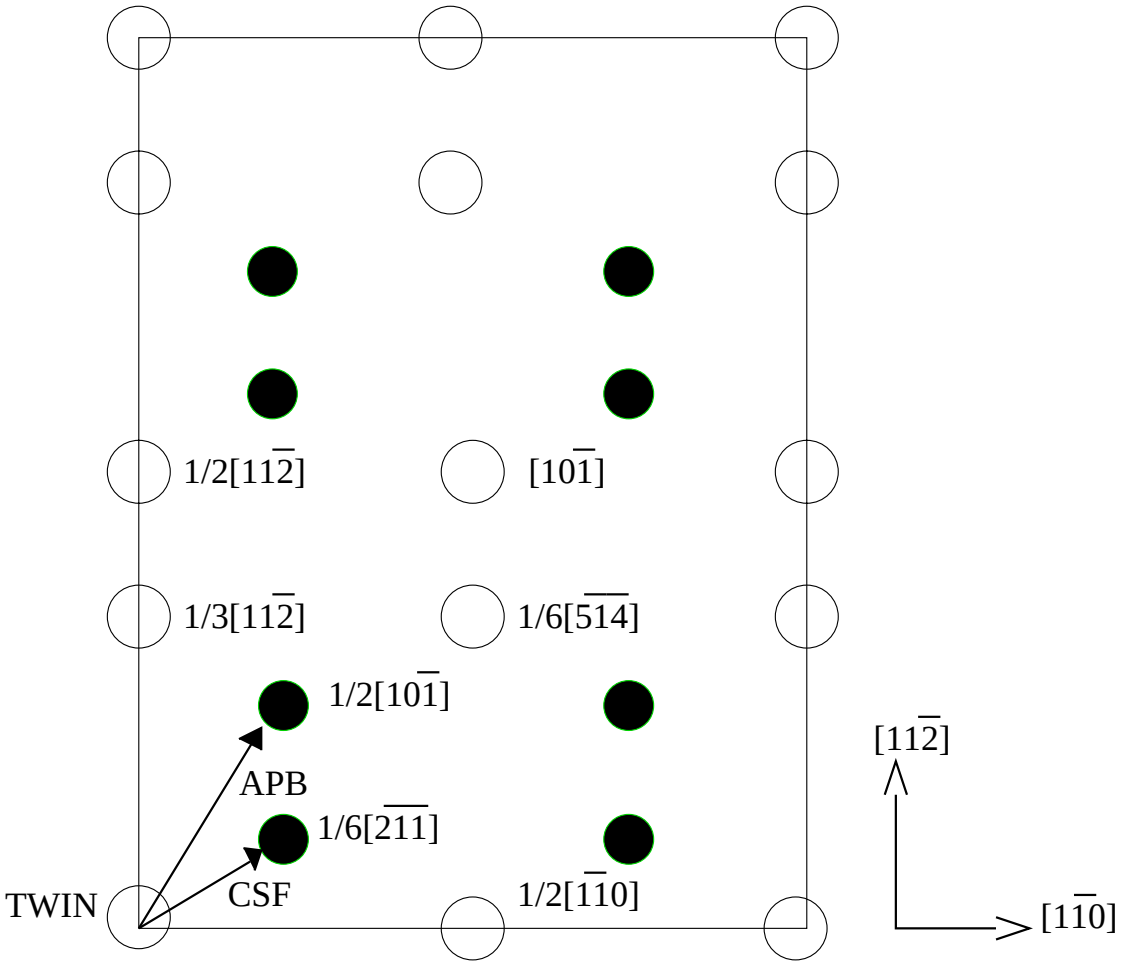

Figure 6.6: Schematic diagram showing equivalent structures from the computed{111} twin boundary γ-surface. Equivalent structures shown by the same symbol.

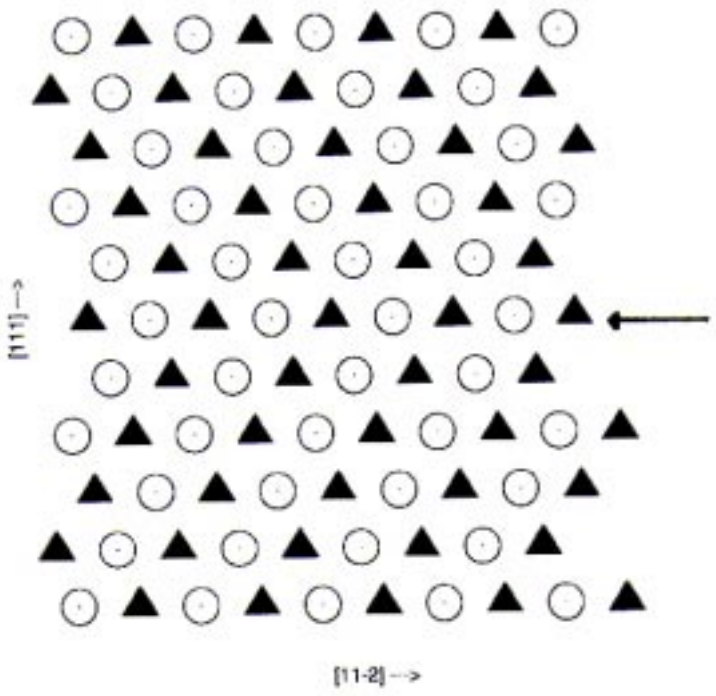

(a)

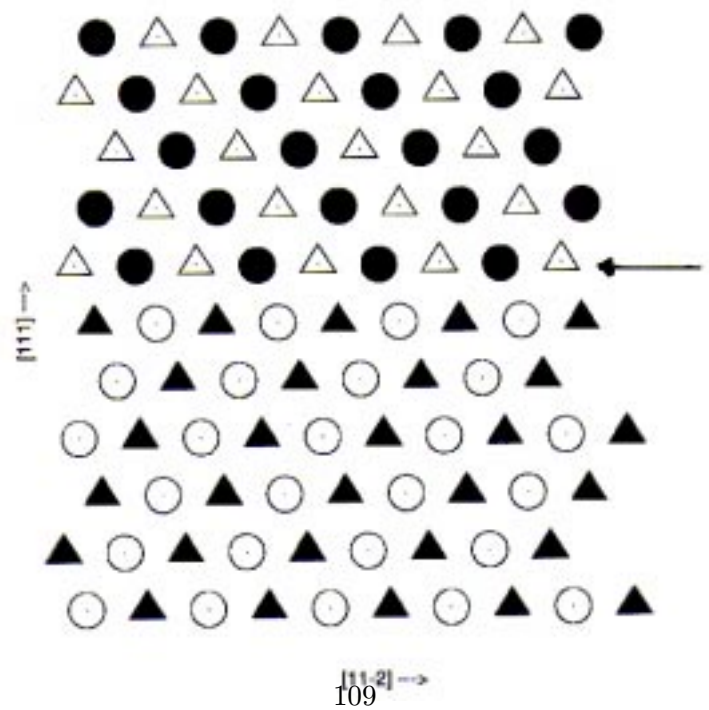

(b)

Figure 6.7: Structures of the {111} twin boundary.

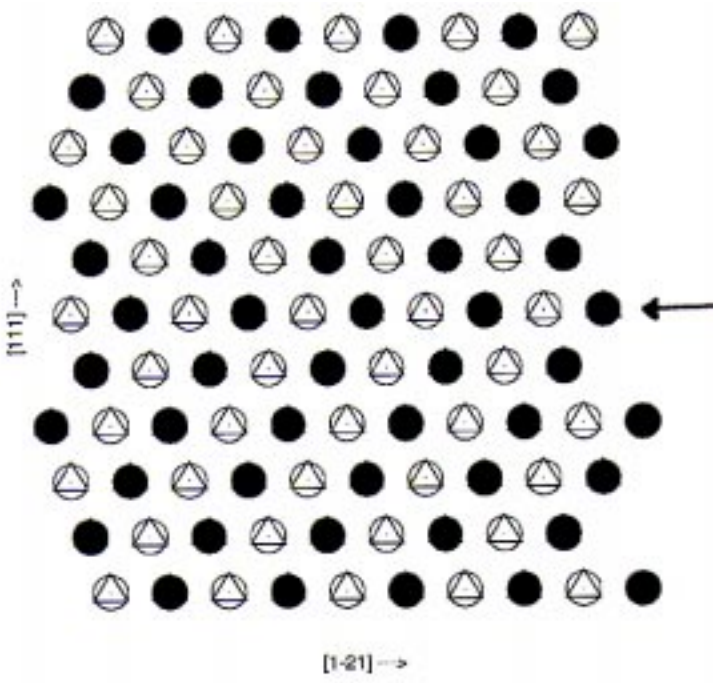

Figure 6.8: Structure of the {111} pseudo-twin boundary.

observed; two equivalent minima with shifts of $3/4[10\overline{1}]$ along the $[10\overline{1}]$ direction were shown to be equivalent (Figure 6.12(a)) and one minima with a shift of $1/4[10\overline{1}]$ along the same direction (Figure 6.12(b)) . The lowest energy structure, (Figure 6.12(a)), has an energy of 497 mJ/m^2 and the other minima structure has an energy of 602 mJ/m^2. The latter structure has near perfect matching at the interface, whereas the lowest energy structure is a strained variant of this. The relative shift along [111] of the two crystals results in a lowering of the energy.

The energy of the twin type interface is lower than the pseudo-twin type in the $\{1\overline{2}1\}$ orientation. This is similar to the $\{111\}$ interfaces. The energy ratio; twin type: pseudo-twin type is 1:1.5 - 1.8 for $\{1\overline{2}1\}$ orientation.

6.6 Discussion and Conclusions

An atomistic study of a number of different interfaces in TiAl was undertaken. Boundary γ-surfaces were computed for all the orientations chosen for detailed study, as were the low energy structures. Three distinct variants of the $\{111\}$ interface structure were observed namely the twin, the twin with APB and the pseudo twin. The twin, as expected had the lowest energy of 30 mJ/m^2, the twin with APB had an energy of 298 mJ/m^2 and the energy of the pseudo-twin was 109 mJ/m^2. The structure and energy of the twin with APB was observed to be the same as that for a twin with CSF. Both the $(1\overline{2}1)$ and (210) boundaries had two different low energy structures and the $(11\overline{2})$ interface had one. The twin type structures were shown to have the lowest energies in both the $\{11\overline{2}\}$ and $\{111\}$ interfaces.

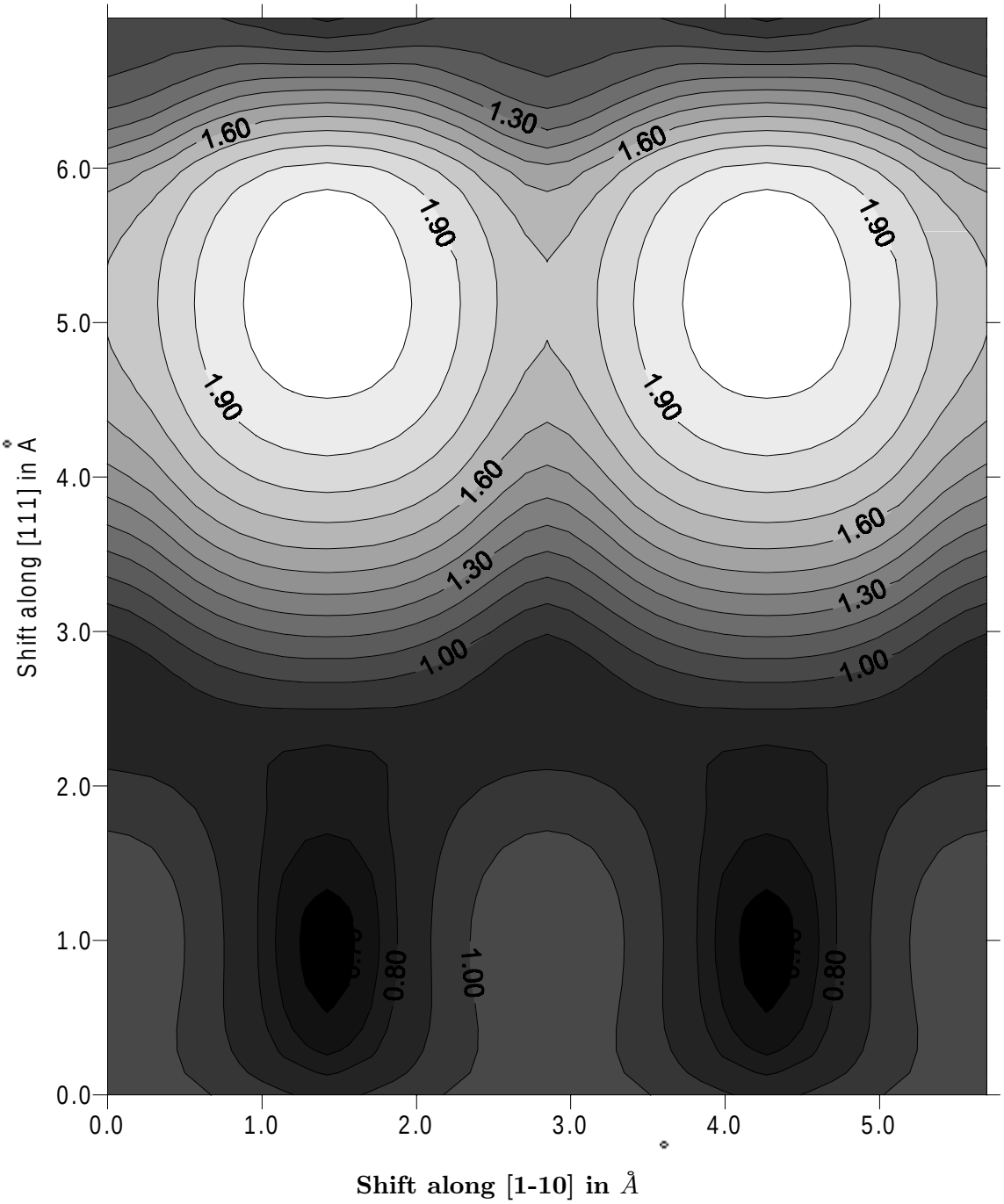

Figure 6.9: Computed stoichiometric $(11\overline{2})$ boundary γ-surface. (Energies are in J/m^2)

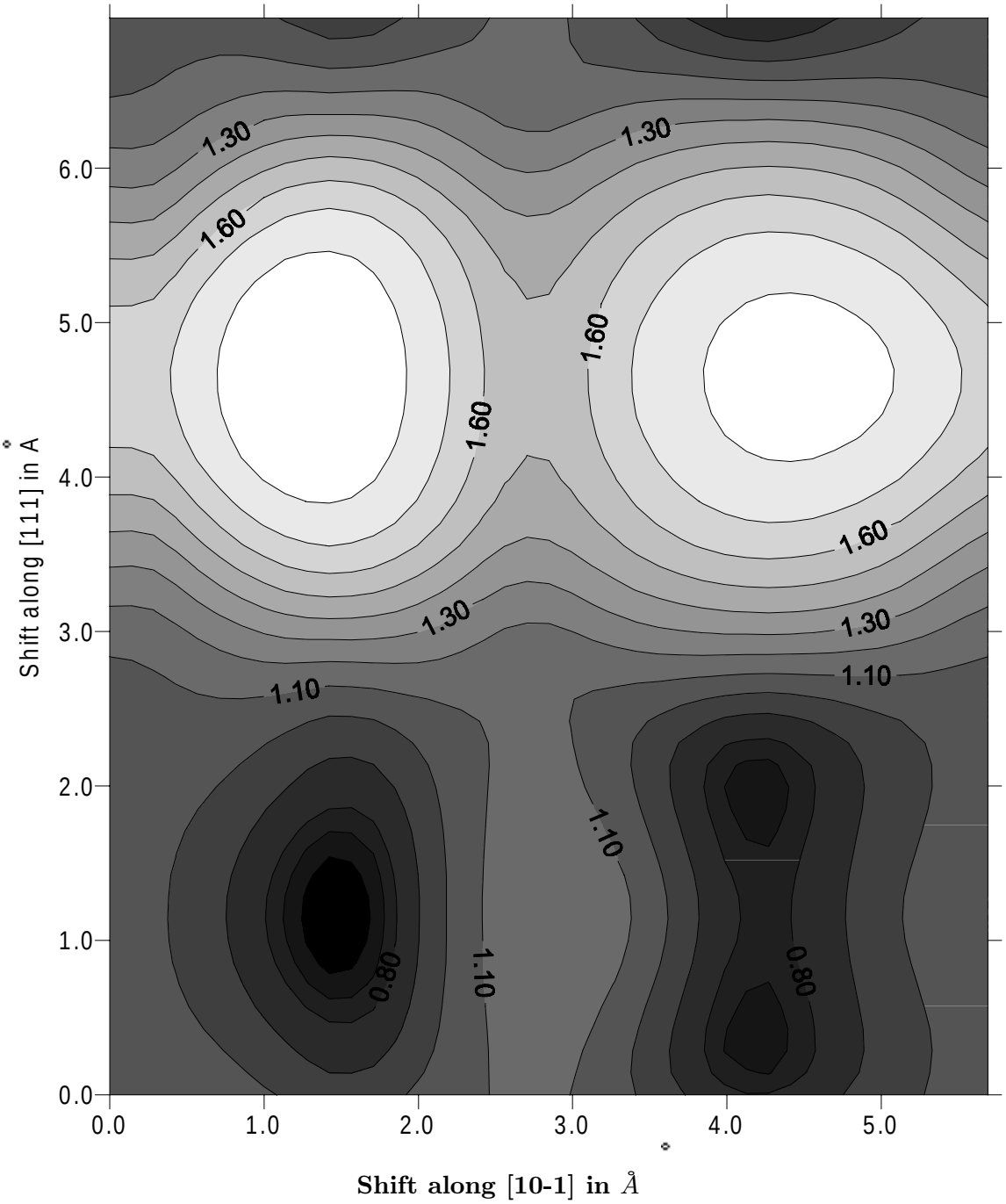

Figure 6.10: Computed stoichiometric $(1\overline{2}1)$ boundary γ-surface. (Energies are in J/m^2)

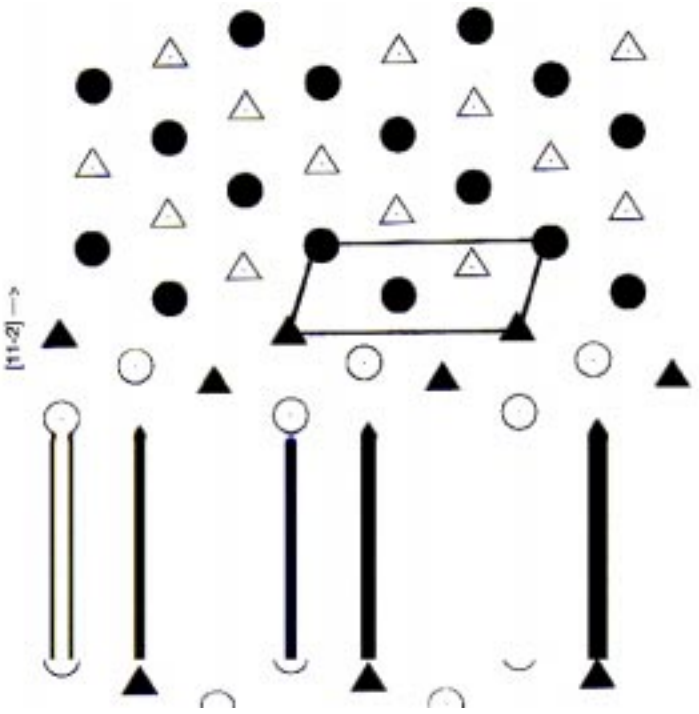

Figure 6.11: Structure of the $(11\overline{2})$ boundary.

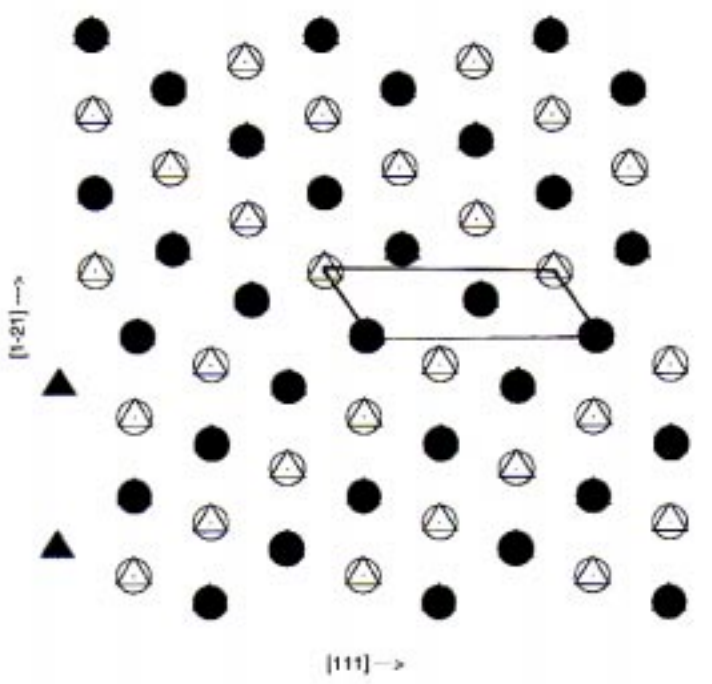

(a)

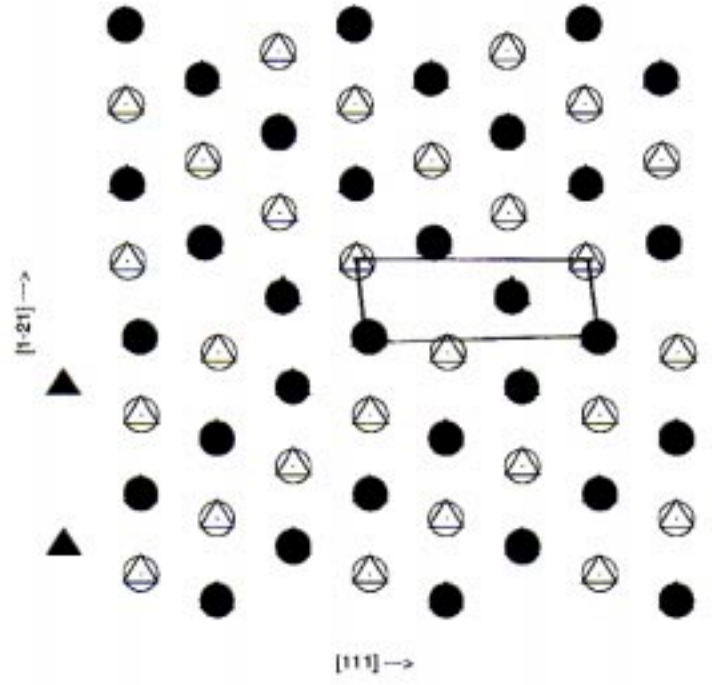

(b)

Figure 6.12: Structures of the$(1\bar{2}1)$ boundary.

Chapter 7

COMPARISON WITH EXPERIMENTAL RESULTS

7.1 Introduction

The intermetallic alloys, B2 NiAl and $L1_0$ TiAl have, for many years, been considered for development as structural materials. It is now well established that the interfaces in these materials play an important role in mechanical behavior. Atomic scale information about interfaces, obtained experimentally or computationally, can provide useful information to improve the understanding of macroscopic interfacial behavior of these materials and the possible effects of this behavior on other material properties. The purpose of the present work, is to compare the results obtained using these two techniques. The high resolution electron microscopy (HREM) observations of the (310)[001] grain boundary in NiAl [40], the (111)[11$\overline{2}$] [78] and (1$\overline{2}$1)[10$\overline{1}$] [42] boundaries in TiAl shall be compared to the computer simulations discussed earlier in Chapters 5 and 6.

Experimentally, there are many difficulties faced in the investigation of the structure-property correlations of grain boundaries due to the small size of the boundary region. The technique of high resolution electron microscopy (HREM) can provide information about the atomic structure of grain boundaries which is currently unattainable by any other experimental method. HREM provides a resolution of approximately one interatomic distance. It is possible to measure rigid body translations of two adjoining crystals, as well as determine the local atomic positions at the boundary. With this technique, it is also possible to study the morphology of the boundary plane, the orientation relationships and compositional ordering.

The drawbacks to this technique include the sample preparation of very thin crystals of the order of 100Å and the precise alignment of the boundary plane to ensure unambiguous results. The obtainment of this structural information is limited to the two grains in question having parallel

low-index zone axes and the grain boundary under study to be parallel to this direction. The major limitation of HREM is that no atomic structural variations in the direction of the beam are observable since this technique gives only the projection of structure of the boundary. The use of this method has thus been limited by the difficulty in sample preparation, since the above mentioned conditions hardly ever occur naturally. Bicrystals are usually used to study specific grain boundary orientations. These experimental observations are the closest experimental comparison to our grain boundary simulations.

7.2 Grain Boundary Simulations and Interatomic Potentials

Atomistic computer simulations allow for the energy minimization of a large number of atoms to give a stable boundary structure. Simulations describe the energetics and the detailed atomic structure of the boundary. Geometric models, such as the CSL, serve the purpose of providing the favored periodic boundaries for the computer simulations. For a detailed understanding of the atomic behavior of metals and intermetallics, specific atomistic processes must be considered. The Embedded Atom Method (EAM) was developed to handle atomistic calculations for defects, e.g. at surfaces and interfaces. It has been shown to accurately describe a large number of properties in metals and intermetallics.

The simulation technique used, for the present study, is standard molecular statics using embedded atom potentials and employing periodic boundary conditions in the plane of the boundary. The initial structures for energy minimization in TiAl were generated using a c/a ratio of one , to avoid lattice mismatch at the interfaces. Variants of the boundary structures were obtained by rigid-body translations applied to one of the crystals and lead to different types of matching between the two crystals without changing their misorientation or the position of the boundary plane. The difference in atomic distribution and sublattice occupation, thus obtained, leads to the structural variants in the boundary region. The structural relaxation procedure was the standard "molecular statics" technique using the conjugate gradient method for the energy minimization. Periodic boundary conditions were imposed in the directions parallel to the boundary plane, while

fixed boundary conditions were applied normal to the boundary plane. The total energy was also minimized with respect to possible rigid body displacements of one crystal relative to the other. For the simulated images the circles depict Al and the triangles Ti. Color variations of the symbols represent different planes of the respective tilt axis. The polyhedra delineate boundary repeat units and the line corresponds to the boundary plane.

The interatomic potentials for NiAl used in this study incorporated the Ni-Ni and Al-Al pair potentials developed by Farkas et al [58]. The electron density functions and embedding functions for both Ni and Al were those developed by Voter and Chen [53]. The mixed Ni-Al potentials differ from those of Voter and Chen and were fit specifically to the properties of B2 NiAl [58]. For the work on TiAl, the Ti potentials were those of Pasianot and Savino [56] who accounted for the contribution of the inner elastic constants. The electron density and embedding functions for Al were again those developed by Voter and Chen [53]. The mixed Ti-Al potential, which reproduces the properties of $L1_0$ TiAl, was that developed by Farkas [54].

7.3 Results and Discussion

7.3.1 NiAl

(310) Boundary

The most stable $\Sigma = 5(310)[001]$ stoichiometric grain boundary obtained for NiAl (Figure 7.2) can be compared to that studied experimentally by Fonda and Luzzi [40] [79], using HREM (Figure 7.1). The samples, with a thickness of $58\mathring{A}$, were examined using a JEOL JEM 4000EX microscope at 400kV and a defocus of -$650\mathring{A}$. The white atoms in the HREM image are the atomic columns. The Ni columns are brighter than the Al columns. The structure is asymmetrical with a rigid body displacement of $0.46\mathring{A}$ along $[1\overline{3}0]$.

Our simulations provide a very good match with the HREM image with the structure being asymmetrical due to the translation of the two grains. The simulated boundary period of $9.1\mathring{A}$ is consistent with the HREM image. The simulations predict a rigid body translation of one grain with respect to the other of $0.48\mathring{A}$, in good agreement with the $0.46\mathring{A}$ displacement observed by

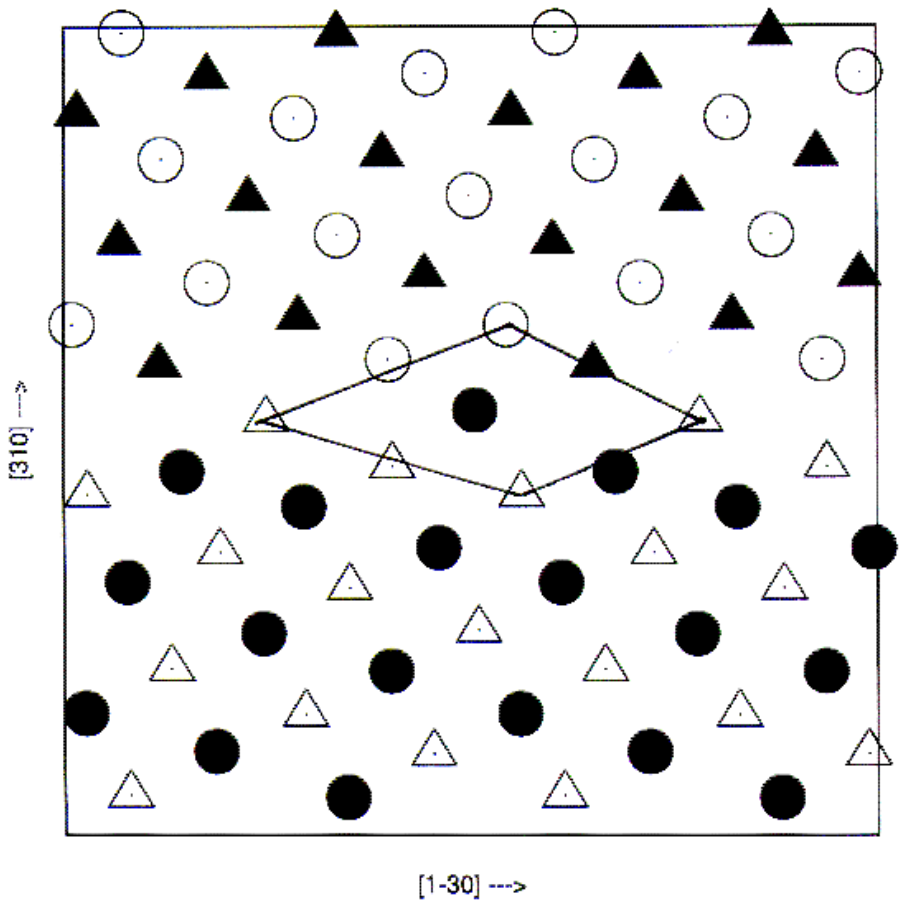

Figure 7.1: Observed HREM image of the $\Sigma = 5(310)[001]$ grain boundary in B2 NiAl

Fonda and Luzzi [79]. The computer simulated image showed atomic structural variations in the direction of the beam; a shift of $1.44\mathring{A}$ along the[001] direction of one grain with respect to the other. It is not possible to determine shifts in the beam direction using HREM.

7.3.2 TiAl

{111} Boundaries

Ricolleau et al. [78] investigated the atomic structure of {111} twin boundaries in γ-TiAl using HREM. The boundaries were observed along a $\langle 110]$ projection using an Akashi 0002B transmission

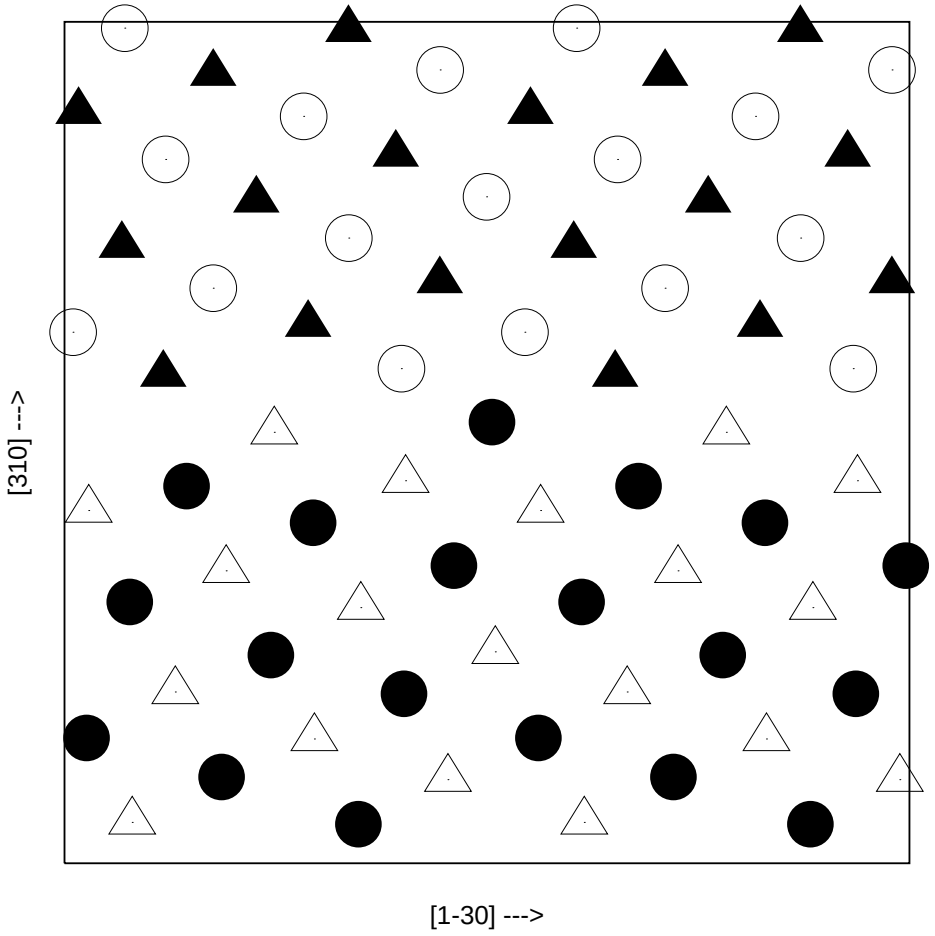

Figure 7.2: Simulated image of the Σ5(310)[001] grain boundary in B2 NiAl

electron microscope at 200kV with a resolution of 1.7$\mathring{A}$ and tilt facilities of $\pm 100^o$ on both axes. For the same operating conditions, two types of boundaries were observed. The first, is a pure twin boundary with perfect matching at the twin plane. The other structure observed (Figure 7.4) did not show exact coincidence at the twin plane. A shift of $1/2\langle 110]$ along the twin plane, corresponding to the APB in this structure, was observed. They confirmed the existence of not only the true twin but also the twin with APB.

The simulations predicted the existence of only two types of stable structures (Figure 6.4). These structures are the twin and the twin with a shift consistent with an APB. The pure twin boundary from the HREM investigations can be compared to our simulation (Figure 7.3). As in the experimental image, perfect matching at the interface is observed. The twin with APB (Figure 7.4) that was observed experimentally is also predicted in the computations. This structure is shown in Figure 7.5, and again the asymmetry due to the presence of the APB is consistent with the HREM image. These HREM images are a good match to our simulations.

$\{1\bar{2}1\}$ Boundaries

Inkson and Humphreys [42] investigated the $\Sigma = 3\{11\bar{2}1\}$ in TiAl using the JEOL 4000EX-II electron microscope. The interface, shown in Figure 7.6 was shown to be asymmetric, with a shift in the $\langle 111\rangle$ planes at 90^o to the interface of (0.22$\pm$ 0.02)a and a shift of (0.41$\pm$ 0.06)a along $[1\bar{2}1]$. Due to experimental limitations, the shift parallel to the $[10\bar{1}]$ beam direction was not obtained.

The stable structure predicted by computer simulations (Figure 7.7) was consistent with the HREM image. The structure was asymmetrical with a shift of 0.27a along [111], a shift of 0.34a along $[1\bar{2}1$ and a shift of 0.35a along $[10\bar{1}]$. The advantage of computer simulations is the ability to determine atomic structural variations in the direction of the beam.

7.4 Conclusions

The results obtained using HREM and atomistic simulations were compared for the $\Sigma = 5(310)[001]$ grain boundary in NiAl [40], the $\Sigma = 3(111)$ [78] and $\Sigma = 3(121)$ [42] boundaries.

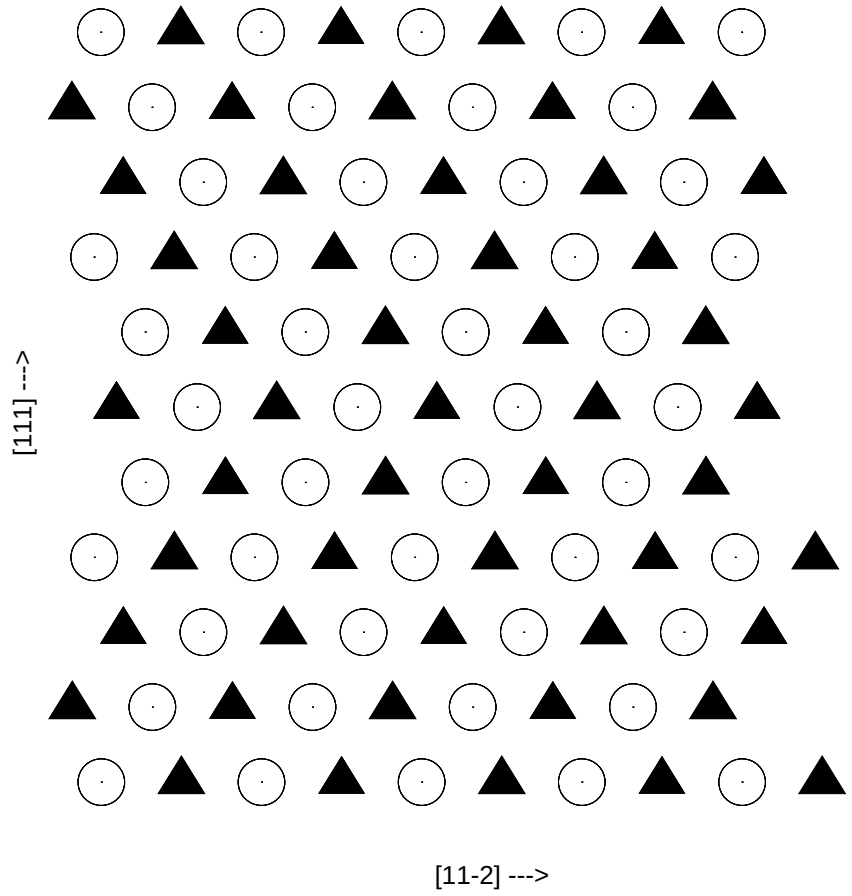

Figure 7.3: Simulated image of the $\Sigma 3(111)$ twin in $L1_0$ TiAl

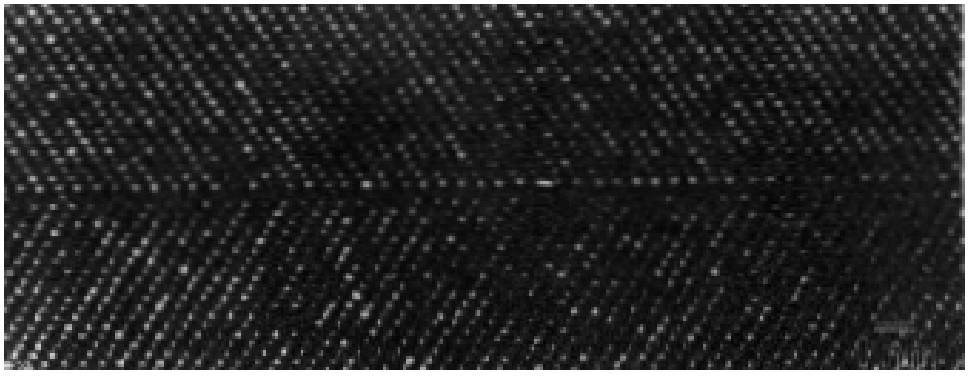

Figure 7.4: Observed HREM image of the $\Sigma 3(111)$ twin with an APB in $L1_0$ TiAl

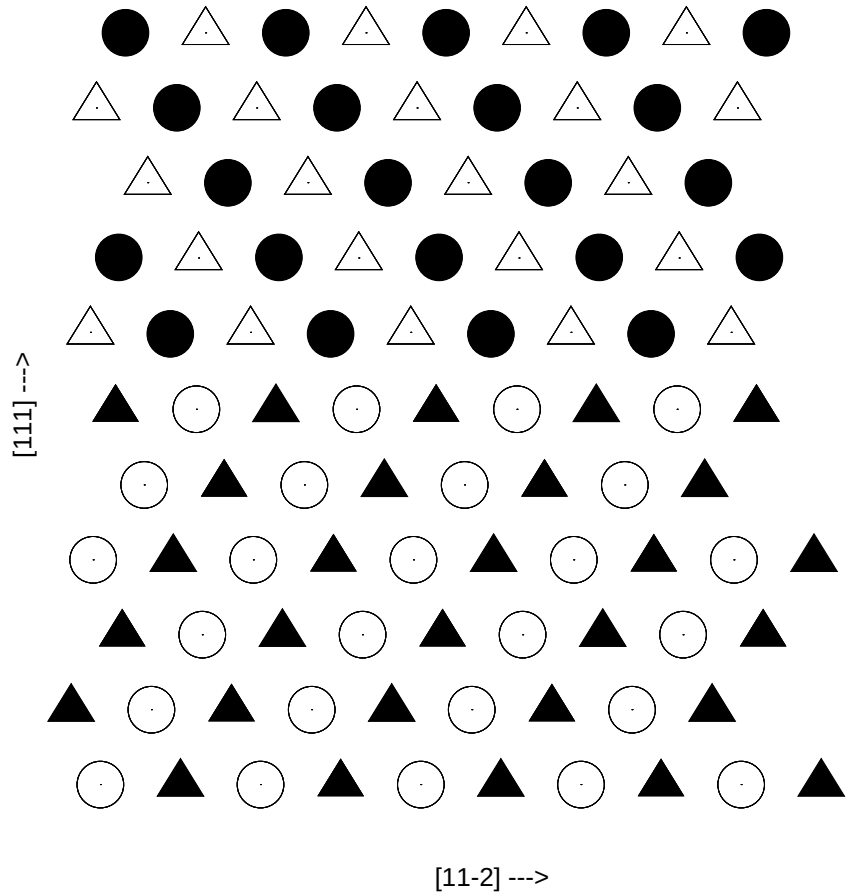

Figure 7.5: Simulated image of the Σ3(111) twin with an APB in $L1_0$ TiAl

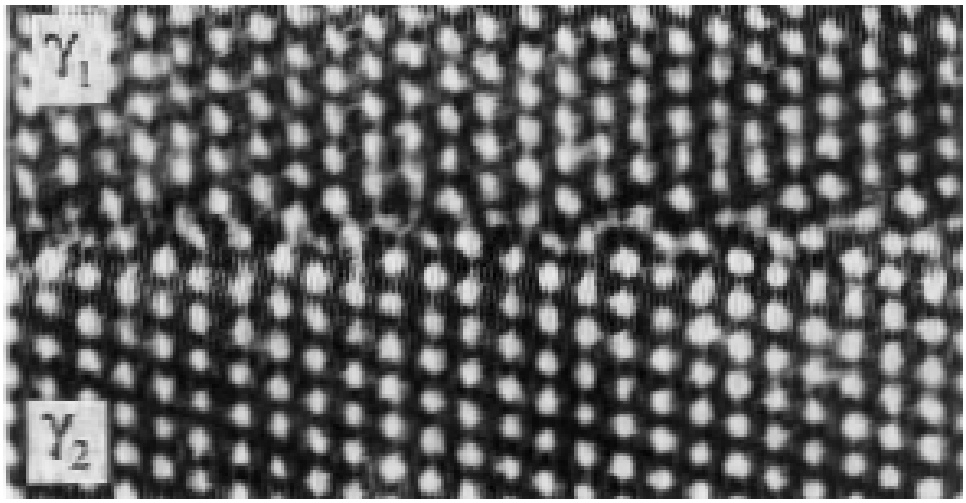

Figure 7.6: Observed HREM image of the $\Sigma 3(1\bar{2}1)[10\bar{1}]$ interface in $L1_0$ TiAl

It was shown that the EAM potentials using molecular statics accurately predict the atomic interactions in these intermetallics and the boundary structures most likely to exist within a given system. It is evident, therefore, that atomistic simulations can be used with confidence to predict structures and energetic trends for more complex orientations that are not easily accessible through present experimental techniques. The simulations also have the advantage of determining, not only, the atomic variations along the beam directions but also predicting the energies of the boundary.

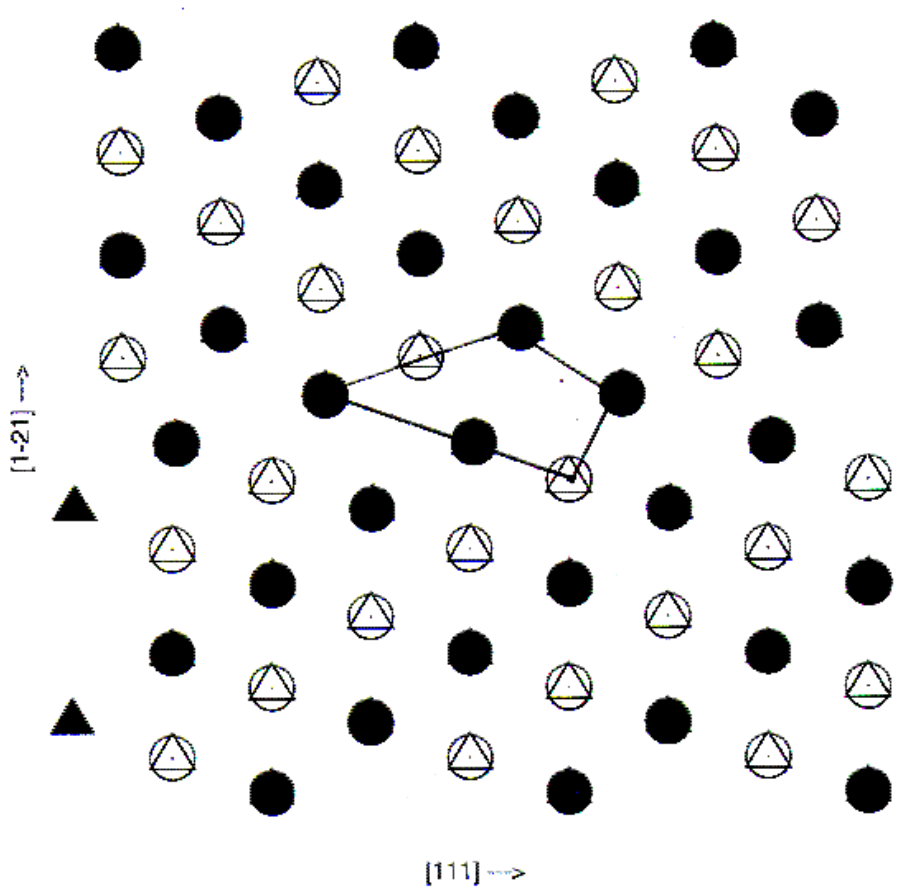

Figure 7.7: Simulated image of the $\Sigma 3(1\bar{2}1)[10\bar{1}]$ interface in $L1_0$ TiAl

Chapter 8
CONCLUSIONS

Atomistic computer simulations were performed on a number of bcc and fcc based ordered structures. Point defects, surfaces and grain boundaries were simulated in Ni Al, FeAl, CoAl and TiAl.

The true formation energies of vacancies and antisites were computed for all the compounds studied. The point defects of the B2 compounds were shown to be consistent with the triple-defect model in agreement with experimental observations. The results for formation energies of the constitutional defects in off-stoichiometric TiAl were also consistent with experiments. The chemical potentials of the different elements in these compounds were calculated for off-stoichiometric alloys at zero-temperature. These results formed the basis for energy calculations for surfaces and boundaries whose local composition differed from perfect stoichiometry. The discontinuity in the difference in the chemical potentials at stoichiometry results in a jump in the boundary energy depending on whether it is embedded in an Al-rich or Al-deficient bulk.

Atomistic simulations of surfaces containing the $\langle 001 \rangle$ axis were performed for both pure metals, Fe and Al and for ordered compounds, NiAl, FeAl and TiAl. A structural unit model was developed to estimate the energies and structural features of higher index surfaces, using some low index surfaces as a basis. The structural unit model successfully predicts the fraction of the different units that comprise the surface and show very good agreement with the simulated structures and energies. The values of surface energy calculated on the basis of this model are consistent with those derived from simulations. It was also shown that the surface energy difference within a given bulk decreases as one moves from low to high index surfaces in the absence of reconstruction, suggesting that the effect of the different terminations is not as important for high index surfaces.

Ordered intermetallic compounds exhibit a great variety of boundary structures that differ not

only in atomic atomic arrangement, but also in the chemical composition around the boundary plane. Different grain boundaries for the series of B2 compounds, CoAl, NiAl to FeAl, were simulated using the embedded atom method, and their energies calculated using the thermodynamically consistent method proposed by Hagen and Finnis [61]. The structures and energies were compared to obtain trends in these compounds. The defect structures that were simulated are very similar and the structural trends for the boundaries are consistent in the three compounds.

From the multiplicity of possible low energy structures it can be suggested that dislocations or APB's reaching the boundary can cause transformations between the different structures and this may influence the mechanical response of the grain boundary region.

The grain boundary energies increase in the series of compounds FeAl-NiAl-CoAl. The energy of the boundaries were found to be dependent on the composition of the boundary and on the composition of the bulk embedding the boundary. The effect of increasing the Al content in the boundary plane is more pronounced in Al-rich bulks than in the Al-deficient bulks.

The cohesive energy was shown to decrease with increasing Al content. The low cohesive energy structures have an Al-rich boundary composition and tend to appear in Al-rich and stoichiometric bulks and are not favored in Al-deficient bulks. It can therefore be surmised that the tendency towards brittle behavior decreases for Al-deficient alloys. We expect that increasing the concentration of the transition metal in these alloys will increase the occurrence of Al-deficient boundaries at the expense of Al-rich ones and thereby increase boundary cohesion and in turn decrease the probability of intergranular fracture. This phenomena should be general for all B2 aluminides since this was found in all the compounds studied.

Trends observed for the free surface energy in the B2 compounds showed the highest energies for NiAl and the lowest for FeAl. This behavior is consistent with that of the cohesive energy of the boundaries. NiAl has the highest boundary cohesive energies and FeAl the lowest for the grain boundaries studied. Since, experimentally, FeAl has been shown to be more ductile, this observation implies that grain boundary energy and grain boundary cohesion are not the only factors that determine the measure of ductility of these compounds; other factors such as the shear modulus, unstable stacking faults and the modes of slip across the boundary may play a role.

A possible criterion of grain boundary ductility was developed by analogy to the Rice criterion for bulk materials [74]. The combination $2\gamma_{us}/\gamma_{coh}$ was used as a criterion of grain boundary ductility. The values obtained for FeAl and NiAl are consistent with values within the range of the ductile to brittle transition in B2 intermetallics [75]. CoAl was shown to have a strong tendency for grain boundary brittleness.

An atomistic study of a number of different interfaces in TiAl was undertaken. Boundary γ-surfaces were computed for all the orientations chosen for detailed study, as were the low energy structures. Three distinct variants of the $\{111\}$ interface structure were observed namely the twin, the twin with APB and the pseudo twin. The structure and energy of the twin with APB was observed to be the same as that for a twin with a CSF. The twin type structures were shown to have the lowest energies in both the $\{11\overline{2}\}$ and $\{111\}$ interfaces. It was suggested that, in cases where an APB exists, it is energetically favorable for the system to create a twin with APB.

The results obtained using HREM and atomistic simulations were compared for the $\Sigma = 5(310)[001]$ grain boundary in NiAl [40], the $\Sigma = 3(111)[11\overline{2}]$ [78] and $\Sigma = 6(1\overline{2}1)[10\overline{1}]$ [42] boundaries. It was shown that the EAM potentials using molecular statics accurately predict the atomic interactions in these intermetallics and the boundary structures most likely to exist within a given system.

REFERENCES

[1] J. C. Beddoes, W. Wallace, and M. C. de Malherbe, Materials and Manufacturing Processes **7**, 527 (1992).

[2] D. B. Miracle and D. P. Pope, *NiAl and its Alloys*, volume 2, John Wiley and Sons, 1995.

[3] K. Vedula and P. Khadkikar, Environmental embrittlement - a major cause for low ductility of ordered intermetallics, in *High Temperature Aluminides and Intermetallics*, edited by C. T. Liu and C. G. McKamey, page 133, TMS, Warrendale, PA 15086, 1990.

[4] E. George and C. Liu, Journal of Materials Research **5**, 754 (1990).

[5] T. K. T. Kawabata and O.Izumi, Acta Metallurgica **33**, 1355 (1985).

[6] S.-C. Huang and J. C. Chestnutt, *Gamma TiAl and its Alloys*, volume 2, John Wiley and Sons, 1995.

[7] K. Vedula, *FeAl and Fe_3al*, volume 2, John Wiley and Sons, 1995.

[8] C. L. Briant, *Intergranular and Cleavage Fracture*, volume 1, John Wiley and Sons, 1995.

[9] R. Darolia, Journal of Metals **43**, 309 (1991).

[10] Y.-W. Kim, Journal Of Materials , 30 (1994).

[11] K. Vedula and J. Stephens, B2 aluminides for high temperature applications, in *Materials Research Society Symposium Proceedings*, volume 81, pages 381–391, 1987.

[12] I. Baker and P. Munroe, Properties of B2 compounds, in *High Temperature Aluminides and Intermetallics*, edited by S. Whang, C. Liu, D. Pope, and J. Stiegler, page 425, TMS, Warrendale, PA 15086, 1990.

[13] C. Liu, E. Lee, and C. McKamey, Scripta Metallurgica et Materialia **23**, 875 (1989).

[14] J. Brzeski, J. Hack, R. Darolia, and R. Field, Materials Science and Engineering A **170**, 11 (1993).

[15] K. Chang, R. Darolia, and H. Lipsitt, Acta Metallurgica et Materialia **10**, 2727 (1992).

[16] K. Chang, R. Darolia, and H. Lipsitt, Fracture of B2 aluminide single crystals, in *Materials Research Society Symposium Proceedings*, volume 213, pages 597–602, Materials Research Society, 1991.

[17] K. Hahn and K. Vedula, Scripta Metallurgica **23**, 7 (1989).

[18] J. Schneibel, M. Jenkins, and P. Maziasz, Crack propagation in NiAl and FeAl, in *Materials Research Society Symposium Proceedings*, volume 288, pages 549–554, 1993.

[19] A. Ball and R. Smallman, Acta Metallurgica et Materialia **14**, 1349 (1966).

[20] R. V. Mises, Z. Agnew. Math. Mech. **8**, 161 (1928).

[21] R. Noebe and R. Gibala, Scripta Metallurgica et Materialia **20**, 1635 (1986).

[22] A. Rozner and R. Wasilewski, J. Inst. Metals **94**, 169 (1966).

[23] I. Baker and D. Gaydosh, Materials Science and Engineering **96**, 315 (1987).

[24] C. Liu and E. George, Effect of aluminum concentration and boron dopant on environmental embrittlement in FeAl aluminides, in *Materials Research Society Symposium Proceedings*, volume 213, pages 527–532, Materials Research Society, 1991.

[25] S. Guha, P. Munroe, and I. Baker, Scripta Metallurgica et Materialia **23**, 897 (1989).

[26] K. Russell and J. Edington, Metal. Sci. **6**, 20 (1972).

[27] D. Miracle, S. Russell, and C. Law, in *Materials Research Society Symposium Proceedings*, volume 133, page 225, 1989.

[28] R. Darolia, D. Lahrman, R. Field, and A. Freeman, in *Materials Research Society Symposium Proceedings*, volume 133, page 113, 1989.

[29] M. Sherman and K. Vedula, Journal of Materials Research **21**, 1974 (1986).

[30] R. Hutchings and M. Loretto, Metal. Sci. **12**, 503 (1978).

[31] S.-C. Huang, *Alloying Considerations in Gamma-Based Alloys*, TMS, 1993.

[32] C. M. Austin and T. J. Kelly, *Development and Implementation Status of Cast Gamma Titanium Aluminide*, TMS, 1993.

[33] T. Kawabata and O. Izumi, Mechanical properties of tial, in *High Temperature Aluminides and Intermetallics*, edited by S. Whang, C. Liu, D. Pope, and J. Stiegler, page 403, TMS, Warrendale, PA 15086, 1990.

[34] S. Whang and Y. Hahn, Dislocation structure in $l1_0$ type titanium aluminides., in *High Temperature Aluminides and Intermetallics*, edited by S. Whang, C. Liu, D. Pope, and J. Stiegler, page 91, TMS, Warrendale, PA 15086, 1990.

[35] F. Froes, C. Suryanarayana, and D. Eliezer, ISIJ International **10**, 1235 (1991).

[36] A. Sutton and V. Vítek, Acta Metallurgica et Materialia **30**, 2011 (1982).

[37] A. Sutton, International Metals Review **29**, 377 (1984).

[38] A. Brokman and R. Balluffi, Acta Metallurgica et Materialia **29**, 1703 (1981).

[39] A. Sutton and V. Vítek, Phil. Trans. R. London A **309**, 1 (1983).

[40] R. Fonda and D. Luzzi, in *Materials Research Society Symposium Proceedings*, volume 288, page 361, 1993.

[41] K. Nadarzinski and F. Ernst, Materials Science Forum **207**, 309 (1996).

[42] B. Inkson and C. Humphreys, An hrem investigation of a 121_{L1_0} boundary in tial., in *High Temperature Ordered Intermetallic Alloys VI*, volume 364, page 605, Materials Research Society, 1995.

[43] D. Farkas and V. Rangarajan, Acta Metallurgica et Materialia **35**, 353 (1987).

[44] T. Takasugi and O. Izumi, Acta Metallurgica et Materialia **31**, 1187 (1983).

[45] J. Kruisman, V. Vítek, and J. D. Hosson, Acta Metallurgica et Materialia **36**, 2729 (1988).

[46] S. Chen, D. Srolovitz, and A. Voter, Journal of Materials Research **4**, 62 (1989).

[47] G. Petton and D. Farkas, Scripta Metallurgica et Materialia **25**, 55 (1991).

[48] D. Farkas, Metallurgical and Materials Transactions A **25**, 1337 (1994).

[49] B. Pestman, J. D. Hosson, V. Vítek, and F. Schapink, Interaction between lattice dislocations and grain boundaries in ordered compounds, in *Materials Research Society Symposium Proceedings*, volume 213, pages 429–434, Materials Research Society, 1991.

[50] M. Daw and M. Baskes, Physical Review B **29**, 6443 (1984).

[51] J. H. Rose, J. R. Smith, F. Guinea, and J. Ferrante, Physical Review B **29**, 2963 (1984).

[52] Y. Mishin and D. Farkas, (1996), Philosophical Magazine A.

[53] A. Voter and S. Chen, Accurate interatomic potentials for Ni, Al and Ni_3Al, in *Materials Research Society Symposium Proceedings*, volume 82, pages 175–180, 1987.

[54] D. Farkas, Modelling and Simulation in Materials Science and Engineering **2**, 975 (1994).

[55] G. Simonelli, R. Pasianot, and E. Savino, in *Materials Research Society Symposium Proceedings*, volume 291, page 567, 1993.

[56] R. Pasianot and E. Savino, Physical Review B **45**, 12704 (1992).

[57] C. Vailhé and D. Farkas, Shear faults and dislocation core structures in B2 CoAl, in *Materials Research Society Symposium Proceedings*, volume 364, page 395, 1995.

[58] D. Farkas, B. Mutasa, C. Vailhé, and K. Ternes, Modelling and Simulation in Materials Science and Engineering **3**, 201 (1995).

[59] R. Pasianot, D. Farkas, and E. Savino, Physical Review B **43**, 6952 (1991).

[60] F. Gao and D. J. Bacon, Philosophical Magazine A **67**, 275 (1993).

[61] M. Hagen and M. Finnis, Materials Science Forum **207-209**, 245 (1996).

[62] R. Jayaram and M. Miller, Acta Metallurgica et Materialia **42**, 1561 (1994).

[63] H. Xiao and I. Baker, Acta Metallurgica et Materialia **42**, 1535 (1994).

[64] D. Paris and P. Lesbats, Journal of Nuclear Materials **69-70**, 628 (1978).

[65] M. Crimp, K. Vedula, and D. Gaydosh, Room temperature tensile ductility in powder processed B2 FeAl alloys, in *Materials Research Society Symposium Proceedings*, volume 81, pages 499–504, 1987.

[66] Y. Shirai and M. Yamaguchi, Materials Science and Engineering A **152**, 173 (1992).

[67] Z. L. D. Vujik and S. Whang, Metallurgical Transactions A **19**, 2455 (1988).

[68] M. Finnis and J. Sinclair, Philosophical Magazine A **50**, 45 (1984).

[69] S. Foiles, M. Baskes, and M. Daw, Physical Review B **33**, 7983 (1986).

[70] C. Vailhé and D. Farkas, Shear faults and dislocation core structures in B2 FeAl, submitted to Acta Met.

[71] E. Savino and D. Farkas, Philosophical Magazine A **58**, 227 (1988).

[72] V. Vítek, Philosophical Magazine **18**, 773 (1968).

[73] S. Chen, A. Voter, and D. Srolovitz, Scripta Metallurgica et Materialia **20**, 1389 (1986).

[74] J. Rice, Journal of the Mechanics and Physics of Solids **40**, 239 (1992).

[75] D. Farkas, S.J.Zhou, C. Vailhé, B. Mutasa, and J. Panova, Journal of Materials Research **12**, 93.

[76] J. Christian and D. Laughlin, Acta Metallurgica et Materialia **36**, 1617 (1988).

[77] J. Panova and D. Farkas, Atomistic simulation of dislocation core configuration in TiAl, to be published.

[78] C. Ricolleau, A. Denquin, and S. Naka, **69**, 197 (1994), Philosophical Magazine A.

[79] R. W. Fonda, M. Yan, and D. E. Luzzi, **71**, 221 (1995), Philosophical Magazine Letters.

VITA

The author was born in Mutare, Zimbabwe on the 28th of November in 1969. After spending 19 wonderful years in Harare, Batsirai Manyara Mutasa (Batsi) traveled across the sees to Greensboro, North Carolina. There she completed her undergraduate studies in May of 1992. With her Bachelors Degree in Interdisciplinary studies in Physics from Bennett College, she took a one year detour to do some Chemical Engineering at North Carolina A & T State University. From there she traveled across the state border to Blacksburg,Virginia; which reminded her of the mountains of the eastern highlands in her native Zimbabwe. The author started the Materials Engineering Science Ph.D program in August of 1993 at Virginia Tech.

Batsirai Mutasa